



TECHNISCHE
UNIVERSITÄT
WIEN

DISSERTATION

Quantum Dynamics of Strongly Interacting BEC of Molecules

ausgeführt am Atominstitut



der Technische Universität Wien
Fakultät für Physik

unter der Anleitung von
Prof. Dr. Jörg Schmiedmayer

durch

Qi Liang

Matrikelnummer: 01527357

Stadionallee 2
1020 Wien

Wien, am 18.03.2025

身無半畝心憂天下
讀破萬卷神交古人

Declaration

I hereby declare and confirm that this thesis is entirely the result of my own original work. Where other sources of information have been used, they have been indicated as such and properly acknowledged. I further declare that this or similar work has not been submitted for credit elsewhere.

Wien, am 18.03.2025

.....

Qi Liang

Abstract

This thesis presents an overview of a cold atom experiment with Bose-Einstein condensation of molecules formed by fermionic lithium-6. The experiment is constructed with the interest of exploring the field of fundamental physics, especially the dynamics of non-equilibrium quantum many-body systems in the presence of strong interactions, and it is achieved through accessing the broad Feshbach resonance of ^6Li . The designs and applications of various techniques that are employed in the process of creating a molecular Bose-Einstein condensate are shown in detail. Furthermore, the results of experiments, that are conducted with this experimental apparatus, on scattering process and universal scaling dynamics are demonstrated with analysis.

Zusammenfassung

Diese Arbeit präsentiert einen Überblick über ein Kaltatom-Experiment mit Bose-Einstein-Kondensation von Molekülen, die durch fermionisches Lithium-6 gebildet werden. Das Experiment wurde mit dem Ziel konzipiert, das Feld der fundamentalen Physik zu erforschen, insbesondere die Dynamik von Nichtgleichgewichts-Quantenvielteilchen systemen in Gegenwart starker Wechselwirkungen. Dies wird durch den Zugang zur breiten Feshbach-Resonanz von ^6Li ermöglicht. Die Entwürfe und Anwendungen verschiedener Techniken, die im Prozess der Erzeugung eines molekularen Bose-Einstein-Kondensats verwendet werden, werden detailliert dargestellt. Darüber hinaus werden die Ergebnisse von Experimenten zum Streuprozess und zur universellen Skalierungsdynamik, die mit diesem experimentellen Aufbau durchgeführt wurden, analysiert und erläutert.

Contents

1. Introduction	1
2. Preliminary Knowledge	2
2.1. Properties of Lithium (Li)	2
2.2. Feshbach Resonance	6
2.2.1. Feshbach Molecule	8
2.3. Gross-Pitaevskii Equation	9
2.3.1. Thomas-Fermi Approximation	11
3. Experimental Setup	13
3.1. Vacuum System	13
3.2. Magnetic Field Coils	17
3.2.1. MOT Coils	18
3.2.2. Zeeman Slower	19
3.2.3. Bitter Type Coil	20
3.2.4. Sci-Coil Sets	20
3.2.5. Fast Switching of Magnetic Field	21
3.3. Laser System	23
3.3.1. Optical Transport	29
3.3.2. Optical Lattice	32
3.3.3. Speckle Potential	34
3.4. Imaging	36
3.4.1. Absorption Imaging	36
3.4.2. MOT Chamber	39
3.4.3. Sci Chamber	40
3.5. State Manipulation	42
3.5.1. Radio Frequency Transition	42
3.5.2. Microwave Transition	45
3.6. Producing Bose-Einstein Condensate of Molecule	48
4. Scattering from Optical Lattice	52
4.1. Diffraction from Lattice	52
4.1.1. Raman-Nath regime: Kapitza-Dirac Scattering	53

4.1.2.	Beyond Raman-Nath: Channeling regime	56
4.1.3.	Interaction Induced Slowing	57
4.1.4.	Incoherent Collisions	61
4.2.	Molecular Interferometer	66
4.2.1.	Michelson Type	66
4.2.2.	Ramsey Type	68
4.2.3.	Interaction Induce Energy Shift	71
5.	Universal Scaling Dynamics in Strongly Interacting Bose Gas	73
5.1.	Renormalization Group and Non-Thermal Fixed Point	73
5.2.	Experiment	76
5.2.1.	Breathing Suppression	77
5.2.2.	Vertical Speckle Setup	79
5.3.	Scaling Analysis	80
5.3.1.	Identify Scaling Windows	81
5.3.2.	Scaling Check	88
5.4.	Thermalization of Solitonic State	90
5.4.1.	Random Defect Model (RDM)	92
5.4.2.	Decay of Solitons	94
6.	Conclusion and Outlook	99
	Appendix	102
A.	Experiment Control	102
B.	Control Program	104
C.	Rotational Waveplate Mount	109
	List of Figures	112
	List of Tables	119
	References	120

1. Introduction

The non-equilibrium dynamic of many-body quantum systems is essential for physics over many orders of magnitude in length scale, energy, and time. Understanding non-equilibrium processes will not only elevate our knowledge about fundamental physics but also assist in the development of quantum technology such as quantum information and communication.

However, despite much research effort, too few are understood. Neither the timescale of thermalization nor the transient processes during the evolution is clearly established. The maximum entropy principle predicts the quantum states in equilibrium but does not show the pathway of dynamically reaching equilibrium. Moreover, in systems where conservation laws of motion exist as constraints, many-body systems are expected to display complex behavior. For instance, an intriguing phenomenon in such a context is pre-thermalization [1]. The rapid establishment of a quasi-stationary state is predicted, which differs from the real thermal equilibrium. Full thermalization, if it occurs, is expected to do so on a further much longer timescale.

The emergence of an ultra-cold atom system introduces an ideal experimental platform for investigating such phenomena. Combining the long coherent time of a Bose-Einstein condensate and the tunability over many system parameters, a quantum gas with designed initial conditions could be prepared, and its evolution could be well observed. This thesis starts with the aim to construct an ultra-cold atom experiment using fermionic lithium 6, where the relaxation phenomenon could be investigated over a larger range of scenarios, such as different inter-particle interactions, different dimensionality, the distinction between bosonic molecules and fermionic atoms, etc.

In this thesis, I will first present the preliminary knowledge required to understand the basis of the experiment. Then, as a major part of the thesis, the details of the design and construction of the experiment will be explained. In the last two chapters, I will show the results of the experiments we have performed, with the corresponding analysis.

2. Preliminary Knowledge

2.1. Properties of Lithium (Li)

In this section, the property of lithium that is most relative to the experiment will be introduced. For a more comprehensive description, one could refer to article [2] or the full "Handbook" [3].

There are two stable isotopes of lithium - ${}^7\text{Li}$ and ${}^6\text{Li}$, with natural abundances 92.4% and 7.6%. In our experiment, we choose ${}^6\text{Li}$ to explore systems of strongly interacting fermions or paired bosonic molecules.

Property (${}^6\text{Li}$)	Value
Density (300 K)	0.534 g/cm ³
Atomic Mass	6.0151223 u
	$9.9883414 \times 10^{-27}$ kg
Melting Point	453.69 K
Boiling Point	1615 K

As the lightest alkali metal, lithium is in solid form at room temperature. The vapor pressure can be approximately calculated with:

$$P_{\text{Li}} = 10^{8.061 - 8310/T} \text{ mbar}.$$

At room temperature $T \sim 300$ K, the vapor pressure of lithium is in the order of 10^{-20} mbar, which is far too low for preparing ultracold atom samples. The alternative is heating the lithium to ~ 700 K, where the vapor pressure reaches about 10^{-5} mbar, then slowing down and capturing the atoms.

Atomic Structure

Like all alkali atoms, ${}^6\text{Li}$ atom has a hydrogen-like atomic structure, where the outer shell consists of only one electron. The hyperfine splitting of ground state $2S_{1/2}$

is 228.20526 MHz [4]. The $2S_{1/2} \rightarrow 2P_{1/2}$ and $2S_{1/2} \rightarrow 2P_{3/2}$ are the main optical transition at 671 nm with 10 GHz separation in between, which are normally referred to as the D1 and D2 transitions. D2 transition is chosen for laser cooling similar to other alkali species. However, the excited state of the D2 transition has 3 hyperfine states that split over a range of ~ 4.6 MHz, which is smaller than the linewidth of D2 transition $\Gamma = 5.87$ MHz. This forbids the usage of regular optical molasses techniques. To make a ^6Li molasses, the D1 transition needs to be involved with the gray molasses technique [5].

The state energy can be calculated with the Breit-Rabi formula [6]:

$$E(B, F = I \pm \frac{1}{2}, m_F) = -\frac{\Delta E_{hf}}{2(2I+1)} - g_N m_F \mu_B B \pm \frac{1}{2} \sqrt{\Delta E_{hf}^2 + \frac{4m_F}{2I+1} (g_j - g_N) \mu_B B \Delta E_{hf} + (g_j - g_N)^2 \mu_B^2 B^2}, \quad (2.1)$$

while $\Delta E_{hf} = h \times 228$ MHz is the hyperfine energy splitting energy at $B = 0$, F is the total electric angular momentum and $\mu_B \approx 1.4$ MHz/G is the Bohr magneton. For ^6Li ground state $2S_{1/2}$ we have $I = 1$. To simplify the formula, one could define:

$$x = \frac{(g_j - g_N) \mu_B B}{\Delta E_{hf}},$$

such that Formula 2.1 can be rewritten as:

$$E_g(B, F_{\pm}, m_F) = -\frac{\Delta E_{hf}}{6} - \frac{\Delta E_{hf} m_F}{g_j/g_N - 1} x \pm \frac{\Delta E_{hf}}{2} \sqrt{1 + \frac{4m_F}{3} x + x^2}. \quad (2.2)$$

Note the value of constant $g_j = 2.0023010$ and $g_N = 0.0004476540$ [4]. So the second term is sometimes omitted for its small contribution. This is referred to as the Zeeman regime, where the energy shift is dominated by electron-nuclear spin interaction under an external magnetic field, and it is only valid for low magnetic field ($B < 50$ G).

For a higher magnetic field, the orbital and spin angular momenta are decoupled and the state energy will mainly have a dependence on electron spin m_s and nuclear spin m_I . This is referred to as the Paschen-Back regime. In this regime, the state energy is linearly proportional to the magnetic field $E \sim \mu_B B$. The high-field seeking or low-field seeking property is given by the sign of m_s , as shown in Figure 2.1.

In addition to the D2 transition, we also use another optical transition at 323 nm [7], which is normally referred to as Ultraviolet (UV) or narrow-line transition. Because the linewidth of the UV transition is much narrower than the D2 transition, it is capable

2. Preliminary Knowledge

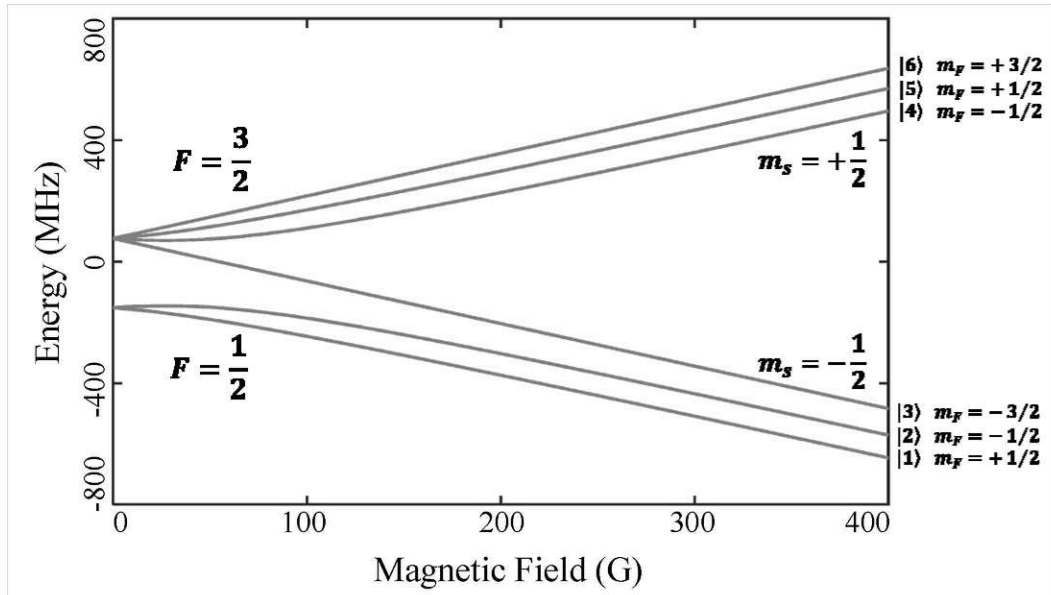


Figure 2.1.: The energy level of ${}^6\text{Li}$ atom plot with magnetic field.

of reaching a much lower temperature by laser cooling. In the experiment, we use UV cooling as an alternative 'sub-Doppler' cooling method. The information on optical transitions is given in Figure 2.2.

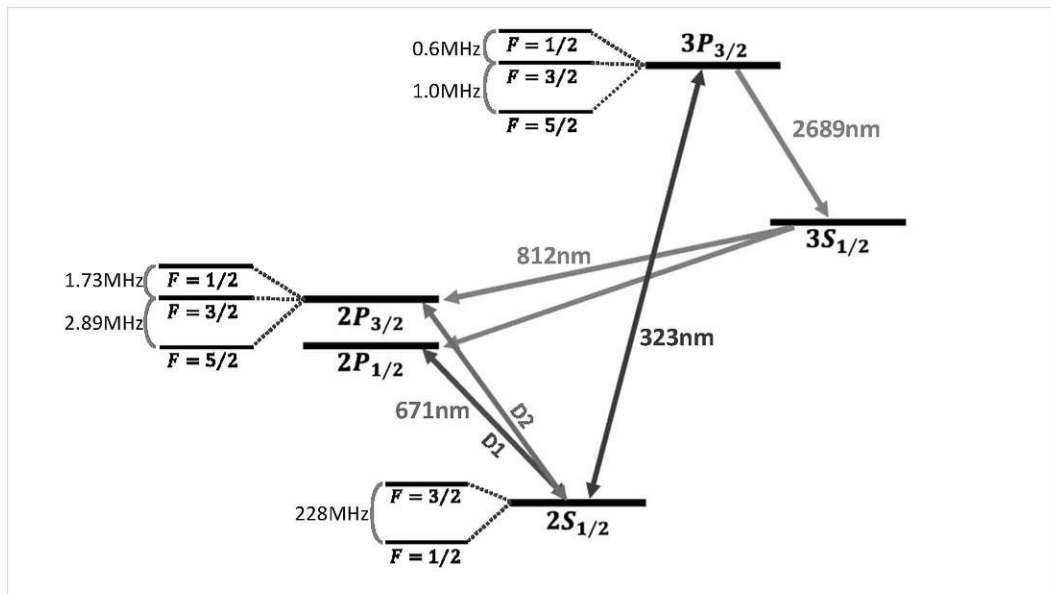


Figure 2.2.: Optical dipole transitions of ${}^6\text{Li}$ atom.

2. Preliminary Knowledge

Table 2.1.: Major optical transitions of ${}^6\text{Li}$ [8].

Property	D1	D2	UV
Wavelength	670.992421 nm	670.977338 nm	323.361168 nm
Frequency	446.789635 THz	446.799685 THz	927.113357 THz
Linewidth	5.8724 MHz	5.8724 MHz	157 kHz
Recoil	9.886554 cm/s	9.886776 cm/s	20.515149 cm/s
Doppler Limit		140 μK	15 μK

Magic Wavelength

The application of optical dipole traps gives great convenience in forming different trapping potentials. While coupling the electric dipole of an atom to the electric field of light, the single energy level of the atom will be shifted, as referred to as "(AC) Stark Shift" [9]. This effect often results in the shifting of optical transition frequency and poses a problem for accessing the optical transition in the presence of an optical dipole trap.

Luckily for us, the polarizability of each state has a different dependence on the wavelength of light. This means, that at a particular wavelength of some transition, the Stark shift of ground state and excited state of an optical transition would be equal, such that the transition frequency would not be affected. This special wavelength is called "Magic Wavelength".

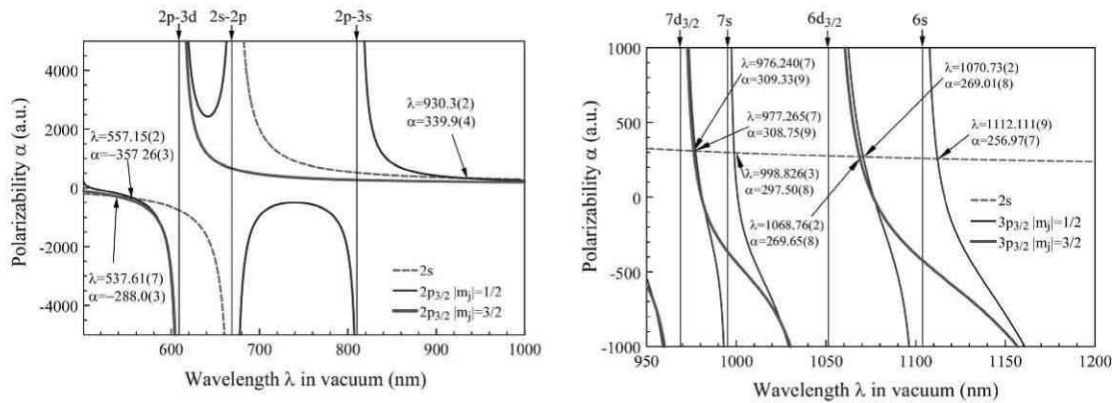


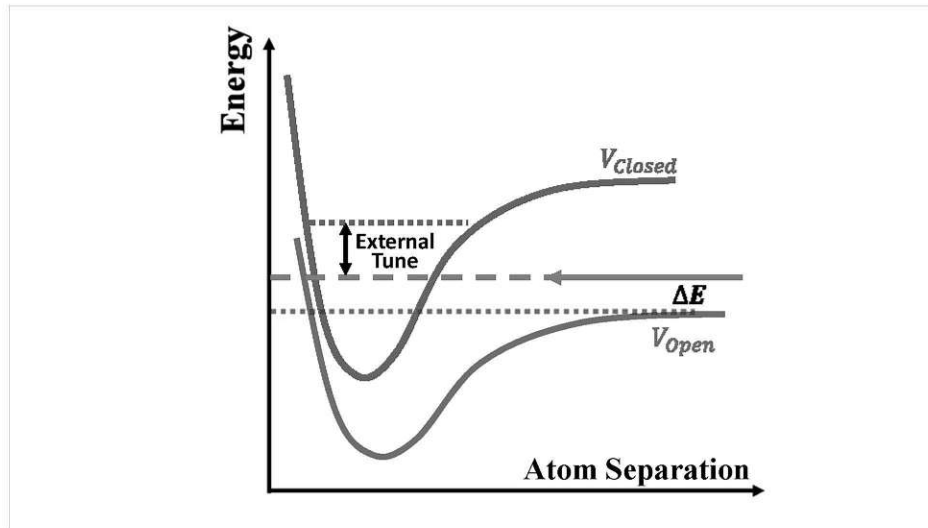
Figure 2.3.: The wavelength-dependent polarizability of the $2s \leftrightarrow 2p_{3/2}$ states (Left) and $2s \leftrightarrow 3p_{3/2}$ states (right). Figure adapted from Ref.[10]

In Figure 2.3 we show the result from Ref.[10] of polarizability calculation on ${}^6\text{Li}$ energy levels and the respective magic wavelength for different transitions. To exploit the magic wavelength of $2s \leftrightarrow 3p_{3/2}$ transition, we choose to use 1070 nm laser for our dipole trap, where UV cooling could be effective in-trap.

2.2. Feshbach Resonance

The idea of Feshbach Resonance was introduced by Herman Feshbach in the 1950s [11, 12] in the context of nuclear physics (Also by Ugo Fano [13]), where a bound state could occur upon collision of two slow atoms. Decades of theory studies were made for how such a phenomenon will emerge in different atom species until it was experimentally demonstrated in 1977 [14]. Later, with the development of ultra-cold atom/Bose-Einstein condensate, the capability of tuning interaction via Feshbach resonance was soon demonstrated in ^{23}Na [15] and ^{85}Rb [16].

For a typical alkali atom, the scattering length is in the same order as the van der Waals radius, which is $50a_0 \sim 100a_0$. In our system, we aim to study dynamics in the high interaction regime $a > 1000a_0$, and this is made possible through the application of Feshbach Resonance. This phenomenon allows the tuning of inter-particle interaction by controlling the external magnetic field, and it is an essential ingredient of our experiment. A detailed and comprehensive review can be found in Ref. [17].



To give a simple picture for understanding this phenomenon, we consider two molecular potentials V_{open} and V_{closed} . This is referred to as open and closed channels for two free atoms during a collision with energy ΔE . Note that closed channel potential is required to possess at least one bound state. When the energy between two channels is tunable, the bound molecular state of a closed channel can be tuned to approach the scattering state of the open channel, and a strong coupling between two atoms is formed. Such tuning is normally achieved with an external magnetic field, but it is also possible optically [18].

For a magnetically tuned Feshbach resonance, the s-wave scattering length is given

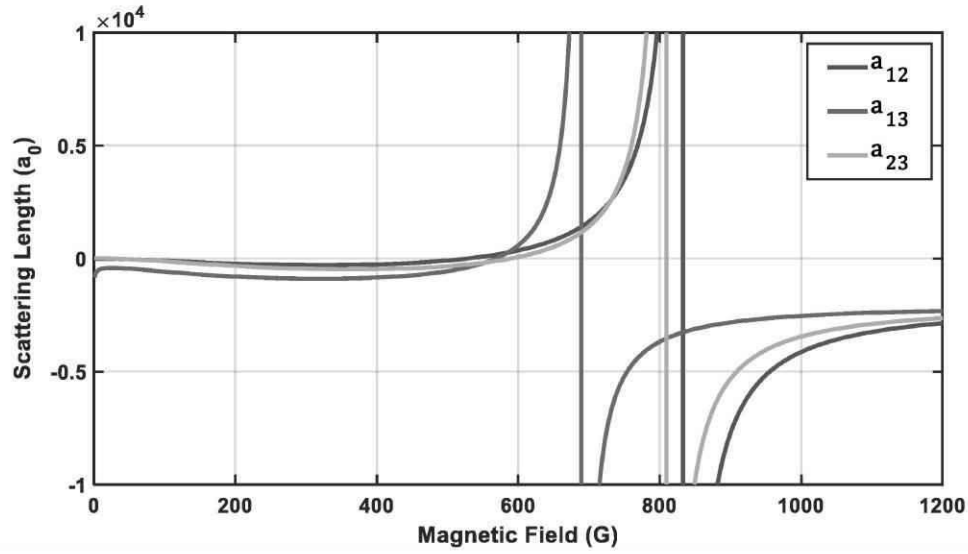


Figure 2.4.: Feshbach resonances between the lowest three energy states of ${}^6\text{Li}$ [21].

by the function:

$$a = a_{bg} \left(1 - \frac{\Delta}{B - B_0} \right), \quad (2.3)$$

where a_{bg} is the far-from-resonance background scattering length, B_0 is the resonance magnetic field and Δ is the width of resonance. Accessing the Feshbach resonance between two particular states poses a very difficult challenge for most species as the width of the resonance is usually very small. For example, in Rubidium 87, the Feshbach resonances are in the order of 0.01~0.001 G.

Table 2.2.: Feshbach resonances between the lowest 3 energy states of ${}^6\text{Li}$.

Channel	B_0 (G)	Δ (G)	a_{bg} (a_0)	Ref
$ 1\rangle 2\rangle$	834.1	-300	-1405	[19]
$ 1\rangle 2\rangle$	543.25	0.1	60	[20]
$ 1\rangle 3\rangle$	690.4	-122.3	-1727	[19]
$ 2\rangle 3\rangle$	811.2	-222.3	-1490	[19]

From Table 2.2, we could see the advantage of using ${}^6\text{Li}$. Between all three lowest energy states, there are Feshbach resonances within an accessible magnetic field. The width of the resonance is in the order of a few hundred Gauss which greatly eases the requirement for precise control of magnetic fields. Furthermore, the fermionic nature of ${}^6\text{Li}$ atoms blocks the three-body collision by the Pauli exclusion principle [22, 23], which allows the atomic cloud to have a much longer lifetime under strong interaction.

A Lithium 6 experiment mostly works with the lowest three energy states, $|1\rangle$, $|2\rangle$, $|3\rangle$, of which Feshbach resonances between them have been well studied in the past decade. In Figure 2.4, the scattering length between the three states a_{12} , a_{13} and a_{23} are plotted versus the magnetic field [24].

In a cold atom experiment, it is normally preferred to have high interaction for fast thermalization during the cooling stage, so that the evaporative cooling is more efficient. This part is rather easy for ^6Li with the help of Feshbach resonance. However, if cooled with Feshbach resonance, atoms will be bound into pairs that have a low lifetime for a lower magnetic field. As an alternative, evaporation could also be efficiently done with state $|1\rangle|3\rangle$ mixture at 300 G, where a_{13} is relatively large without the formation of molecules.

2.2.1. Feshbach Molecule

Assume the scattering to be much larger than the van der Waals range, meaning very close to the Feshbach resonance, two atoms can form a pair with binding energy [25]:

$$E_b = \frac{\hbar^2}{2m_d a^2} \quad (2.4)$$

where m_d is the mass of the pair and a is the scattering length. When the temperature (kinetic energy) is smaller than the binding energy $k_B T < E_b$, the atom pair will favor the bound state of a Feshbach molecule. Although being named "molecule", it does not possess a strong binding like a regular molecule (chemical binding). This "molecular binding" is extremely weak, as a result, the wave function of the dimer would extend very far spatially. Such phenomenon is also commonly referred to as halo dimer.

Three-Body Recombination

The molecule formation takes place with the process of three-body recombination. During the cooling process, even if the Feshbach molecule is preferred over a single atom, molecular binding can not happen only from a two-body elastic collision. A third particle is always needed such that the binding energy released can be taken away. With $k_B T < E_b$, the third particle will receive a strong kick and most likely be lost from the trap.

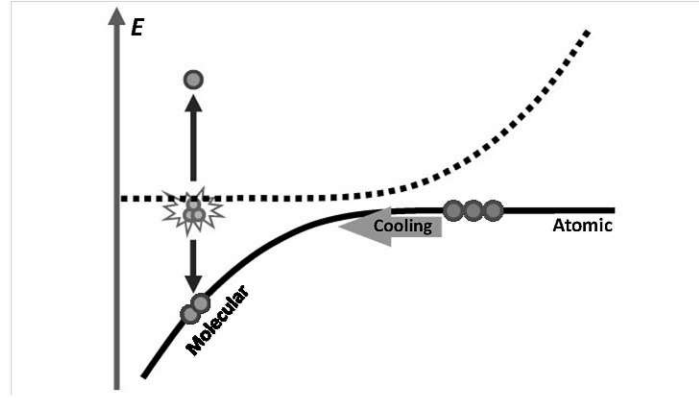


Figure 2.5.: Illustration of a three-body recombination process.

This process has been experimentally measured in Ref.[26].

2.3. Gross-Pitaevskii Equation

In 1961, a mean-field description of a ground-state quantum system was given by Eugene P. Gross [27] and Lev Petrovich Pitaevskii [28] independently. The Gross-Pitaevskii equation (often abbreviated as GPE), named after its creators, soon developed into a powerful tool for researching Bose-Einstein condensates, providing insight description to quantum phenomena such as vortices [29] and solitons [30, 31].

The derivation of this equation could be found in most of the textbooks relevant to the Bose-Einstein condensate. In the following, a simplified approach from the second quantization description is given, as an N-particle system could be written as:

$$i\hbar \frac{\partial}{\partial t} \hat{\Psi}(\vec{r}, t) = [\hat{\Psi}, \hat{H}] = \left[-\frac{\hbar^2 \nabla^2}{2m} + V(\vec{r}, t) + \int d\vec{r}' \hat{\Psi}^\dagger(\vec{r}', t) u(\vec{r}' - \vec{r}) \hat{\Psi}(\vec{r}', t) \right] \hat{\Psi}(\vec{r}, t) \quad (2.5)$$

with $\hat{\Psi}^{(\dagger)}(\vec{r}) = \sum_i \Psi_i \hat{a}_i^{(\dagger)}$ being the sum of all single-particle wavefunctions. Here $\hat{a}^{(\dagger)}$ represents the creation and annihilation operator. This function is numerically too demanding to solve. So the interaction term is rewritten with mean field approximation:

$$i\hbar \frac{\partial}{\partial t} \Phi(\vec{r}, t) = \left[-\frac{\hbar^2 \nabla^2}{2m} + V(\vec{r}, t) + g |\Phi(\vec{r}, t)|^2 \right] \Phi(\vec{r}, t) \quad (2.6)$$

with

$$g = \frac{4\pi\hbar^2 a_s}{m},$$

where a_s denotes the s-wave scattering length.

Equation 2.6 is known as the Gross-Pitaevskii equation.

Although GPE provides a very powerful framework for understanding and predicting quantum systems, it is derived under the mean-field approximation, which may break down under strong interaction. Furthermore, it assumes the overlap of single-particle wavefunctions, which requires the de-Broglie wavelength to be large. This only holds for a system at low temperature, commonly stated as zero temperature approximation.

Dimensional Reduction

In some scenarios, the dynamic of the physical system is mainly contributed by fewer dimensions while other dimensions are frozen out. Applying dimensional reduction over GPE can save the time of calculation while maintaining the accuracy of the result. For example, in Chapter 4, we apply a 1D harmonic potential on an elongated 3D gas. While the dynamics of our interest occur along only one dimension, it is safe to assume that the dynamics could be described as a 1D system, thus with 1D GPE.

To obtain the formalism of 1D GPE, we take the ansatz by separation of dimensions:

$$\Phi(\vec{r}, t) = \psi(z, t)\phi(x, y) \quad . \quad (2.7)$$

Here $\psi(z, t)$ and $\phi(x, y)$ are the axial and transversal wavefunction respectively, while the transverse wavefunction is assumed to be in a transverse ground state, for example, a Gaussian shape:

$$\phi(x, y) = \frac{1}{\sqrt{\pi} a_{\perp}} e^{-\frac{x^2+y^2}{2a_{\perp}^2}} \quad .$$

$a_{\perp} = \sqrt{\frac{\hbar}{m\omega_{\perp}}}$ is the characteristic length of transverse harmonic trap.

By inserting the ansatz back to Equation 2.5 and integrating out dimensions x and y , we arrive at the 1D-GPE:

$$i\hbar \frac{\partial}{\partial t} \psi(z, t) = \left[-\frac{\hbar^2}{2m} \frac{\partial^2}{\partial z^2} + V(z, t) + g_{1D} |\psi(z, t)|^2 \right] \psi(z, t) \quad (2.8)$$

with

$$g_{1D} = \frac{g}{2\pi a_{\perp}^2} = 2\hbar a_s \omega_{\perp} \quad .$$

Note that the assumption of Gaussian shape for transverse ground state is an over simplification that neglects interaction. A better alternative is to assume a variational-Gaussian function, and it leads to the result of 1D nonpolynomial Schrödinger equation

(NPSE) [32]. In the work of this thesis (Chapter 4), we assume a transverse Thomas-Fermi profile.

2.3.1. Thomas-Fermi Approximation

Using GPE we can already produce numerical solutions for a BEC system. However, calculating an analytical solution is still very difficult, as GPE is a nonlinear equation. To conveniently apply it in experiments, we sometimes take additional approximations such that a 'quick' and 'dirty' result can be given directly.

For a stationary BEC, its wavefunction could be written as $\Phi(\vec{r}, t) = \phi(\vec{r})e^{-i\mu t/\hbar}$ and the time-independent GPE read:

$$\mu\phi(\vec{r}) = \left[-\frac{\hbar^2 \nabla^2}{2m} + V(\vec{r}) + g|\phi(\vec{r})|^2 \right] \phi(\vec{r}) \quad (2.9)$$

with μ representing the chemical potential of the system and $|\phi(\vec{r})|^2 = n(\vec{r})$ is the density distribution. In the Thomas-Fermi approximation, we assume a sufficiently large interaction energy, such that we could neglect the kinetic term and the above equation gives:

$$n(\vec{r}) = \frac{\mu - V(\vec{r})}{g} \quad \text{for } \mu \geq V(\vec{r}). \quad (2.10)$$

In our system, the BEC stays within a harmonic trap:

$$V(\vec{r}) = \sum_{i=x,y,z} \frac{1}{2} m \omega_i^2 r_i^2$$

and the chemical potential could be calculated by integrating over the whole cloud $N = \int n(\vec{r}) d\vec{r}$, and the result is [33]:

$$\mu = \frac{\hbar \bar{\omega}}{2} \left(\frac{15Na}{a_{ho}} \right)^{\frac{2}{5}}, \quad \text{with } r_i \leq \sqrt{\frac{2\mu}{m\omega_i^2}}, \quad (2.11)$$

where N is the total particle number, $\bar{\omega} = (\omega_x \omega_y \omega_z)^{\frac{1}{3}}$ is the geometric mean trapping frequency, and $a_{ho} = \sqrt{\frac{\hbar}{2\pi m \bar{\omega}}}$ is the harmonic oscillator length. The range of r is the Thomas-Fermi radius, which is calculated by setting $\mu = V_i(R_{TF})$.

In the regime of Thomas-Fermi approximation, a stationary BEC in a harmonic trap takes the density distribution of a reverse parabolic function. In reality, the approximation fails on the edge of the cloud where the density is low. But it gives a nice prediction of the overall shape of the BEC.

2. Preliminary Knowledge

This result gives a good approximation for an interacting stationary BEC. Figure 2.6 shows the calculated result using Thomas-Fermi approximation plot with experimental measurement over different interaction strengths. It can be seen the calculated result shows a good agreement with the parabolic fitting of the experimental result.

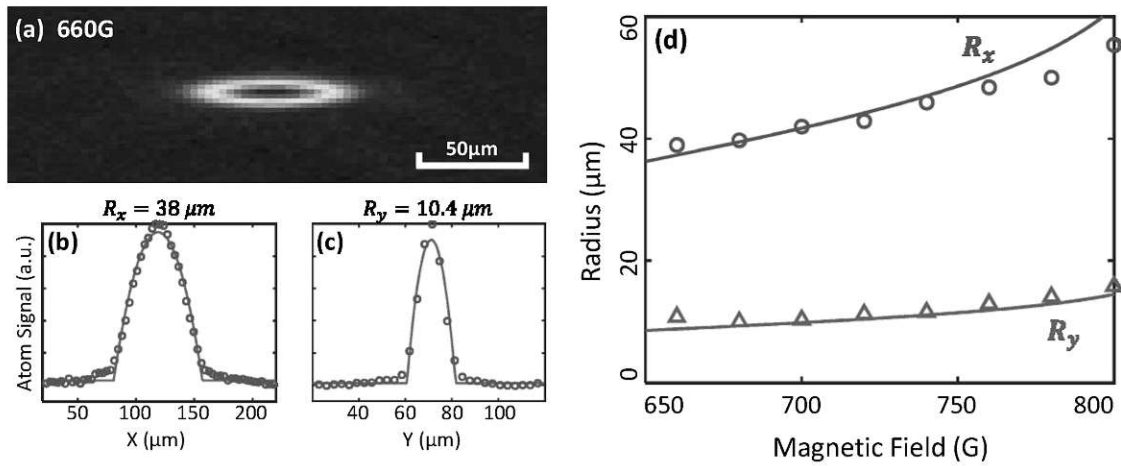


Figure 2.6.: Experimental measurement plot with Thomas-Fermi radius calculation.

3. Experimental Setup

The major task of this thesis is the construction of our experimental platform. The design took inspiration from multiple research groups such as the group of Selim Jochim, Immanuel Bloch, Tilman Esslinger, and many more. The working principle of this experiment (such as MOT, dipole trap) is not explained in detail in this thesis. For a comprehensive description, one could refer to the reviews of Ref [34, 35].

Some parts of the experiment are finished independently as student projects and integrated later into the experiment. References to their thesis works will be given in such scenarios.

3.1. Vacuum System

An overview of our vacuum chamber is shown in Figure 3.1.

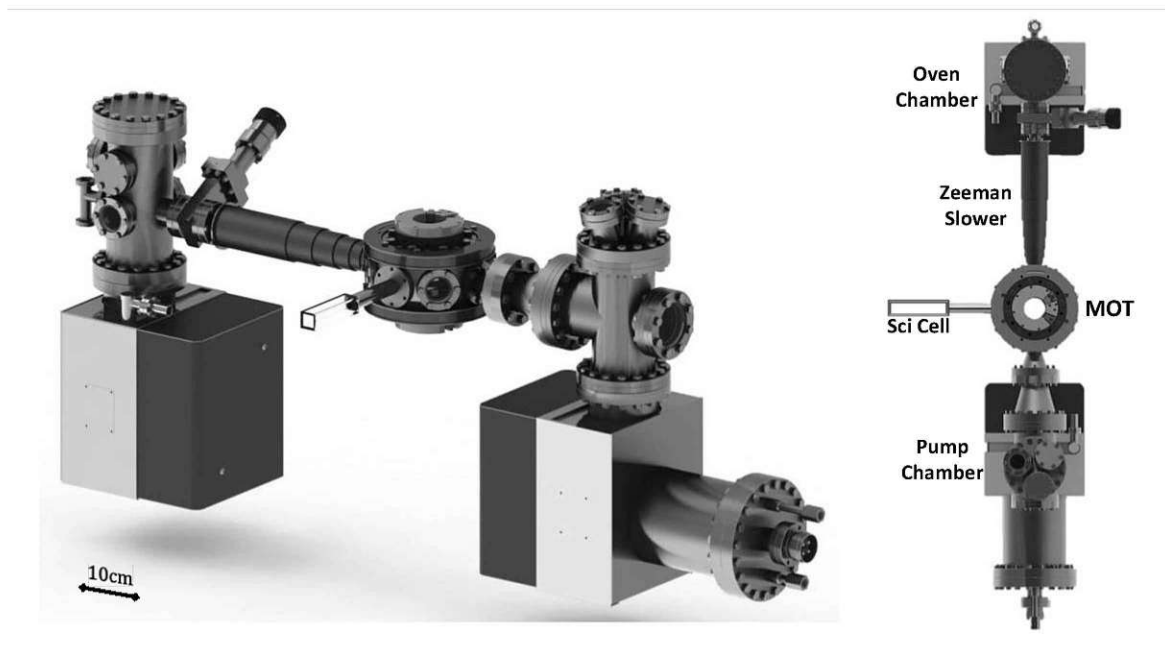


Figure 3.1.: 3D model of the vacuum chamber.

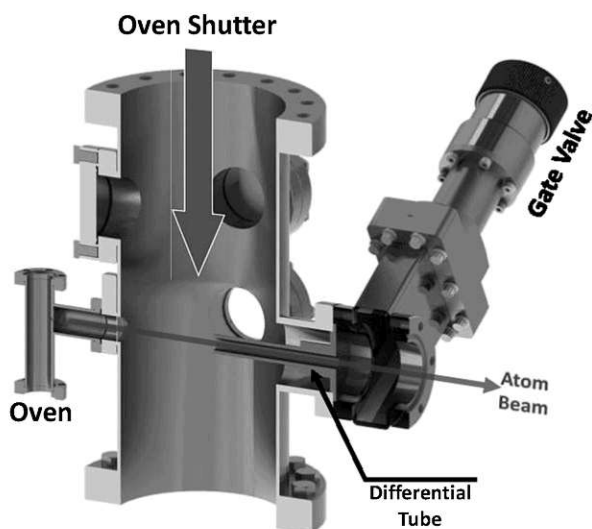
3. Experimental Setup

The vacuum chamber could be seen as three major parts: Oven, MOT, and Science (Sci) chamber. The Oven and MOT chambers are connected via the Zeeman slower tube. With a gate valve, we can isolate the vacuum of the Oven chamber in case of the need for lithium refill.

The vacuum is maintained by two VacIon Plus 150 ion pumps from Agilent Technologies, installed at both ends of the system. One of the ion pumps includes a titanium sublimation pump (TSP), which we activate when the vacuum level is degrading. Above each ion pump, we have installed an angle valve that allows us to pump either side of the system independently, or speed up the pumping process using both sides for the whole chamber.

The experiment achieves a vacuum level of $\sim 3 \times 10^9$ mbar in the oven chamber. In the MOT chamber, the pressure is lower than 10^{-10} mbar, and we read $2 \sim 5 \times 10^{-11}$ mbar with an ion gauge. The vacuum level in the Sci chamber could not be measured directly, so we infer from the lifetime of the atom cloud.

Oven Chamber



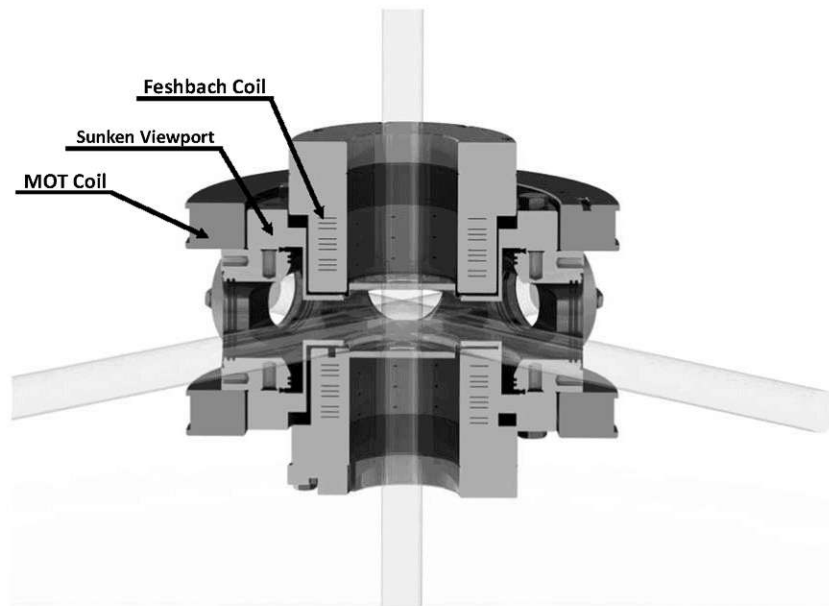
The oven piece is manufactured by Vacom according to our custom specifications. It is loaded with ~ 0.5 g of enriched lithium 6 (purchase from Sigma-Aldrich), and is heated to $\sim 380^\circ\text{C}$. Note that the heating at the oven aperture is rather crucial to

3. Experimental Setup

avoid blocking. After ejecting out of the oven piece, the atom beam is angular filtered by a differential tube, then enters the Zeeman slower. The chamber is also mounted with a linear pneumatic shutter from SVT, which we could move up and down to block the atom beam.

When sealing the vacuum of the oven, nickel-coated gaskets are needed for the lithium container, as lithium could react with copper and corrode the gasket, resulting in a vacuum leak. Since the nickel coating will unavoidably be broken by the CF flange while sealing vacuum, it is crucial to maintain the temperature of oven piece after heating up, as the exposed surface of the gasket would be blocked by the cutting edge itself. In the case of a temperature decrease, the tiny gap created by thermal contraction will allow lithium vapor to sneak in and corrode the gasket slowly. This happened for our experiment during the pandemic lockdown. We only realized this six months later when we could no longer work with the degrading vacuum level and found that the gasket was completely replaced by lithium compound.

Magneto-Optical Trap (MOT) Chamber

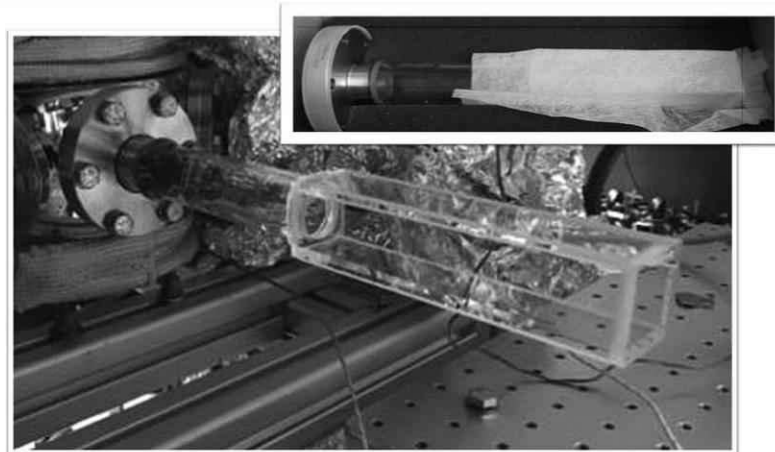


Our MOT chamber uses the 6.0" Spherical Octagon model (MCF600-SphOct-F2C8) from Kimball Physics. Of all seven viewports, six MOT beam windows are coated with 671 nm/323 nm dual wavelength anti-reflection (AR) coating, and the optical

dipole trap window is 671 nm/1064 nm AR coating. The top and bottom windows are custom-designed sunken viewports from Vacom. This allows us to mount our Feshbach coil pair closer to the atom cloud, which is essential to generating a high magnetic field.

Science (Sci) Chamber

Most of the experiments are planned to be conducted in the Sci chamber. To gain a better optical access, we installed a glass cell purchased from Hellma. The cell is made with material called “Spectrosil” from Heraeus, with refractive index 1.45637 at 656 nm and 1.44963 at 1064 nm. After studying the available method, we did not manage to find a satisfying anti-reflection coating option, so we planned our fluorescence imaging beam (Sec 3.21) using the Brewster’s angle. The major drawback of this arrangement is the fringes created from multiple glass surfaces during absorption imaging, which greatly increase the requirement of mechanical stability.



Front Window Protection

Front window coating is one of the common problems that cold atom experiments face when using a Zeeman slower. Since we capture atoms from a slowed atom beam, a large part of the atom flux will eventually end up on the vacuum window where the Zeeman slower beam enters. If not dealt with properly, the transparency of the window will be degraded and reduce the functionality of the Zeeman slower.

There are two common solutions to the coating problem. One is heating the front window to dispose of the attached lithium. The other one is to remove the lithium-coated layer with light-induced atom desorption (LIAD) [36]. When the lithium coating

3. Experimental Setup

is shined with high-frequency (ultraviolet) light, the metal-insulator binding could be stimulated by the high-energy photons similar to the photoelectric effect, such that the lithium layer would be "vaporized". Note that the stimulation only works for metal-insulator binding, meaning that it is very inefficient in removing thick layers of coating. Additionally, a sapphire window would be preferred over a silica window, as lithium could react with glass.

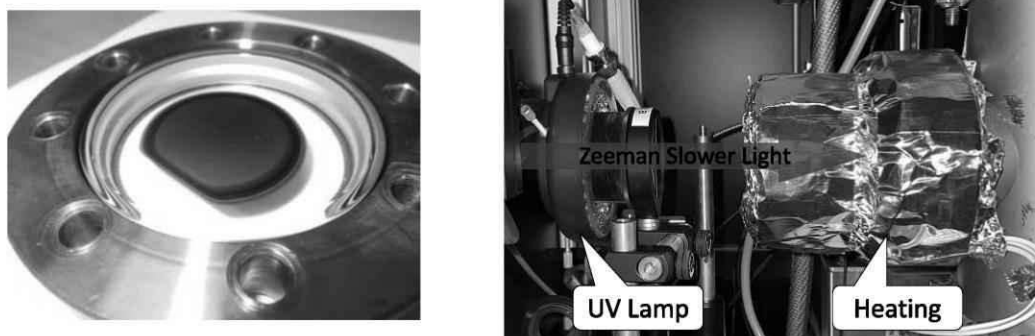


Figure 3.2.: (left) A front window heavily coated by Lithium. The coating takes the shape of the Zeeman slower beam. (right) Front window protection setup with both UV lamp and heating.

In our experiment, we apply both methods together. Two vacuum windows are stacked together to create a small air chamber in between and heated up to $\sim 200^{\circ}\text{C}$. The air chamber ensures uniform heating to avoid cracking. At the same time, an ultraviolet microscope lamp is installed close to the window.

3.2. Magnetic Field Coils

All the field coils used in this experiment, except the Bitter type coil (Sec 3.2.3) and the Zeeman slower, are wound with hollow-cord wire purchased from S&W Wire, with cooling water running through its center. On every coil, we glue a thermal circuit breaker (NGT 05EN-65) with thermally conductive adhesive, which will break the connection when sensing temperature above 65°C . By connecting the circuit breaker in series with the interlock of the corresponding power supply, the coil will be cut from power automatically when overheated.

3.2.1. MOT Coils

The pair of MOT coils are made from 4×5 windings of wire with 176 mm inner diameter, set up in an anti-Helmholtz configuration. With 100 A of current, it is expected to generate a radial field gradient of 12.3 G/cm at the center of the MOT chamber.

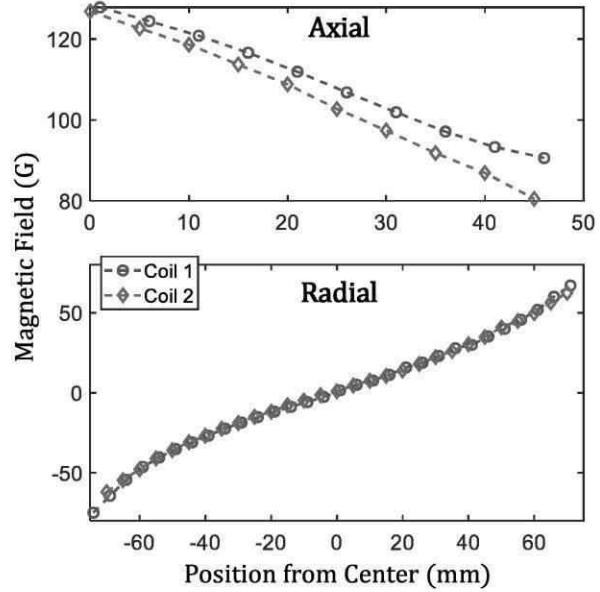


Figure 3.3.: (left) Photo of a MOT coil. (right) Magnetic field measurement in axial and radial direction with 10 A of current.

Two coils are connected in series, with an additional MOSFET connected in parallel with one of the coils. By applying a small voltage to the MOSFET, we could slightly tune the current balance between the two coils, such that the zero crossing of the field could be shifted vertically. This function is useful when we need to fine-tune the MOT cloud position during the loading of the dipole trap.

For absorption imaging of the MOT cloud, we installed a snubber circuit setup (Fig 3.4) for the MOT coil pair such that we could perform a fast switch off of the gradient field. Note that the operation of IGBT and shottky diode require strong cooling, so we water-cooled the whole board. The grounding of this circuit must be taken extra care of, as high current/voltage could go through the wrong ground and damage the power supply.

3. Experimental Setup

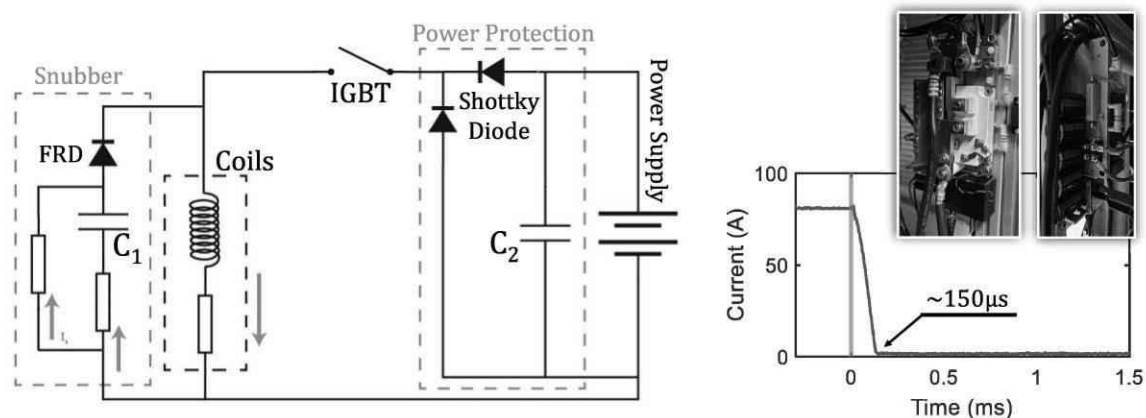
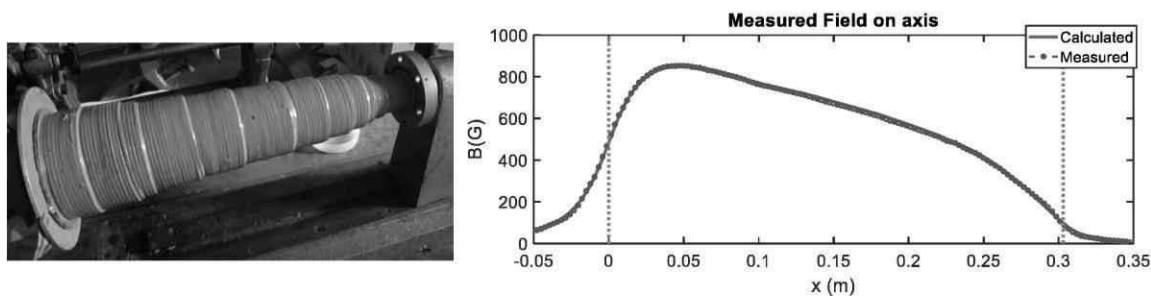


Figure 3.4.: Snubber circuit of MOT coils. Elements used: IGBT, SKM800GA176D; FRD, STTH60L06W; Shottky diode, MBR40040CT; Power supply, Keysight N8754A. Capacitor C_1 should be built from polypropylene film capacitors. Capacitor C_2 needs to be large in capacitance, so aluminium capacitors are preferred. IGBT driver built with chip MC33153PG. We measure the turn off time to be $\sim 150 \mu$ s.

3.2.2. Zeeman Slower

The Zeeman slower is designed to run with a maximum 10 A of current, so water cooling through the hollow-cord wire would be excessive. Instead, we run cooling water through the water channel within the tube. Between each layer of winding and the tube itself, we brush a layer of paste (LP-VU-4675, Putz Drucktechnik) to ensure thermal conductivity and electrical isolation.

More details on calculation and design are available from the bachelor thesis of Lukas Heller [37].



3.2.3. Bitter Type Coil

In order to generate the required high field for accessing the Feshbach resonances in the MOT chamber, we have to employ this special design of magnetic coil. The Bitter type coil, invented by Francis Bitter in the 1930s, combines a structure of compact copper disk with efficient water cooling channels, allowing operation with high current. We consulted Dr.Dylan Sabulsky and slightly modified the design from Ref.[38] according to our needs, as shown in Figure 3.5.

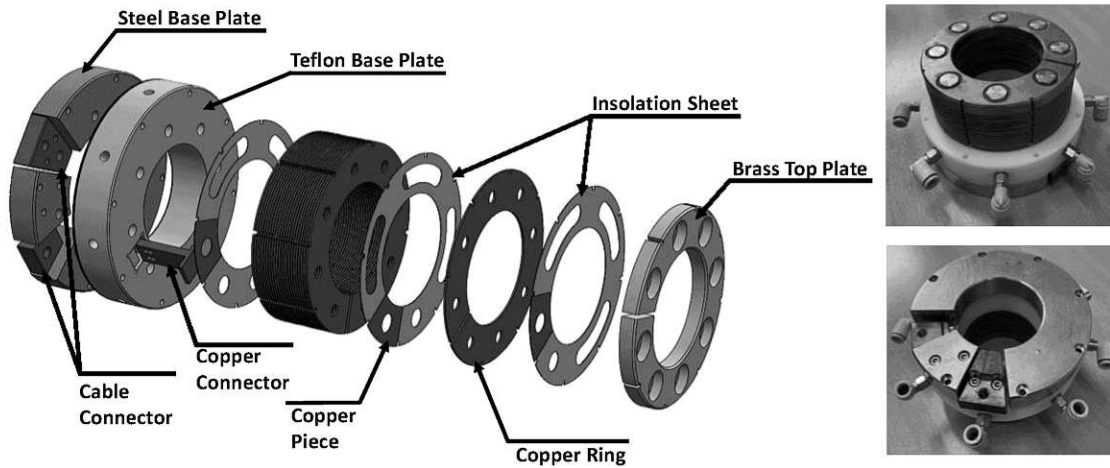


Figure 3.5.: Schematic (left) and photos (right) of the Bitter type Feshbach coils

Our Bitter-type coils consist of 24 layers of copper rings, insulated by plastic sheets in between. Every layer is made with 8 holes around the ring sealed by rubber gaskets, such that water can flow through. After laminating all copper and plastic disks alternately, the structure is compressed by slowly tightening 8 long screws. 7 of the screws are made of non-magnetic steel which contributes most of the force for compression. The other one is a conductive copper screw that connects the top plate to the cable connector. The progress of compression can be checked by measuring the thickness of the coil, which is crucial to the water tightness of the cooling channels. We measured our coil pair generating 2.78 G/A of magnetic field at the atom location.

3.2.4. Sci-Coil Sets

At the Sci chamber, we take advantage of the glass cell and build the Sci coil sets very close to the chamber, such that the coils are 1 mm away from the glass surface. As shown in Figure 3.6, we have prepared 3 sets of coils. The single coil at the front is the Gradient coil, which we used to give phase shift to the atom cloud (Sec 4.2.2). The

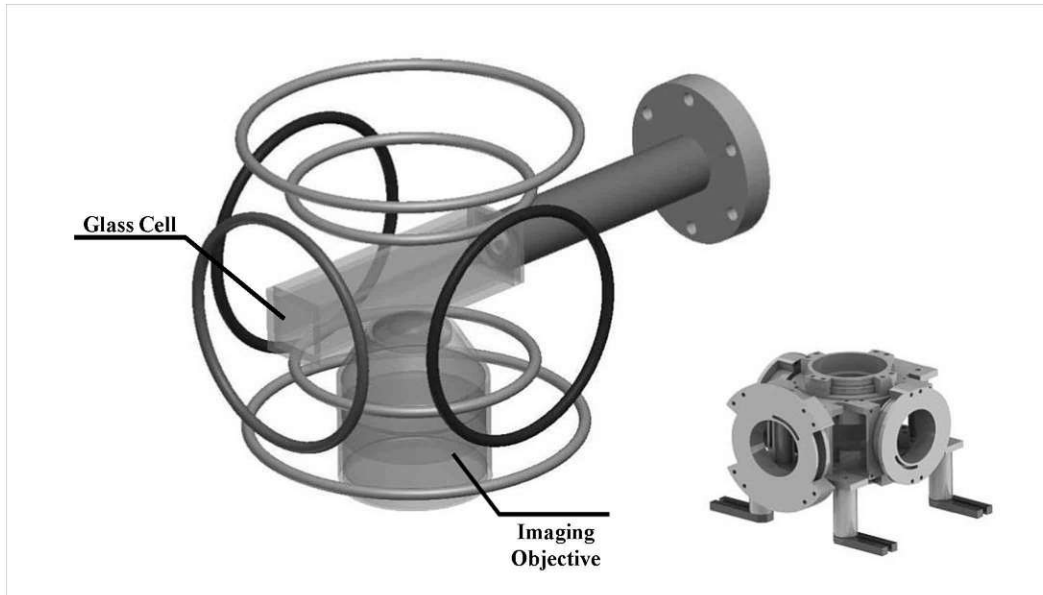


Figure 3.6.: The schematic and 3D model of the coil sets at Sci-Chamber. The coil sets are referred to as Gradient (green), Stern-Gerlach (blue) and Feshbach (yellow) in this thesis.

horizontal coil pair is the Stern–Gerlach coil. As stated by the name, they are planned for the generation of a gradient field. The vertical coil set is the Feshbach coils. Here we use two Helmholtz coil pairs for the purpose of producing field quenches (Sec 3.2.5). The primary (inner) pair was designed to run with maximally 400 A of current and generate 1100 G of field (2.75 G/A). This provides the necessary Feshbach field for evaporative cooling and covers a sufficiently large range of the Feshbach resonances. The quench (outer) coils, further away from the atom, are capable of 300 G. For different experimental needs, we can change the connection for a magnetic field quenching up or quenching down.

In the work of this thesis, the Stern–Gerlach coil sets are not installed, such that the optics could be placed closer to the Sci chamber.

3.2.5. Fast Switching of Magnetic Field

In some scenarios, the experiment requires a fast switching of the magnetic field, such that we could quench the interaction of the system or even quench across the BEC-BCS crossover.

To rapidly switch off current, the common approach is to use a snubber circuit. A typical snubber circuit consists of three elements: fast recovery diode, charge capacitor and dump resistor. When the coil (inductance) is switched off, the inductor and

3. Experimental Setup

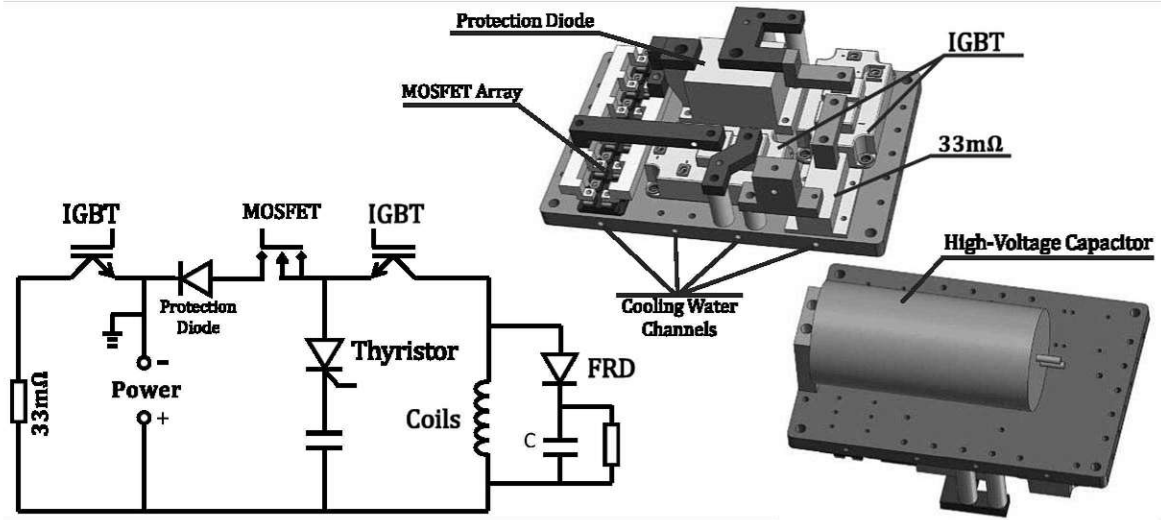


Figure 3.7.: The circuit diagram and 3D model of the fast switching circuit. The whole setup is mounted on a copper board that contains cooling water channels. All connections on the board are made with copper blocks to reduce inductance.

capacitor will form an LC circuit, and the energy in the coil will flow to the capacitor. However, unlike a typical LC circuit, after the energy exits the coils, it would not flow backward because the reverse current is blocked by the fast recovery diode. The energy transfer to the capacitor will then be slowly damped into the resistor. The switch-off time of the coil in such a system can be calculated by the quarter period of the LC circuit: $\tau = \frac{1}{4\sqrt{LC}}$.

To rapidly switch on current, one just reverses the processes of the snubber circuit. A capacitor is pre-charged with high voltage. Then by connecting the capacitor and

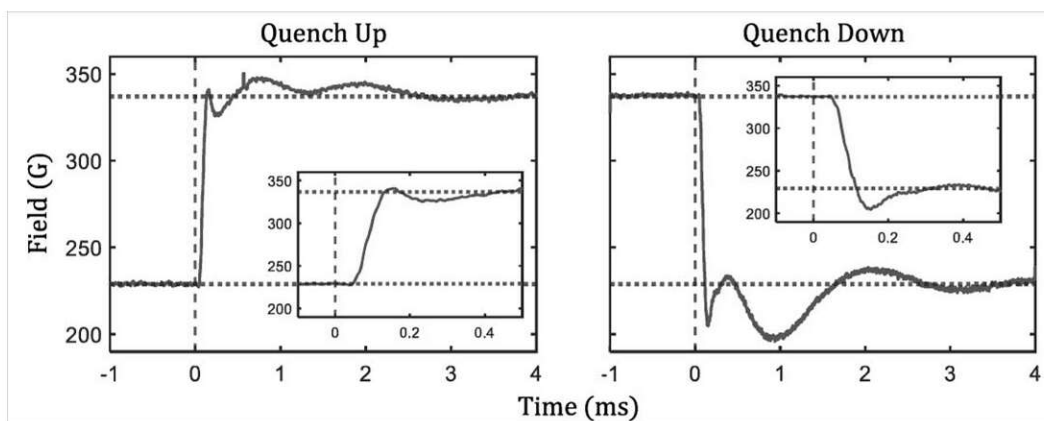


Figure 3.8.: Magnetic field quench by generating a fix field from the primary coils and quenching the quench coils. Magnetic field measured with Gaussmeter.

coil, current will flow through the coil within the quarter period of the LC circuit. When the current (equivalently voltage) level reaches the desired value, the power supply takes over the output. To compensate the responds of the power supply, we include a dummy load resistor ($33\text{m}\Omega$, Fig 3.7) for pre-activation. The power supply will turn on to the desired output before the quench, which greatly reduce the required turn on time.

The theoretical picture of fast current switching is rather straightforward. However, in real applications, lots of issues could complicate the situation. First is the induced voltage. From the property of inductance, we know the induced voltage is proportional to the rate of current change $V_{in} = L \frac{dI}{dt}$, meaning faster switching results in higher voltage. In order to prevent damage to the power supply and switches, extra electronic components such as Schottky diodes are needed. Second is the response time of different electronic components. The IGBTs, thyristors and diodes are likely manufactured differently even for the same types of components. During the turn-on and turn-off processes, microseconds of difference in response time could already induce current oscillation as well as spikes in the circuit. In some cases, we externally program a microcontroller (Arduino device) to fine-tune the operation sequence time.

3.3. Laser System

There are mainly three wavelengths that are involved in this experiment, 671 nm (D2 transition), 323 nm (narrow line transition) and 1064 nm (optical dipole trap). In this section, I will present the layouts of laser arrangement and functionality of all the above.

D2 Laser: 671 nm

The arrangement of the 671 nm laser has actually gone through several major changes during the progress of the experiment. The lasers we purchased from TOPTICA have severe issues with their laser diode, amplifier and electronics. We have had our laser system sent for repair in total 11 times, and it is not until a year and a half later that we are able to lock to the transition stably, while the laser is giving far lower power than the product specification. As a result, most of the "non-optimal" choices that are made in the design were caused by the limitations of the laser.

The laser system for the D2 transition consists of three lasers manufactured by TOPTICA, which are TA-pro (Master), BoostA and DL-pro (Imaging). TA-pro and DL-pro are controlled by the DLC-pro controller of TOPTICA with locking function,

3. Experimental Setup

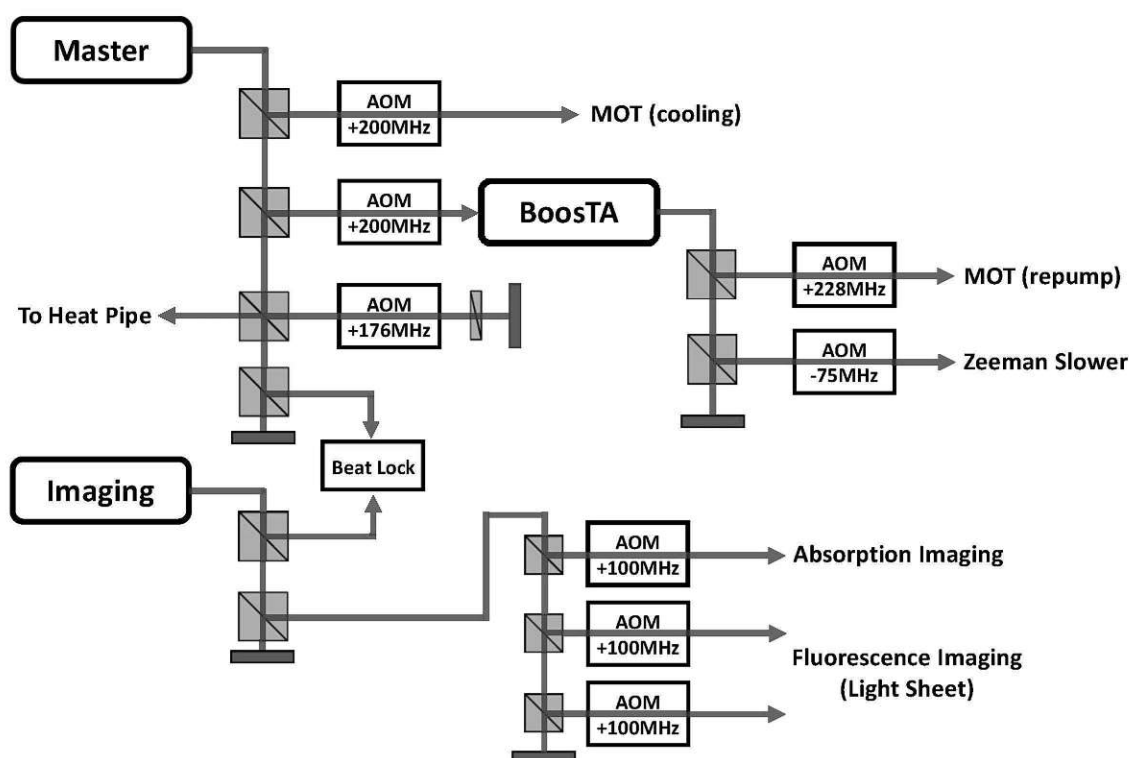


Figure 3.9.: Schematic of 671 nm laser system.

while the BoosTA controller requires an external computer. The master laser is frequency-locked to a lithium heat pipe using saturation spectroscopy, and the imaging laser is offset beat-locked to the master laser.

Limited by the laser output power, we chose to build the system with AOM single pass except for the lock AOM. The original plan was to shift the laser frequency by shifting the frequency of the lock. However, the locking capability provided by the DLC pro controller can not fulfill our requirement of frequency shifting for the MOT compression. So alternatively we unlock (and hold) the TA-pro laser with a TTL signal to the controller digital I/O port (MC+ Module Digital I/O Input #0, Pin #15¹), then the laser frequency is pushed with an analog voltage to the 'DC Modulation' port of the laser². After MOT compression, the laser is shifted back and locked again.

¹Note that some manual may give a different pin assignment configuration, some versions of the manual are wrong.

²This will directly modify the diode current without any safety protection, be cautious about the voltage limit of input.

Saturation Spectroscopy

Saturation spectroscopy, also known as Doppler-free spectroscopy, is a commonly used technique in cold atom physics, as it can probe and resolve optical transition free from the Doppler broadening effect. By sending a high-intensity beam through the vapor cloud, normally called the pump beam, the atoms that are resonant with the pump beam will be saturated. Then a low-intensity beam with the same frequency, normally called the probe beam, would pass through the vapor as if the cloud is transparent. By having the pump and the probe beam counter-propagate, the transparent window will only show when the addressed atoms have no Doppler shift toward either of the laser beams, hence the term 'Doppler-free'.

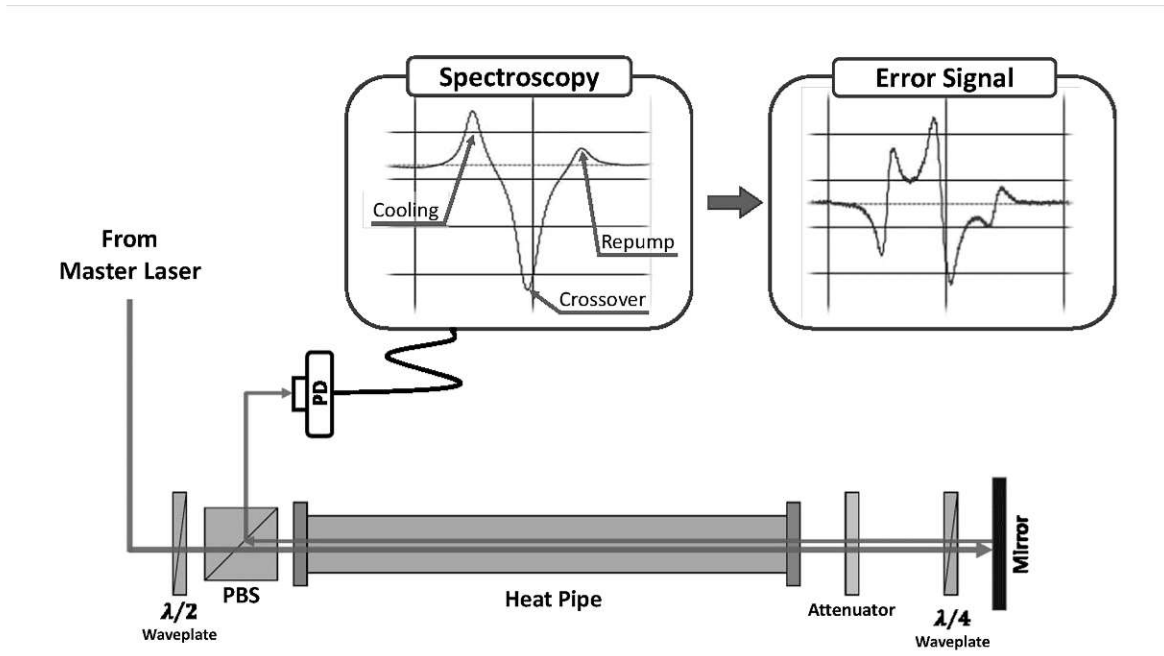


Figure 3.10.: Schematic setup of saturation spectroscopy, with the measured spectrum and error signal.

As shown in Figure 3.10, in our experiment, we chose to retro-reflect the same laser beam. The probe beam is created by attenuating the reflection of the pump beam. With the beam path separated using a polarizing beam splitter (PBS), the probe beam is detected by a photo-diode (PD). The saturation intensity of ^6Li D2 transition is 2.54 mW/cm^2 . We adjust the pump beam to be $\sim 2 \text{ mW}$ and 1.5 mm in diameter. The attenuator is an optical density one (OD1) neutral density filter, so the probe beam is about 1% of the pump intensity. The spectroscopy is then generated by sweeping the laser frequency across the resonance. For the D2 transitions, we will see the two

transition peaks separated by 228 MHz (Figure 2.1 and Figure 3.10). In our experiment, we lock the laser on the cross-over of the two peaks.

Frequency Offset Lock

To generate resonated light for experiments under different interactions/fields, the imaging laser needs wide tunability in laser frequency. For imaging from zero field to high field (1000 G), the imaging laser would span over 2.4 GHz of range. We achieve this range with an offset lock circuit designed and built by Andrzej Pelczar from our electronic workshop. Design details can be found in the bachelor thesis of Sophie Höller [39].

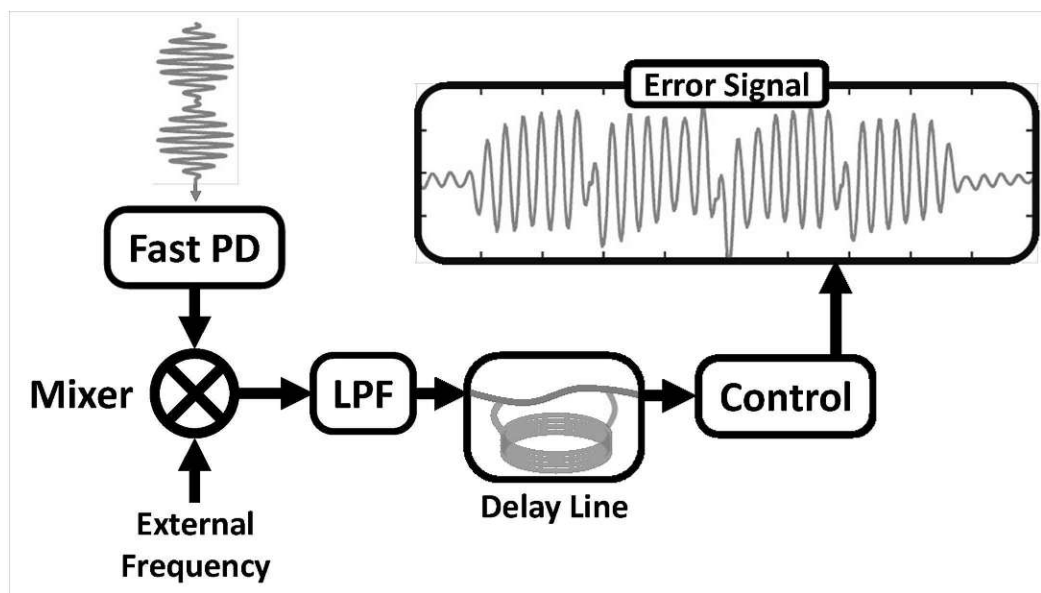


Figure 3.11.: Schematic of offset frequency lock.

As shown in Figure 3.11, both the master laser and the imaging laser light are collected with a fast photodiode G4176 from Hamamatsu. When the frequency of two lasers is relatively close (~ 5 GHz), we could collect the beating signal and mix-down with an external frequency to generate an error signal. This way, we could lock the imaging laser with a frequency offset from the master laser, and the offset could be adjusted easily by shifting the external frequency. We choose a scheme where the laser is matched to ~ 500 G when the mix-down signal is close to DC. Because of the limitation of electronics, the circuit could not function properly in the low-frequency range $[-180 \text{ MHz}, 180 \text{ MHz}]$. As a result, we lost the ability to image in this particular field range, and the locking range is separated into low field $[-1.2 \text{ GHz}, -200 \text{ MHz}]$ and

3. Experimental Setup

high field [200 MHz, 1.2 GHz]. However, Feshbach molecules have a very low lifetime below 500 G, so there is no plan for imaging in this range for experiments with bosonic molecules.

At the beginning of every experiment cycle, the control program (Sec B) will calculate the required offset frequency according to the imaging magnetic field and the atomic state to be imaged. Then the frequency ramp is sent to the local oscillator and push the imaging laser. From testing, our offset lock system is capable of following a frequency ramp up to ~ 2 MHz/ms. We set the ramp speed to be 1 MHz/ms to ensure stability.

UV Laser: 323 nm

Generating UV laser light is in general challenging. The commercial products available to us are very limited. So in our experiment, inspired by [40] and with help from Christian Gross and Ahmed Omran, we built our own 323 nm laser system from Keopsys 1110 nm (CYFL-KILO-05-LP-1110) and Keopsys 1550 nm (CEFL-KILO-05-LP-W15) lasers with two stages of conversion.

As shown in Figure 3.12, first, we combine lasers of the two wavelengths through a Periodically-Poled Lithium-Niobate (PPLN) crystal, where 646 nm is generated by Sum-Frequency-Generation (SFG) process. Secondly, the 646 nm light is sent through a Beta-Barium-Borate (BBO) crystal inside an enhancement cavity, and the Second-Harmonic-Generation (SHG) converts 646 nm light into 323 nm light. To increase the efficiency of SHG, the BBO crystal is set up within a bow-tie cavity.

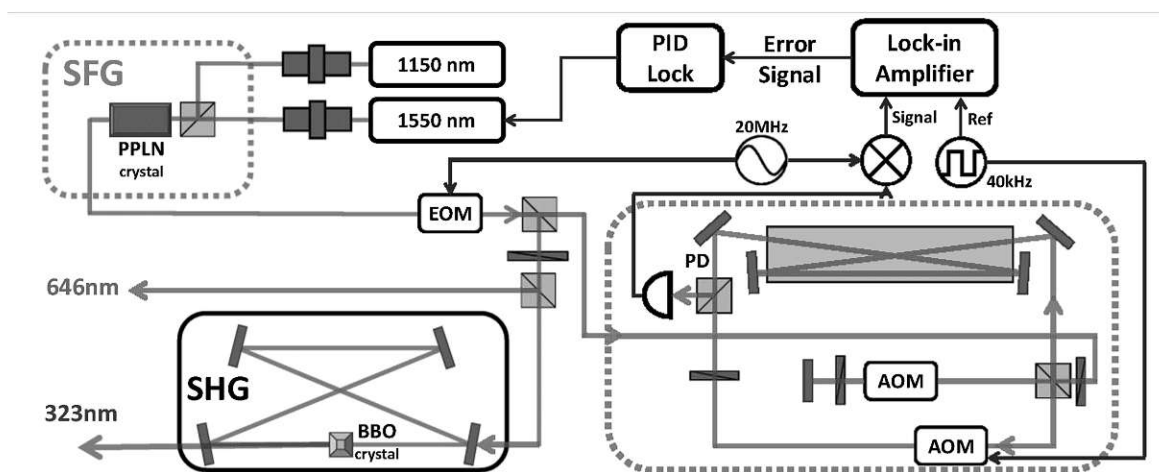


Figure 3.12.: Schematic of the UV generation setup. There are three major parts of the system: Sum frequency generation (SFG), Second harmonic generation (SHG) and Iodine spectroscopy locking.

Iodine Spectroscopy

There are two possible approaches to lock the frequency of the UV laser. The straightforward way is to produce spectroscopy of UV transition with a lithium heat pipe similar to our D2 laser. This approach requires a constant output of 323 nm light, which is damaging to the lifetime of BBO crystal. To save the trouble of frequently exchanging the crystal, we employ the technique of Iodine spectroscopy [41]. As shown in Figure 3.12, we generate the spectroscopy of Iodine using the intermedia 646 nm light, with a similar working principle to saturation spectroscopy. The laser is modulated by 20 MHz using an EOM, and the probe light is then mixed down with the modulation reference to generate the spectroscopy. However, the Iodine transition line we accessed is much weaker than the D2 transition, so some special technique is required to extract the spectroscopy signal. We choose to chop the probe beam at 40 kHz and use Lock-in amplification to extract the signal. Then, through a PID circuit, we lock the frequency of the 646 nm light by tuning the 1550 nm laser.

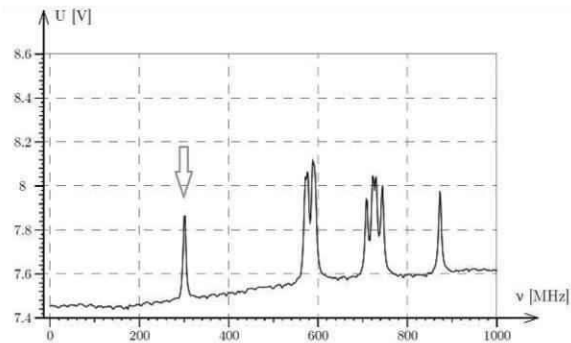


Figure 3.13.: Iodine spectroscopy. Arrow marks the lock position.

In this experiment, the Lock-in amplifier we use for the error signal is a Red-Pitaya 125-14 FPGA with STEMLab application. To monitor the lock, we installed and synchronized a second FPGA unit to monitor the spectroscopy.

Dipole Laser: Infra red

We chose 1070 nm for our dipole trap to take advantage of Lithium 6 magic wavelength, and the drawback is the requirement of laser power, since the detuning is very large $\delta = 393$ nm. Luckily, the technology relative to this wavelength is very well-developed, and we have available options to choose from. There are three inferred lasers used in this experiment:

3. Experimental Setup

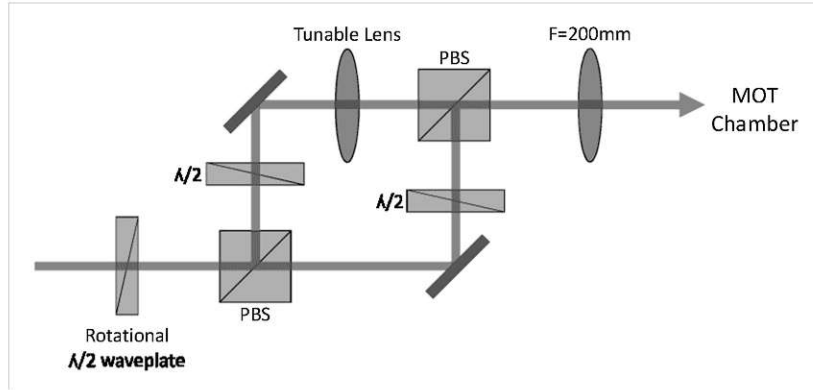
Laser	λ (nm)	P (W)	M^2
IPG Ytterbium Fiber Laser	1070	200	1.1
NKT Koheras BOOSTIK	1070	4	1.05
Coherent Mephisto + Nufern Fiber Amplifier	1064	60	1.1

The IPG laser (YLR-200-LP-WC) is capable of generating power up to 200 W. We normally use it up to 150 W to form the initial dipole trap of ~ 1 mK, so that we could load atoms from the MOT. The linewidth of this laser is 2.5 nm, which is not of concern for dipole trap, but impossible to use for optical lattice. As a result, we only used the IPG laser on the "MOT" side of the experiment and transported to the Sci-chamber. Note that the power level of this laser is very high (The lowest constant output of IPG is 20 W), all optics involved need to be specially chosen, and the laser light needs to be properly blocked and the beam dumped properly cooled.

The other two lasers are used on the Sci-chamber side for the Capture beam (Sec 3.3.1) and optical lattice (Sec 3.3.2), which will be explained in more detail later.

3.3.1. Optical Transport

To move the atom cloud from the MOT-chamber to Sci-chamber, we employed an optical transport scheme similar to Ref.[42]. With a lens setup that includes a tunable focus lens, we are able to transfer the atom cloud over a spacial distance of ~ 300 mm.



After testing in the experiment, we found out that although the tunable lens has a high-intensity damage threshold, it does not function normally under high laser power. We believe it is caused by the thermal heating of the lens liquid by laser light, which is also consistent with the long-term measurement of the focus positional drift (Figure 3.14). From our testing, the maximum laser power that the tunable lens could

3. Experimental Setup

work with is ~ 6 W. To be on the safe side, we choose 2W of laser power for optical transport.

The dipole beam is separated into two arms by a polarizing beam splitter (PBS) and recombined before the last lens. The tunable lens is installed in the transport arm such that it is safe from thermal damage during the high power stage. Note that the tunable lens surface has to be orientated perpendicular to gravity, such that the liquid lens would stretch the membrane evenly to maintain a good spherical shape. After we evaporate down to 2W of laser power, the rotational waveplate (Appx C) is turned and all power is transferred into the transport arm. The tunable lens is initialized with zero focal power (flat surface), so the dipole trap would be stationary during the transfer. Then by decreasing the focal power (shift into a concave lens), the focus of the dipole laser is pushed towards the Sci-chamber.

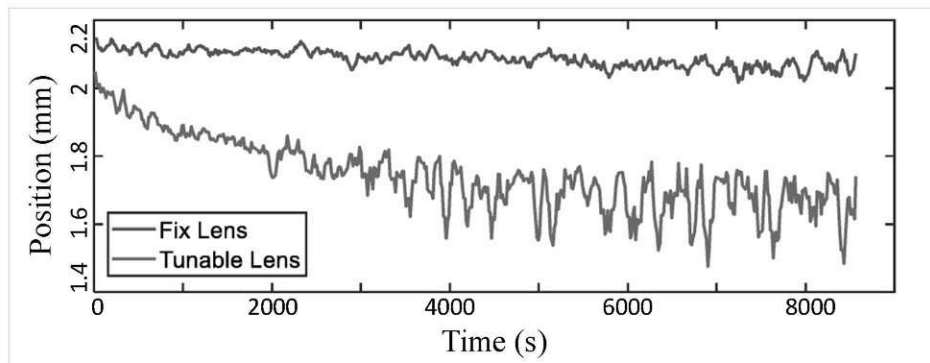


Figure 3.14.: Stability measurement by holding the atomic cloud in dipole trap, measured with 2W power. Each measurement circle is 15 s. A clear drift over time can be seen when forming the dipole trap with the tunable lens. Furthermore, the lens starts to show instability after 1 hour of long exposure operation.

From our measurements (Fig 3.14), the transport setup is not stable enough for holding the atoms or performing evaporation. We believe that the instability originated from the heating effect of laser onto the lens liquid, which can not be corrected by temperature calibration¹. So on the Sci-chamber side, we have a dedicated dipole beam to 'capture' the atom from transport, and we refer to it as the Capture beam.

¹The tunable lens contains a built-in temperature sensor to calibrate for the thermal drift of the coil when running current. The temperature read from internal sensor only indicates the coil.

Tunable Focus Lens

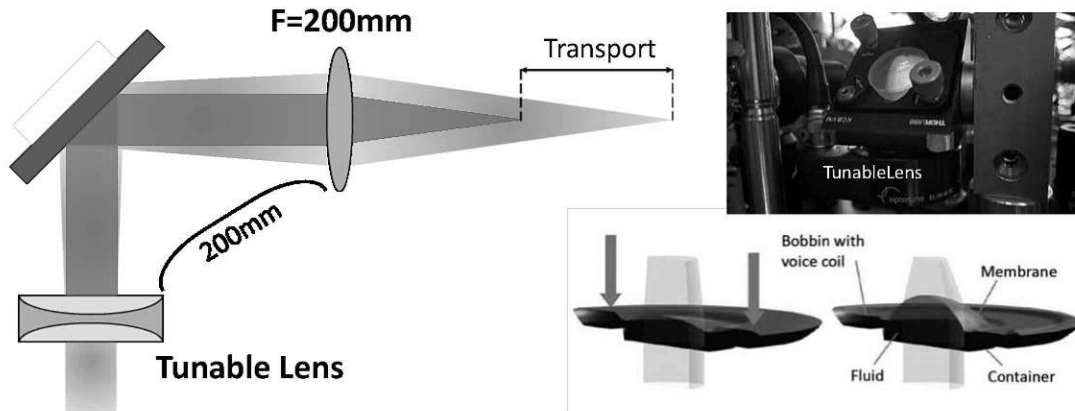


Figure 3.15.: (left) Schematic of moving focus setup. (right) Working principle of the tunable lens (Adapted from the manual provided by Optotune).

The tunable focus lens functions by applying current to a shape-changing polymer, which stretches the membrane that contains the refractive liquid. For a current range of $\pm 300\text{ mA}$, the lens could change optical power in a range of $\pm 10\text{ dpt}$. It is equipped with a USB-connected microcontroller such that the focal length can be controlled from a computer program while calibrated for the temperature drift of the polymer.

However, the controller does not perform with enough resolution for the experiment, so we built our own current supply and controlled it with external voltage (Figure 3.16),

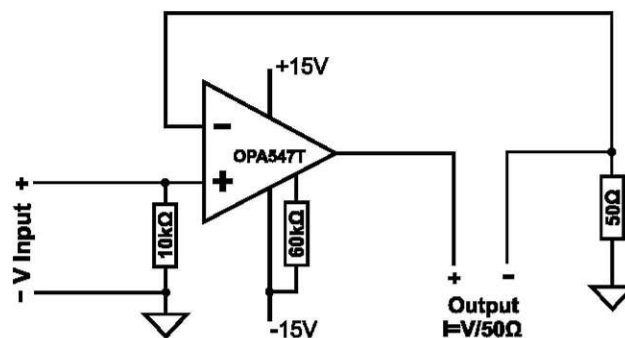


Figure 3.16.: Schematic of a voltage-controlled current source built base on a power operational amplifier (OPA547). This circuit is capable of stability up to 0.01 mA , where the constraint comes from the stability of the resistance (50Ω). We chose a power resistor and connect it to a heat sink.

while applying temperature feedback to the experiment control program using the USB microcontroller.

Stabilizing Atom Transport

Although adiabatic transport is theoretically possible, heating during a long distance moving is unavoidable in reality. At the same time, the atom cloud is also restricted by a lifetime, which means the transport time can not be too long. So, the transport path is preferred to be both "fast" and "smooth".

To estimate the best trajectory of transport, we can take a highly simplified model of a moving pendulum. The position of the atom can then be calculated as [43]:

$$x(t) = x_{trap}(t) + \frac{1}{\omega_{\parallel}} \int_0^t \sin(\omega_{\parallel}(\tau - t)) \ddot{x}_{trap}(\tau) d\tau, \quad (3.1)$$

where x_{trap} is the center position of the trap, ω_{\parallel} is the trap frequency along the transport direction. The oscillation amplitude of the atom cloud (basically heating) induced by moving can be calculated by the Fourier transform of the transport velocity profile:

$$A = \left| \int \dot{x}_{trap}(t) e^{-i\omega_{\parallel}t} dt \right|. \quad (3.2)$$

Taking different schemes of constant velocity, constant acceleration or constant jerk (the first, second or third order derivative of trajectory), the oscillation amplitude could always give a zero heating ($A = 0$) solution. However, the tolerance increases for higher-order derivative cases. In this experiment, we chose the trajectory with constant jerk, and the optical transport is done within 800 ms.

3.3.2. Optical Lattice

By overlapping two laser light beams, a periodic dipole potential would be created by interference. The use of such technique could be dated back to the 1980s, with research around scattering phenomena and atom interferometers. After the development of Bose-Einstein condensates, the periodic potential, also called an optical lattice, makes its first appearance in an ultra-cold atom experiment for demonstrating the squeezed state [44], and later the Mott insulator transition [45]. The tunability of optical lattice allows research of many quantum phenomena and condensed matter systems, which makes it a popular tool among cold atom experiments.

In this thesis, as shown in Figure 3.17, a 1064 nm laser beam is equally spilled into

3. Experimental Setup

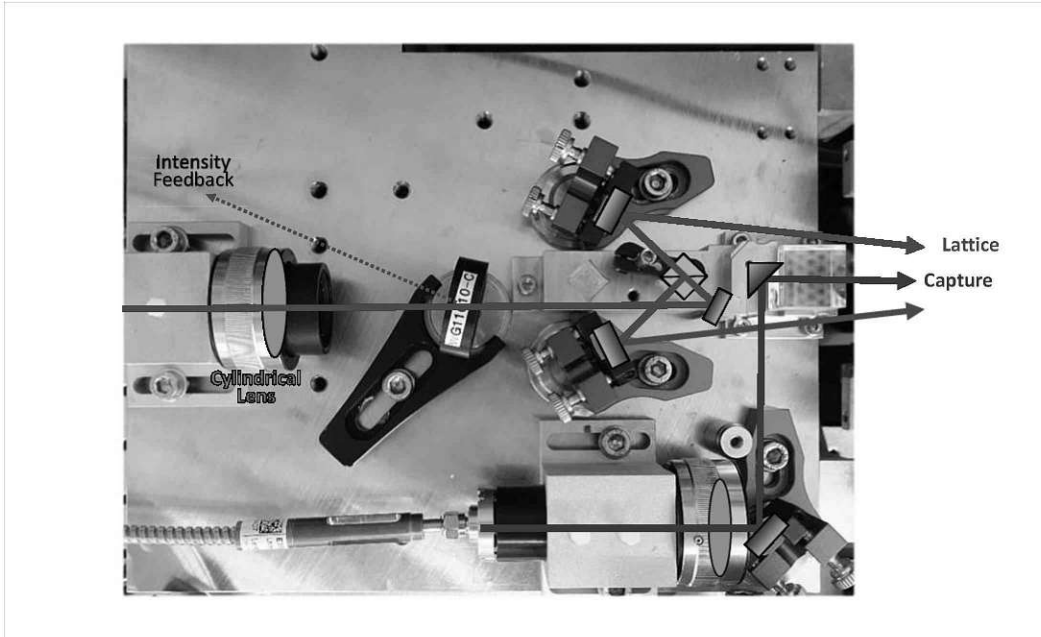


Figure 3.17.: 1064 nm is split with a non-polarized beam splitter, and focused with a 250 nm cylindrical lens. We use an AR-coated glass plate (WG11010-C from Thorlab) to reflect a small portion of light for power monitoring.

two beams and crossed at atom position with an angle of $\theta = 15^\circ$. The lattice period can be calculated as $D = \frac{\lambda}{2 \sin(\theta/2)} \approx 4 \mu m$.

Our lattice setup is built on a single non-magnetic stainless steel board, such that relative motion and drifting between optical elements could be reduced. The stability of the lattice setup used in this thesis is tested externally with a camera mounted ~ 4 m away from the lattice board, such that the interference fringes could be large enough to be recorded. According to the result shown in Figure 3.18, the relative phase of the lattice drift for $\sim 0.3\pi$ in 3 hours time. This gives a lower bound for the instability of the lattice board, and we believe the major cause is the airflow in the optical path.

Additionally, a capture beam setup is aligned along the lattice beam, such that we can rotate the direction of capture when needed, for example, if we want to load the atom cloud into a signal layer of the lattice. The capture beam goes through a dichroic cube that separates 1064 nm and 671 nm before entering the chamber. This allows us to insert an on-resonance beam from the other side of the glass cell to perform imaging.

We have also planned for a lattice board made out of 'Zerodur'. This is a special material whose coefficient of thermal expansion equals zero, such that the lattice setup will be temperature insensitive, and supposedly create much less phase fluctuation. However, the manufacturing and processing of Zerodur is very difficult because of

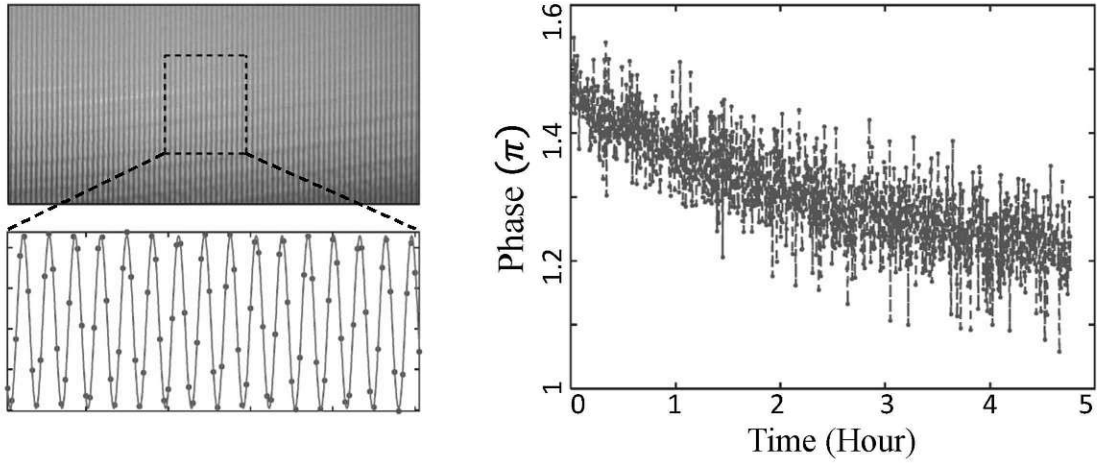


Figure 3.18.: Lattice stability test. (left) Camera imaging and fitting result. (right) Continuous measurement of long-term phase drift.

its glass nature. Every optical element on the board has to be glued with a special adhesive. For convenience, the Zerodur board was not used in this thesis.

Calibrating Lattice Depth

Theoretically speaking, the depth of the lattice potential can be calculated directly from the laser setup. In reality, lots of factors will influence the trap depth, such as power balance, polarization, beam overlap, etc... So in the experiment, we infer the lattice potential depth by measuring the evolution of momentum distribution subject to a lattice pulse.

The working principle of this measurement is based on the solution to the Kapitza-Dirac scattering process (Sec 4.1.1). In a simplified description, the atom cloud will split into different momentum modes after a short lattice pulse, and the population of each mode evolves according to the zeroth order Bessel function. This means for a lattice pulse, the 0th momentum mode will reach the first zero population point when the pulse length equals $\tau \approx \frac{4.8\hbar}{U_0}$ (U_0 is the lattice depth). By scanning the pulse length at different laser power settings, we could obtain the relation between power and lattice depth. This approach is also very useful when aligning the lattice laser.

3.3.3. Speckle Potential

In the experiment presented in Chapter 5, it is required to create an atom cloud far from equilibrium, where momentum distribution is broad and over-occupied in high

3. Experimental Setup

momenta. We achieve the preparation of such an initial state by the use of speckle (random) potential to excite a wide range of momentum modes. This technique has already been used in cold atom physics for creating random potential [46] and phase disorder [47].

There are several approaches to understanding the working principle of the speckle potential. For a comprehensive description and theoretical calculation, one could refer to an optics textbook such as [48]. Here I present a qualitative description.

When a laser beam passes through a diffuser (speckle plate), the diffused laser beam (speckle beam) can be seen as the combination of many coherent laser beams, spreading evenly in space. When the speckle beam is focused, each pair of these "coherent laser" beams would form an optical lattice of its own, with a lattice vector perpendicular to the direction of beam propagation. During a speckle pulse, countless "lattices" excite the cloud according to their own lattice vector, which in the end creates a board excitation. The cutoff of the excitation is then given by the largest "lattice vector" generated with the maximum angle of focusing, which is related to the numerical aperture (NA). An approximated calculation can be given by:

$$\sigma = \frac{\lambda}{2NA} \quad , \quad (3.3)$$

where λ is the wavelength of the laser. σ denotes the root-mean-square width of the autocorrelation function of speckle potential, more commonly referred to as speckle grain size.

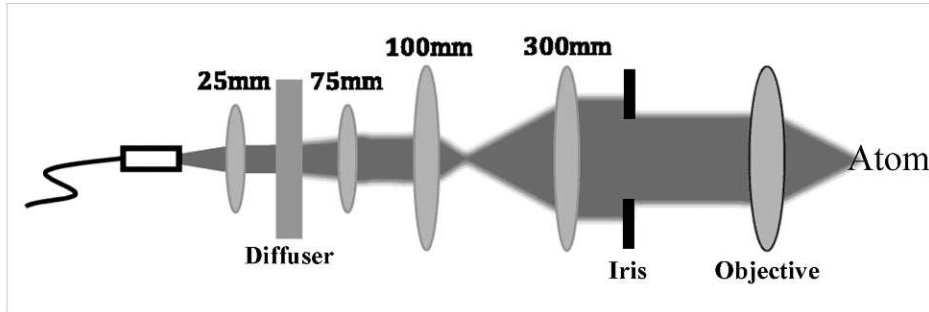


Figure 3.19.: Schematic of the speckle beam setup. The iris can be used to change the effective NA of the speckle potential, and thus the speckle grain size.

In this thesis, we take the convenience and use the 646 nm intermedia output of the UV system (Sec 3.3) to form a repulsive speckle potential. Since the diffused laser beam no longer works like a Gaussian beam, the optical setup shown in Fig 3.19 is finalized after trying different lens combinations, so that the speckle beam could match the aperture of the objective. The iris is used to control the effective NA of the speckle

3. Experimental Setup

beam. Characterization of the speckle pattern is made with a camera outside of the system. Refer to the bachelor thesis of Lorenz Fischer [49] for more detail. The speckle grain size used in this experiment is estimated to be $\sim 1 \mu\text{m}$.

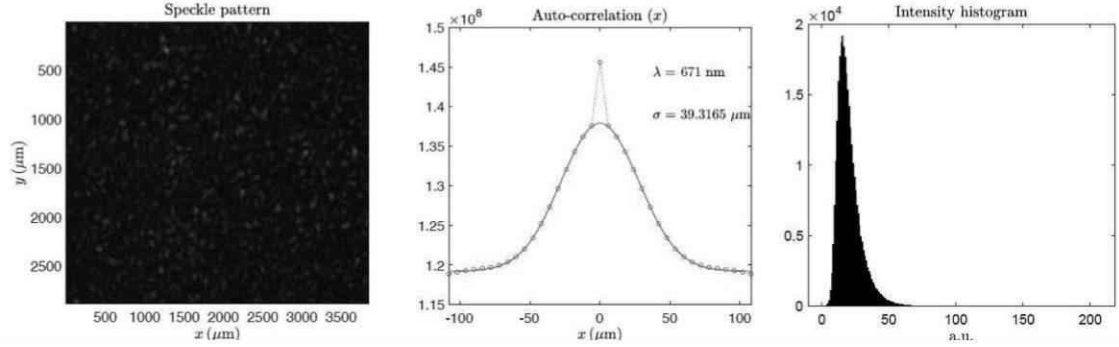
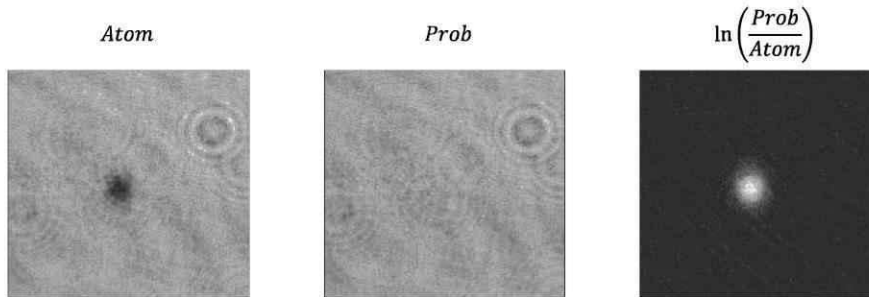


Figure 3.20.: A typical measurement for speckle characterization. Figure adapt from Ref.[49]. (left) Speckle pattern on camera. (middle) Autocorrelation function fitted to Gaussian. (right) Intensity histogram of speckle pattern.

3.4. Imaging

3.4.1. Absorption Imaging

The technique of absorption imaging is widely used in cold atom physics. It allows precise measurement of atomic density without the knowledge of detail characteristic of optical elements and camera, with the drawback of high imaging shot noises, resulting low signal-to-noise ratio for low atomic density.



In a simplified description, absorption imaging measures the shadow of an atomic cloud. For an on-resonance light beam far below saturation intensity passing through

3. Experimental Setup

an atomic cloud, the light intensity afterward would be:

$$I = I_0 \exp(-\tilde{n}\sigma) \quad .$$

Here \tilde{n} is the density integrated along the optical path, and $\sigma = \frac{3\lambda^2}{2\pi}$ is the scattering cross-section with λ being the transition wavelength. By taking two images of laser pulses with and without the atomic sample respectively, which are normally named as 'Atom' image and 'Probe' image, we could calculate the atomic density by simply division the two images:

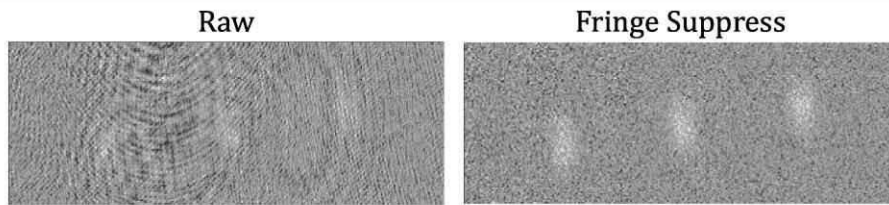
$$\tilde{n} = \frac{1}{\sigma} \ln \left(\frac{I_{Probe}}{I_{Atom}} \right) \quad .$$

This approach can give an accurate measurement as long as the imaging beam is significantly below the saturation intensity. When imaging intensity is closer to or higher than the saturation intensity, it is required to know the measured intensity level (I_{sat}) of the camera when the imaging beam reaches saturation, such that the absorption level could be corrected. Furthermore, in a real experiment, the image taken by the camera may include a signal other than the imaging light, such as scattered light or dark count from the CCD itself. So we would normally take a third background image without the imaging light ('Bgd' image) as a reference for correction. And the calculation of atomic density would amounts to:

$$\tilde{n} = \frac{1}{\sigma} \left[\ln \left(\frac{I_{Probe} - I_{Bgd}}{I_{Atom} - I_{Bgd}} \right) + \frac{I_{Probe} - I_{Atom}}{I_{sat}} \right] \quad .$$

Fringe Removal Algorithm

When applying the absorption imaging technique, the imaging light passes through several optical elements before reaching the CCD sensor. Between each two glass surfaces, there is the possibility of forming an interference pattern, which results in a fringe pattern in the image taken. With more optical elements or higher magnification, the final image will become more sensitive to fringe noise.



Reducing fringe noise with better stabilization is of course preferred. At the same time, it is also possible to suppress the fringe noise through pure mathematical processes

3. Experimental Setup

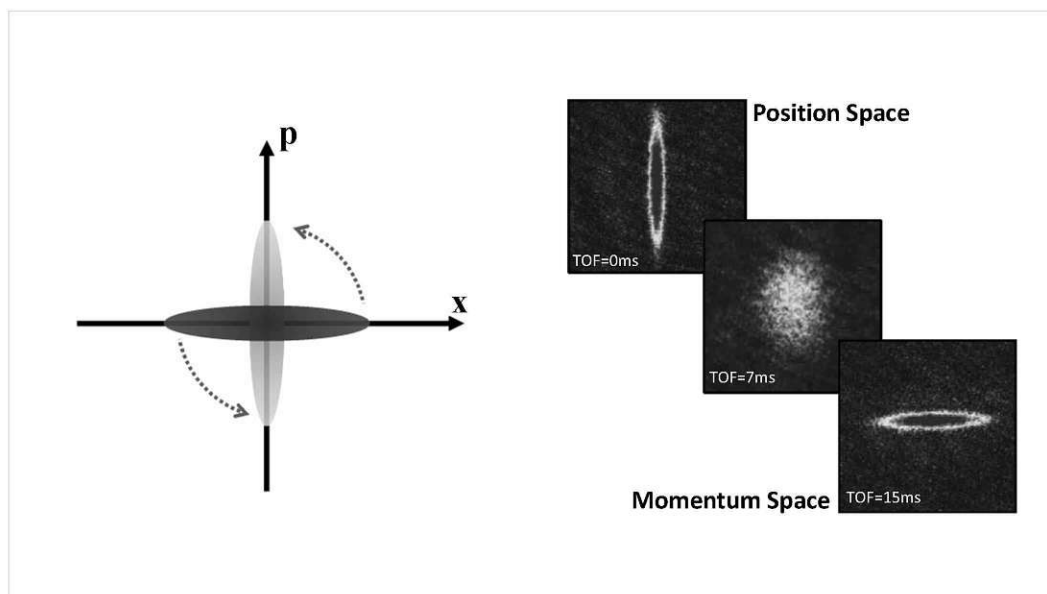
[50, 51]. If the fringe patterns are relatively stable in position and shape, a reference prob image can be created from a database of multiple prob images, such that the fringe noise in the result could be minimized.

In principle, this algorithm works better with a more "complete" database, which means more images. However, it is not guaranteed to be effective because of the random nature of the fringe pattern in an experiment, and it is preferred that the database is composed of images that are taken the closest in time to the target Atom image. Also, if the size of the database increases, the time cost for this algorithm would increase exponentially with respect to the number of images included in the database. In the experiment, when fringe removal is required in real-time analysis, we compose the database with the latest 30 images and renew it every cycle.

Time of Flight and Mater-wave Focusing

When an atom cloud is released from the trap, if we assume there is no external potential, then the cloud will expand with each particle moving at its own velocity. As a result, after a relatively long time, the position of the particle is dominated by its velocity over the in-trap position, so the momentum distribution of the cloud can be measured in a far-field image. This method is known as time-of-flight (TOF) measurement, and it is widely used in cold atom experiments.

In our experiment, the presence of a magnetic field is unavoidable, due to the constrain of Feshbach molecule lifetime. The TOF required for the initial size of the cloud to be negligible is very long. As a result, we intentionally designed our coil configuration to provide a harmonic confining potential horizontally with trapping



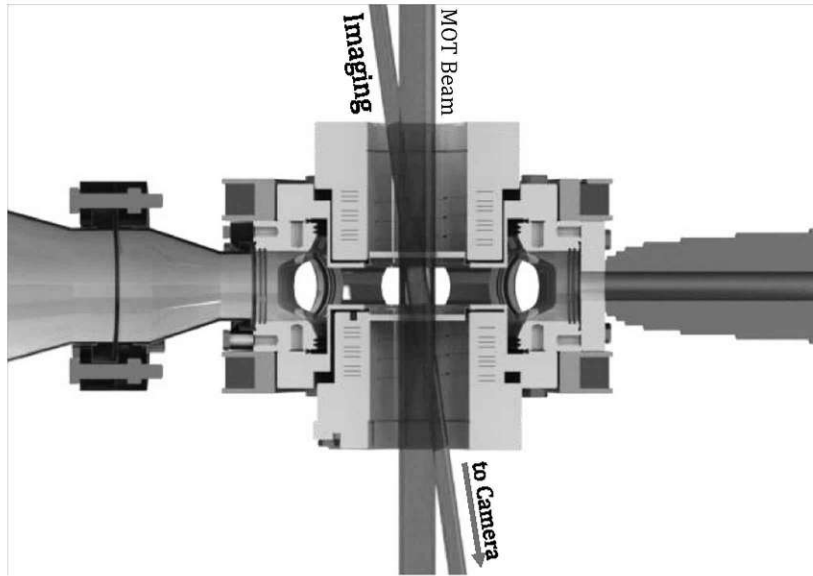
3. Experimental Setup

frequency $\{f_x, f_y, f_z\} = \{16 \text{ Hz}, 16 \text{ Hz}, -23 \text{ Hz}\}$ (around 650 G), allowing for the matter-wave focusing, with which the in-trap momentum distribution can be accessed after a finite TOF. After a quarter period of evolution, the initial density profile will collapse into a point and the evolved profile corresponds to the initial momentum distribution.

The measuring technique we use is called "Focusing" [52]. Instead of a free expansion, the cloud evolves within a harmonic potential. From classical mechanics, a particle with certain momentum will move in an elliptical trajectory within the potential. As a result, the momentum distribution can be observed after quarter period oscillation $T = \frac{1}{4f_{x,y}}$ when released from the dipole trap. This process can also be understood as matter-wave being focused/Fourier transformed by a lens into momentum space, thus the name "Focusing".

3.4.2. MOT Chamber

Since there is no plan for experiments to be conducted in the MOT chamber, the imaging system setup is rather simple, which fits the purpose of examining the collection and preparation of the cloud. We installed a PCO Pixelfly USB camera below the MOT chamber with an angle of 8° , such that the imaging path could avoid the MOT beam path. The imaging lens set consists of two 150 mm achromatic lenses, forming a 1:1 image onto the CCD sensor.



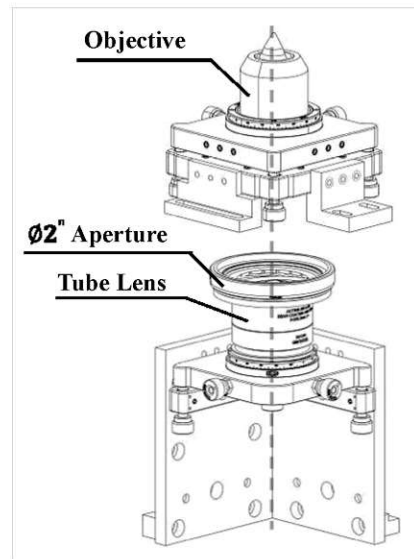
For absorption imaging, we pulse an on-resonance light from above the chamber. This normally requires the presence of a homogeneous magnetic field such that all

atoms will be on resonance. So we also do fluorescence imaging with the MOT and Repump beam at low field, for example during the MOT stage.

While pulsing the MOT and Repump beams, an extra beam shutter needs to be implemented to block the vertical beam path, or the image will see a very strong reflection from the chamber window. In order to switch off the vertical beam with the desired speed, we built a telescope with two 100 mm focusing lenses such that the beam size at the shutter is small enough.

3.4.3. Sci Chamber

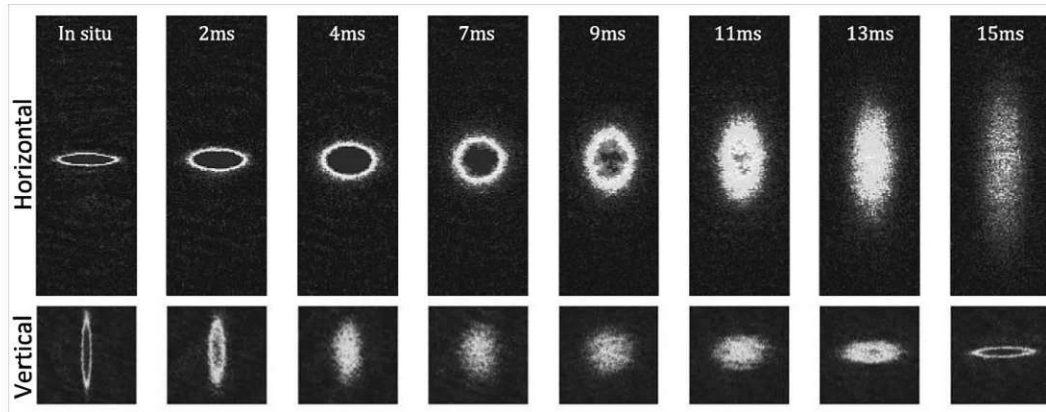
The imaging setup on the Sci chamber side is designed for high-resolution imaging with single-atom sensitivity. Our objective lens is custom-made by SPECIAL OPTICS. It is specially designed to achieve a numerical aperture of 0.5 with effective focus length $f = 27$ mm, while correcting for the 4 mm chamber glass. The objective is mounted below the glass cell on a 6-axis kinematic optic mount from Thorlabs (K6X2), which ensures adjustability for the position and angle. In this thesis, we combine the objective with a 300 mm achromatic lens, which gives a magnification of 10.8. The images are taken by an EMCCD camera of Andor (iXon Ultra 888). In addition to the vertical imaging path, we also installed a horizontal imaging setup for checking and alignment purposes.



Between the objective and tube lens, we have the option to insert a special laser clean-up filter (F94-671L, AHF Analysentechnik). The filter only transmits light with 670-672 nm wavelength and reflects all other wavelengths from 500 nm to 1000 nm. This allows us to combine other dipole light into the imaging path, such as speckle (Sec 3.3.3), DMD, etc without significantly contaminating the camera images.

For absorption imaging, we pulse the on-resonance light from above the chamber. The coherent laser light passing through several glass surfaces inevitably forms multiple interference patterns, thus fringes on the images. The imaging result became sensitive to the relative vibration between different surfaces, and the sensitivity would be amplified by larger magnification.

3. Experimental Setup



To counter the vibration, we first mount the laser out coupler on a dynamically damped pillar (DP10A/M from Thorlabs). This could reduce the effect of vibration from the optical table. Secondly, we stuff the spacing between the glass cell and the objective with "Sorbothane" isolation material. As the objective is designed to be installed 2 mm away from the glass chamber surface, we 3D printed a holder with 1 mm thickness and cut the damping polymer to be 1.6 mm thick (The purpose of the holder is to avoid friction on the cell surface when screwing in the objective). While installing the objective, the polymer is compressed such that it serves as a stabilizer for the glass cell.

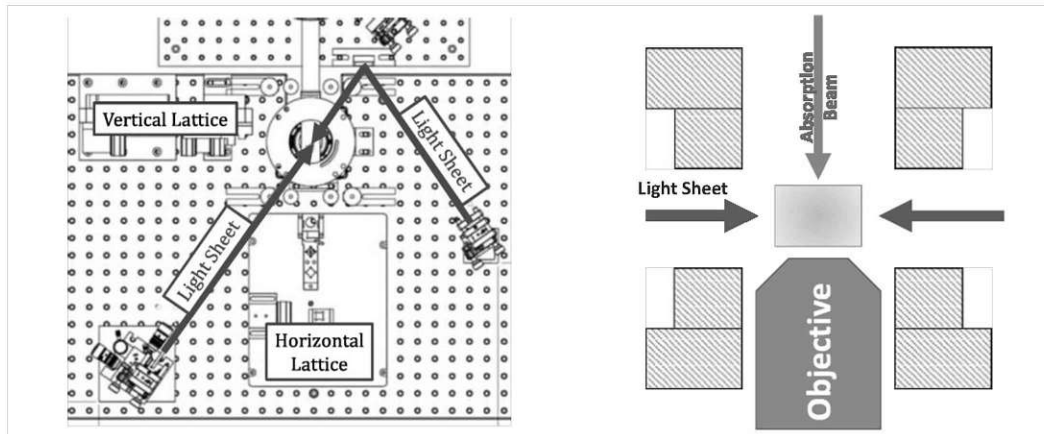


Figure 3.21.: Top (left) and section (right) view of the imaging setup. The two fluorescence imaging beams are sent in at Brewster angle to reduce reflection.

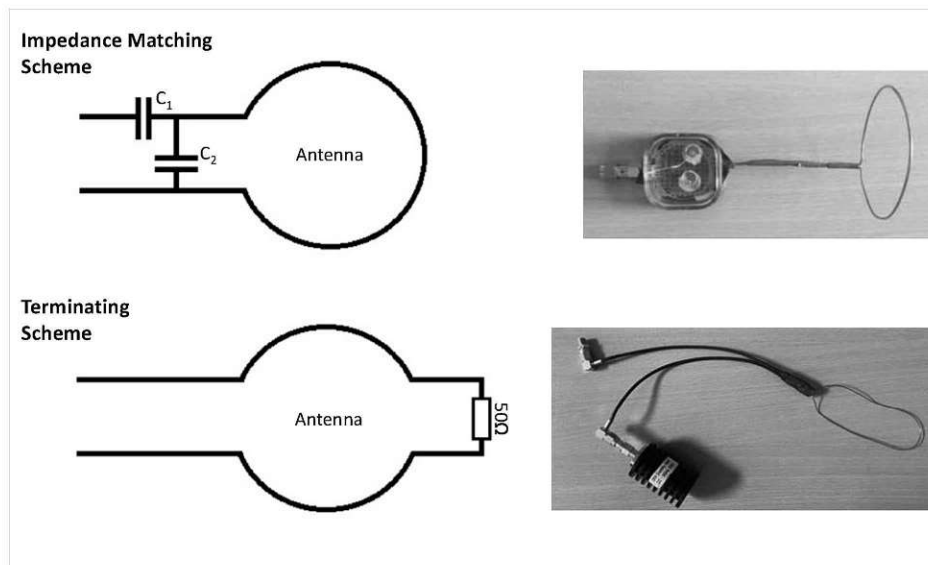
A fluorescence imaging setup was also installed, as part of the plan for future 2D experiments. As shown in Figure 3.21, two counter-propagating beams are focused with cylindrical lenses, forming a light sheet at the atom position. To avoid the formation of an optical lattice, two beams are pulsed alternatingly with 2 MHz frequency. From the

calculation of depth of field, we could get $d = \lambda \sqrt{(n/NA)^2 - 1} \approx 2.3 \mu\text{m}$, $\lambda = 671 \text{ nm}$ is the imaging wavelength, $n = 1$ is the refractive index and NA is the numerical aperture of the imaging setup. This is much smaller than the radial size of 3D atom cloud $\sim 20 \mu\text{m}$, and thus can not be used for the experiment conducted during this thesis.

3.5. State Manipulation

3.5.1. Radio Frequency Transition

We attempted two different designs of radio antennas, frequency selective impedance matching by an L-section bridge with capacitors, and frequency independent (broad-band) impedance matching by a 50Ω termination. The schematics of both designs are shown in the figure below. For convenience, we refer to them as the "impedance matching" scheme, and the "terminating" scheme.



In the impedance matching scheme, we could tune the matching frequency of the antenna over a range of $\sim 20 \text{ MHz}$, which is more than sufficient to cover both the $|1\rangle \leftrightarrow |2\rangle$ and $|2\rangle \leftrightarrow |3\rangle$ transitions. By connecting the antenna to a spectrum analyzer, we can adjust the value of the capacitor while monitoring the reflection level, such that the maximum level of transmission can be achieved in the frequency range we need. As shown in Fig 3.22, each transition can be matched with approximately -10 dB of power reflection with a width of $\sim 2 \text{ MHz}$. For convenience, we implement a Double-

3. Experimental Setup

Pole-Double-Throw (DPDT) switch to toggle between two matching configurations. Details of the antenna design and testing result can be found in the bachelor thesis of Martin Feiler [53].

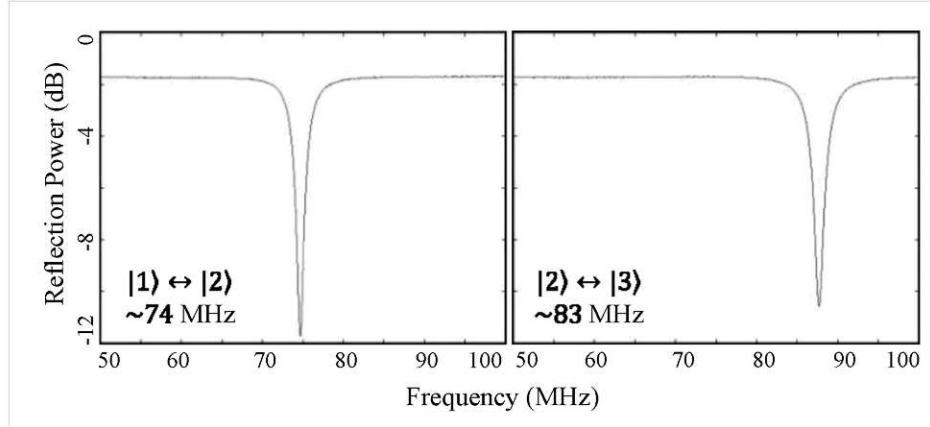


Figure 3.22.: Radio power reflection measured with a spectrum analyzer. Two sets of capacitor are tuned to match the $|1\rangle \leftrightarrow |2\rangle$ and $|2\rangle \leftrightarrow |3\rangle$ transition.

Note that the impedance matching condition is very sensitive to the environment, as touching the capacitor with a metal screwdriver can shift the transmission. Since the metallic chamber and coils have a large influence on the impedance, it is preferred that the antenna is only adjusted after being mounted into the system and fixed in its position.

In the terminating scheme, the antenna is terminated with a $50\ \Omega$ high-power resistor. This design is inspired by Ref [54]. Instead of matching to a narrow frequency band, the antenna is matched to a wide frequency range with lower transmission, and the power that does not convert to radio wave will be absorbed by a power resistor. The terminating scheme could not reach the same level of Rabi frequency given by the matching scheme, but it provides much better protection to other devices during the RF stage. Design and measurements can be found in the bachelor thesis of Bernhard Zeh [55].

We have two sets of antennas installed close to the MOT and Sci chamber respectively, and we chose the terminating scheme for both antennas. Although the matching scheme could reach a higher Rabi frequency, the interference with other devices during the RF stage (e.g. $|1\rangle \leftrightarrow |2\rangle$ mixing for 600 ms) is too strong. In most cases, when using the impedance-matched antenna, the RF power has to be tuned down such that other devices would not be triggered randomly, especially for home-built and OEM devices, resulting in a lower Rabi frequency and instability of the experiment. In the end, the highest Rabi frequency we could achieve is ~ 1 kHz in the MOT chamber and ~ 10 kHz in the Sci chamber.

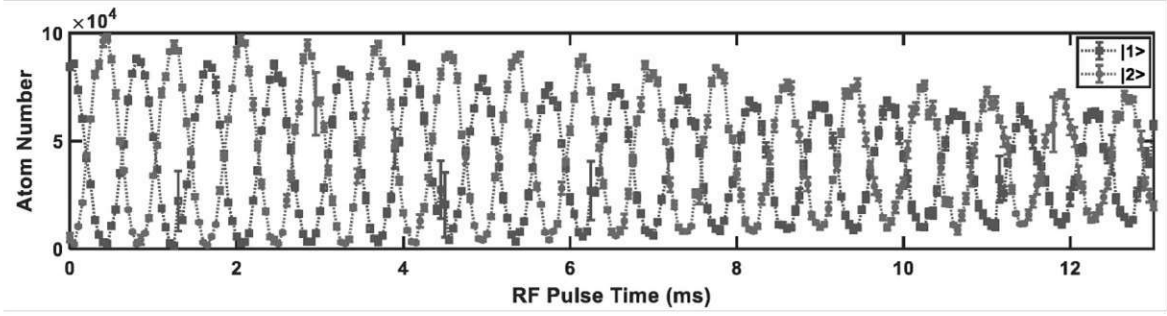


Figure 3.23.: Rabi oscillation measurement of $|1\rangle \leftrightarrow |2\rangle$ started with only $|1\rangle$ population.

Landau-Zener Transition

By doing an on-resonance π -pulse, we could transfer one spin state to another the fastest. However, the RF transition is narrow in linewidth, posing a rather strict requirement on the precision of the magnetic field. In some cases, the inhomogeneity of the magnetic field across a large cloud could already degrade the fidelity of an on-resonance pulse. So instead of applying a π -pulse for state transfer, we use the technique of Landau-Zener sweep [56] to perform a spin flip in the experiment.

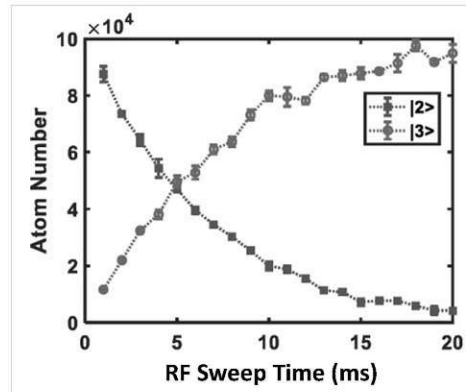


Figure 3.24.: Landau-Zener sweep of $|2\rangle \rightarrow |3\rangle$ started with $|1\rangle$ removed.

RF Spectroscopy

Besides state manipulation, RF transition is also useful as a detection method in some scenarios, such as precision measurement of scattering length [57]. As an example, the RF transition could be used to distinguish atomic and molecular clouds, as the additional binding energy of the Feshbach molecule needs to be compensated by RF during a bound-free transition. In Figure 3.25 is the spectroscopy measurement during the evaporative cooling process.

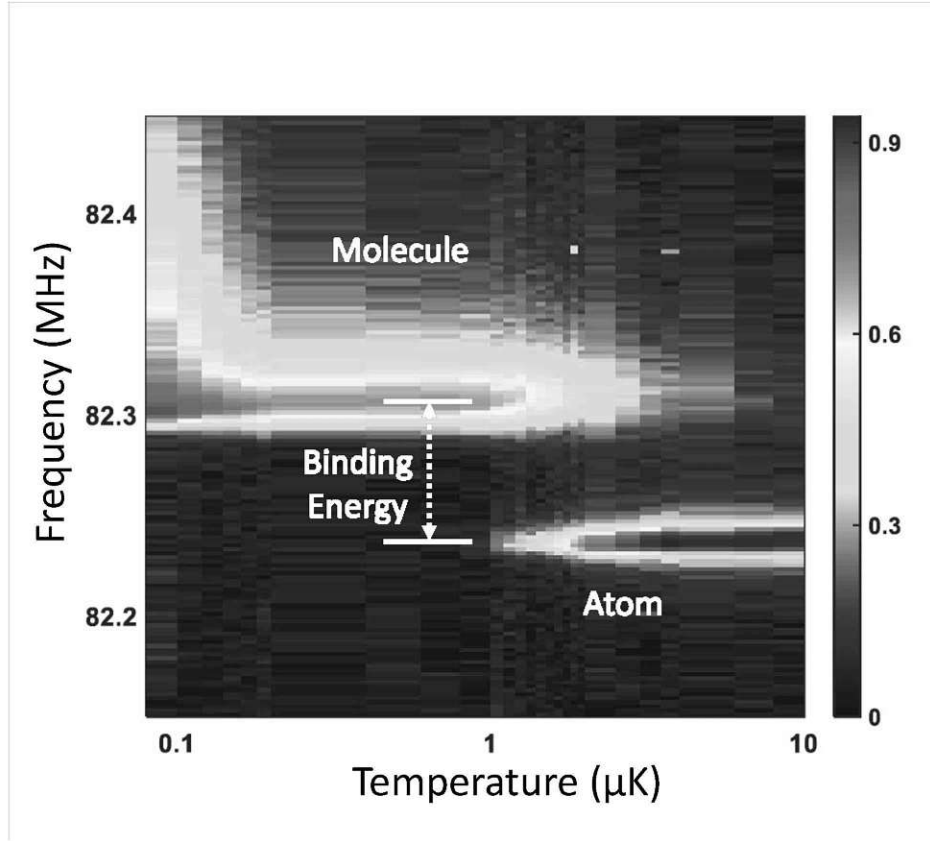


Figure 3.25.: RF spectroscopy of evaporative cooled state $|1\rangle|2\rangle$ mixture, using the $|2\rangle \rightarrow |3\rangle$ transition.

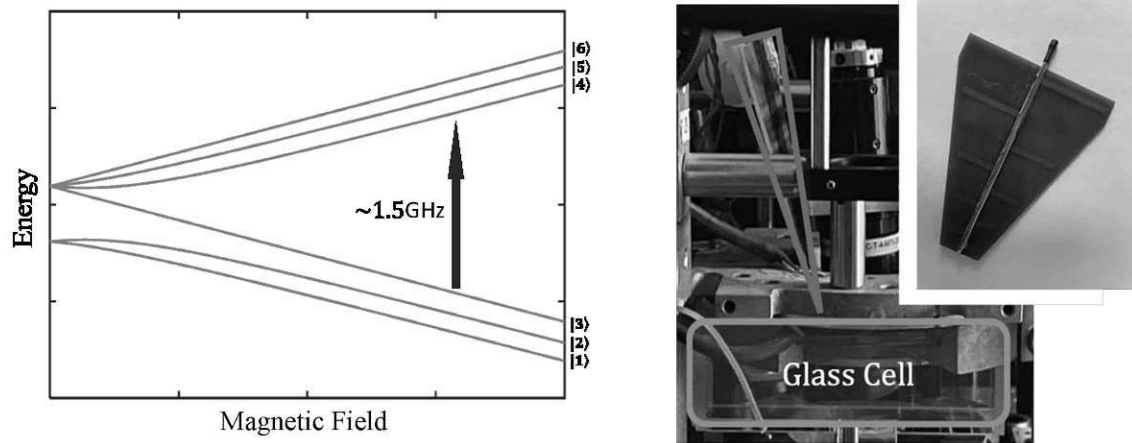
As shown in Figure 3.25, two distinctive peaks can be observed at frequencies 82.3 MHz and 82.24 MHz, which correspond to molecular and atomic signals respectively. The energy gap in between $\Delta E = h * 60$ kHz is the binding energy of the molecule. The molecule formation during evaporative cooling starts around the temperature $3 \mu\text{K}$, which can be compared to the binding energy.

3.5.2. Microwave Transition

Microwave is not commonly used in lithium experiments, as the most used states ($|1\rangle, |2\rangle$ and $|3\rangle$) are separated in the RF range. In this experiment, we attempted to quench the inter-particle interaction by utilizing the $|3\rangle \rightarrow |4\rangle$ transition. Although failed for our attempt, we believe the result is worth presenting.

The idea originated from the desire to reduce the interaction effect during TOF (3.4.1). Although the atom cloud would rapidly expand vertically, we can not quantitatively

3. Experimental Setup



estimate how much the momentum measurement is affected after focusing in the presence of strong interaction. The obvious solution would be to transfer the system right before releasing from the dipole trap into a non-interacting state, namely the $|1\rangle|4\rangle$ mixture. From Marvin Holten's unpublished work in Jochim's Group, we acquire the knowledge that $|1\rangle|4\rangle$ do not possess a Feshbach resonance in our magnetic field range (600 G to 700 G), and the scattering length $a_{14} < 100a_0$, which is much smaller than $a_{13} \approx 800a_0 \sim 4000a_0$.

We implemented a microwave antenna into the experiment as a replacement for the RF setup. By performing a microwave pulse, we are able to locate the $|3\rangle \rightarrow |4\rangle$ transition under different fields (Fig 3.26). Since the transition is one way for bound molecules, we could transfer all atoms from $|3\rangle$ to $|4\rangle$ by an on-resonance pulse for 0.5 ms.

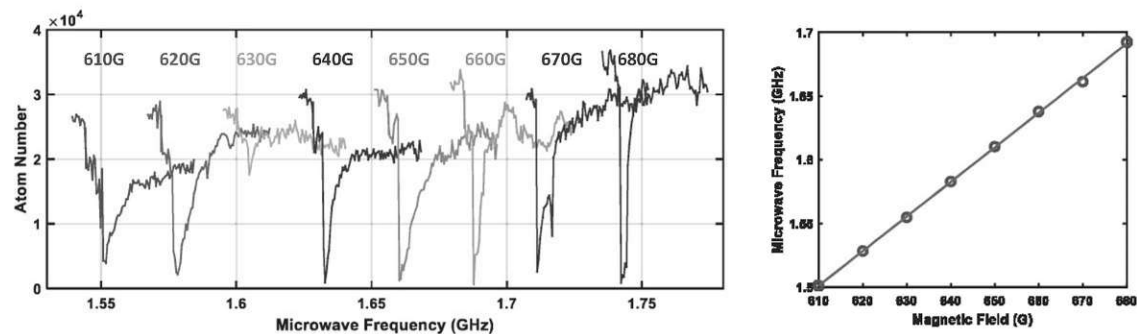


Figure 3.26.: (left) Microwave transition ($|3\rangle \rightarrow |4\rangle$) frequency measurement for different magnetic fields. 630 G has a low signal for unclear reasons. (right) Resonance frequencies with linear fitting. Theory predicts a slope of 2.8 MHz/G.

3. Experimental Setup

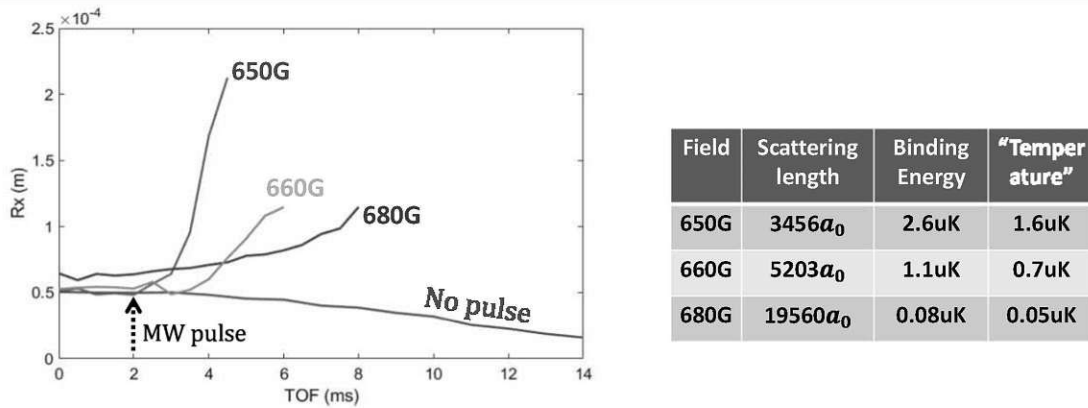


Figure 3.27.: The transverse size of the atom cloud after microwave pulse under different magnetic fields. The difference in initial size is caused by the different repulsive interactions. When no pulse is given, the cloud size would reduce because of focusing (Sec. 3.4.1)

We examined our method by performing TOF measurement with state $|1\rangle|3\rangle$ molecular BEC at various magnetic fields, while pulsing the microwave right after releasing the atom cloud. To our surprise, instead of "compressing" the cloud as the result of reducing repulsive interaction, the cloud starts to rapidly expand after the pulse (Fig 3.27). This could be explained by the breaking of molecules. For a Feshbach molecule, each atom of the pair is bounded in space with uncertainty relative to the size of the molecule, which is also proportional to the scattering length between the two atoms. During a $|3\rangle \rightarrow |4\rangle$ transition, the molecular bounded is broken and the atomic cloud start to expand following its momentum distribution, which is inversely proportional to the uncertainty of position. As a result, smaller scattering length leads to faster expansion. Furthermore, if we treat the expansion to be thermal and calculate the temperature from size vs TOF, we can see that the calculated "temperature" is in the same order as the value of the molecular binding energy of state $|1\rangle|3\rangle$.

3.6. Producing Bose-Einstein Condensate of Molecule

In this section, the procedure of making a molecular Bose-Einstein Condensate (BEC) will be presented with detailed numbers and characteristics. When the number of atoms/particles is given, it refers to the number in each spin state unless mentioned otherwise.

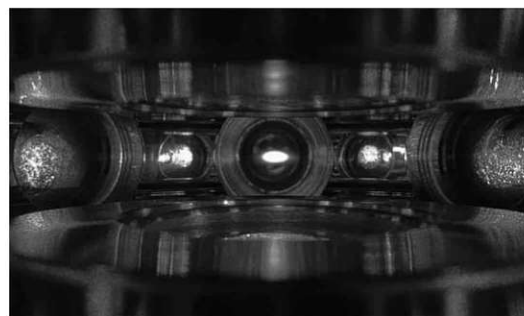
	Thermal	Zeeman Slower	MOT	CMOT	ODT	RF	Evap	Transport	Evap	BEC
T	700K 500m/s	80m/s	1.3mK	337 μ K	422 μ K	246 μ K	9 μ K		6 μ K	20nK
N			5×10^9	2.3×10^8	8×10^6	6×10^6	1.5×10^5	1.2×10^5	8×10^4	1.2×10^4

Hot Atoms

First, the Lithium 6 block in the oven is heated to 380°C, and the lithium vapor enters the Zeeman slower through a differential tube for differential pumping. In the Zeeman slower, a portion of the atom beam will be slowed down to below 100 m/s such that they could be captured by MOT.

MOT

Three laser beams are retro-reflected to form the six-beam configuration. With a field gradient of 10 G/cm and laser detuning of 6σ , we capture an MOT cloud of 5×10^9 atoms with 5 s of loading time. Afterwards, in 700 ms, we shift the position of the MOT cloud towards the dipole trap by ramping the current of Zeeman slower and changing the current balance of the MOT coil pair.



Then we perform a compression on MOT (CMOT) to increase its phase space density for a better dipole trap loading. In 28 ms, the field gradient is ramped to 14 G/cm and the laser detuning to $\sim 1\sigma$. At the same time, the intensities of MOT and Repump laser light are ramped down to 1% of power. The Repump laser is turned off 1 ms earlier than the MOT laser, such that atoms will be pumped to the lower hyperfine state. This step is called "optical pumping".

Optical Dipole Trap and Evaporative Cooling

3 ms before finishing the compression, we switch on the optical dipole trap (ODT) with 150 W of power forming a trap of ~ 1 mK trap depth, and 8×10^5 atoms could be loaded into the dipole trap. At the same time, the MOT coils are switched off and the Feshbach coils are ramped to 780 G. Then we ramp down the laser power to 20 W for evaporation.

Radio Frequency Mixing

To achieve evaporative cooling with high efficiency, a balanced two-state mixture is preferred. Although the optical pumping stage makes sure all atoms sit in state $|1\rangle$ or $|2\rangle$. However, the ratio between the two states is not controlled by the pumping stage, and it has remained a mystery how to achieve a balanced spin mixture without extra steps. So in our experiment, we always perform a radio frequency mixing (Sec 3.5.1) regardless of the ratio. For 600 ms, the magnetic field is fixed and the RF frequency is ramped across the transition multiple times (or fix the RF frequency and ramp the field), and the cloud will end up with equal numbers in state $|1\rangle$ and $|2\rangle$.

$|1\rangle |3\rangle$ mixture

After mixing, we give a $|2\rangle \rightarrow |3\rangle$ Landau-Zener pulse (Sec 3.5.1) to transfer the $|1\rangle |2\rangle$ mixture to $|1\rangle |3\rangle$ mixture. However, during the state transfer, a mixture of all three states $|1\rangle |2\rangle |3\rangle$ is bound to appear, and this process will have a high loss rate from three-body collision. As shown in Figure 3.28, if we actively clean away $|1\rangle$, the transfer efficiency could be doubled. To reduce the loss, we choose to perform the transition at $B = 568$ G where $a_{12} = 171a_0$, $a_{23} = 0$ and $a_{13} = -109a_0$. The loss is minimized and the transition of $|2\rangle \rightarrow |3\rangle$ can be achieved with efficiency higher than 90%.

There are two major advantages of using $|1\rangle |3\rangle$ mixture in our experiment. Firstly, since there will be no magnetic field during the optical transport stage, no molecule could survive the transport. While the tunable lens has a maximum power tolerance, it sets an upper bound to the cloud temperature for transport. For the $|1\rangle |2\rangle$ mixture, evaporative cooling needs to be performed near the Feshbach resonance (780 G), so molecule formation may already occur before the transport, and result in extra loss of atom. $|1\rangle |3\rangle$ mixture, however, could be efficiently cooled at 300 G where no Feshbach molecule could be formed. Second, the imaging transition of $|1\rangle$ and $|2\rangle$ are less effective, whereas $|3\rangle$ is a closed transition. So imaging of $|3\rangle$ would give a better signal compared to others.

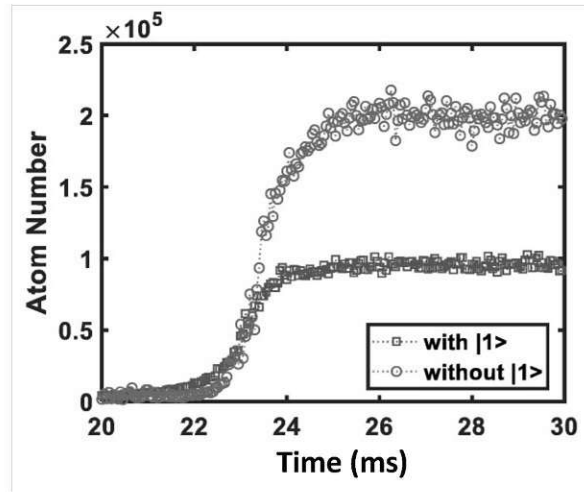


Figure 3.28.: $|3\rangle$ number measure of $|2\rangle \rightarrow |3\rangle$ Landau-Zener sweep perform at 620G.

Optical Transport

With more than 90% of $|2\rangle$ transferred to $|3\rangle$, evaporative cooling continues at 300 G (or 780 G for $|1\rangle |2\rangle$). We normally evaporate to a cloud of $N = 1.5 \times 10^5$ at temperature $8 \mu\text{K}$ before transport (limited by tunable lens Sec. 3.3.1). The atom cloud is transferred into the transport beam by rotating a waveplate (Sec 3.3.1), then the Feshbach field is switched off and the atom cloud is pushed to the Sci cell by shifting the focus of the transport beam.

Cooling to BEC

After reaching the Sci cell, the transport beam is ramped down and the atom cloud is transferred to the capture trap. The Feshbach field is ramp to 760 G ($|1\rangle |2\rangle$) or 670 G ($|1\rangle |3\rangle$). Evaporative cooling is continued until a pure BEC is obtained.



One other option is to cool on the BCS side of the Feshbach resonance, where a degenerate Fermi gas (DFG) can be produced (Figure 3.29).

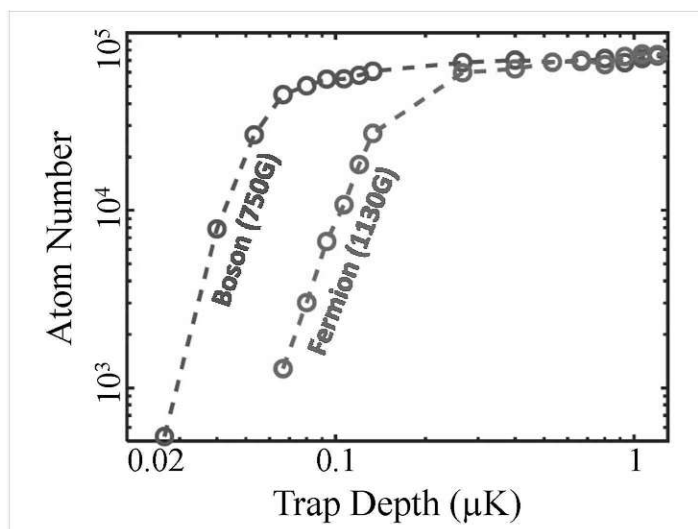


Figure 3.29.: Evaporative cooling performed on the bosonic and fermionic sides of the Feshbach resonance.

4. Scattering from Optical Lattice

In 1933 Kaptiza and Dirac made the prediction on the behavior of matter-wave diffracting from standing waves of light [58]. They presented the process of two-photon scattering where particles within the standing wave gain discrete momenta in units of the vector sum of the two photons' recoil. This phenomenon was first experimentally observed by David E. Pritchard with thermal atom beams¹ [60]. Later, the same effect was also observed with electron beams [61, 62] and BEC [63–66].

4.1. Diffraction from Lattice

In this chapter, I will present the experimental studies of the diffraction process in the presence of strong inter-particle interaction. The same result is published in Ref.[67], with Figures 4.1, 4.3 and 4.10 to 4.14 adapted from the publish paper. The effect of interaction during the diffraction process was mostly neglected for mathematical simplicity, since the diffraction time is mostly considered to be short and particles are stationary. But such simplification may no longer hold for strongly interacting systems or longer timescales [68–70], as shown by our experimental observation of the experiment together with theoretical simulation.

The experiments are performed with mBECs of ~ 3000 ^6Li Feshbach molecules in a two-state mixture of the lowest two hyperfine states $|F = \frac{1}{2}, m_F = \frac{1}{2}\rangle$ (state $|1\rangle$) and $|F = \frac{1}{2}, m_F = -\frac{1}{2}\rangle$ (state $|2\rangle$). By controlling the external magnetic field, we tune the s -wave scattering length between molecules and study the scattering process under different interactions. For weakly bound molecules close to the Feshbach resonance, the dimer-dimer s -wave scattering length is given by $a_{dd} = 0.6a_{12}$ [22], where a_{12} is the scattering length between atoms in states $|1\rangle$ and $|2\rangle$. In this chapter, all scattering lengths are given with the dimer-dimer (a_{dd}) value.

Figure 4.1 shows a qualitative sketch of the setup. The mBEC is confined in a combined trapping potential formed by a focused dipole laser beam (1064 nm) and

¹Fun fact: Initially, the effect predicted by Kaptiza and Dirac was actually Bragg scattering [59]. However, the first group of experiments claimed the observation of K-D effect, which many years later was found to be mistaken. But the convention has stayed.

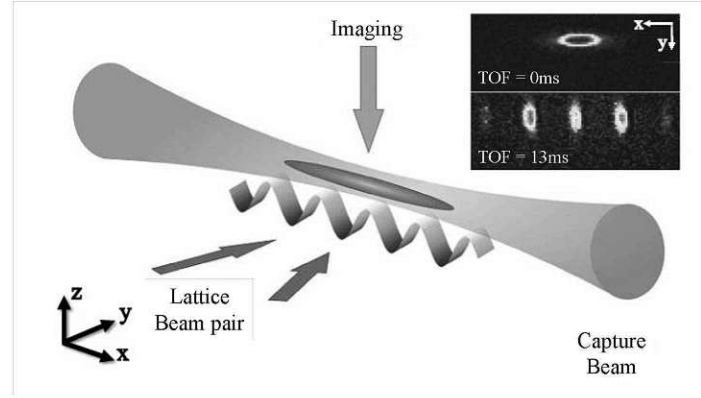


Figure 4.1.: Schematic of the experimental setup with images taken in situ and after focusing.

the magnetic field curvature produced by the Feshbach coils. The combined potential provides trap frequencies $(f_x, f_y, f_z) = (16, 74, 68)$ Hz, where x denotes the axial direction along the capture beam, y the other horizontal direction, and z the vertical direction. The axial trap frequency is varied only by 7%, for magnetic field offset from 650 G to 750 G, so the trap frequencies are only very weakly affected by changing the field level, while the radial directions are dominated by the optical dipole trap.

The lattice potential $U(x) = U_0 \cos^2(\pi x/D)$ is formed by crossing two 1064 nm laser beam with angle 15° , resulting in a lattice period $D = 4 \mu\text{m}$. The lattice laser beams are focused to beam waists of $w_{\text{horizontal}} = 600 \mu\text{m}$ and $w_{\text{vertical}} = 140 \mu\text{m}$, such that they are large compared to the size of the mBEC, and hence the lattice potential depth is approximately uniform across the cloud. The recoil energy of the two photon transition is $2E_r = 2\hbar^2 k_l^2 / 2m \approx 500$ Hz, where $k_l = \pi/D$, m is the mass of a lithium molecule (${}^6\text{Li}_2$) and E_r is the recoil energy of the corresponding single photon transition.

4.1.1. Raman-Nath regime: Kapitza-Dirac Scattering

When the pulse time is short enough such that the particles in the potential could be seen as stationary, or equivalently $t\sqrt{E_r U_0}/\hbar < 1$, the scattering process occurs within the Raman-Nath limit [71] or thin grating limit, and the process is normally referred to as Kapitza-Dirac scattering. The lattice potential results in a periodic phase imprinting on the BEC wavefunction, which in the far field translates into an interference pattern that corresponds to momentum distribution with a fringe spacing of $2\hbar k_l$. The occupation of each momentum mode is given by the Bessel function of the first kind:

$$P_{\pm n} = J_n^2\left(\frac{tU_0}{2\hbar}\right). \quad (4.1)$$

We pulse the lattice with $t = 0 \sim 20 \mu\text{s}$ at a trap depth of $U_0 = 500E_r$. To investigate the effect of inter-particle interaction during the scattering process, we perform the same pulse under magnetic field $B = 650 \text{ G}$, 700 G and 750 G , which correspond to scattering lengths of $a_{dd} = 486a_0$, $982a_0$ and $2109a_0$. The momentum distribution evolutions are observed and shown in Figure 4.2.

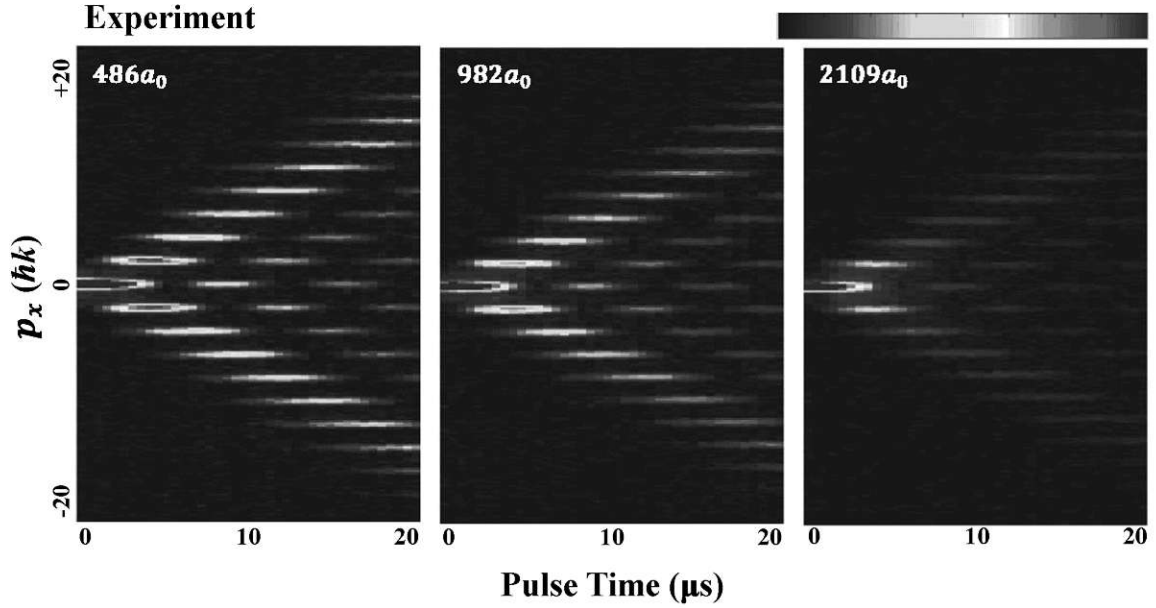


Figure 4.2.: Time carpet of momentum evolution of Kapitza-Dirac scattering measured at different scattering lengths.

The evolution of $\pm 2n\hbar k_l$ momentum modes can be clearly observed. With increasing scattering length, we see a degradation of coherent modes peak signal and a growth of background level, which suggests an interaction-dependent loss of molecules from the condensate.

Fitting and Background Remove

In order to characterize the scattering process under high interaction, we separate the coherent peaks and background, by fitting each momentum measurement to a two-part function:

$$\sum_i A_i^c e^{\left(\frac{x-\mu+id_{sep}}{\sigma^c}\right)^2} + \sum_j A_j^g e^{\left(\frac{x-\mu+2jd_{sep}}{\sigma^g}\right)^2} . \quad (4.2)$$

4. Scattering from Optical Lattice

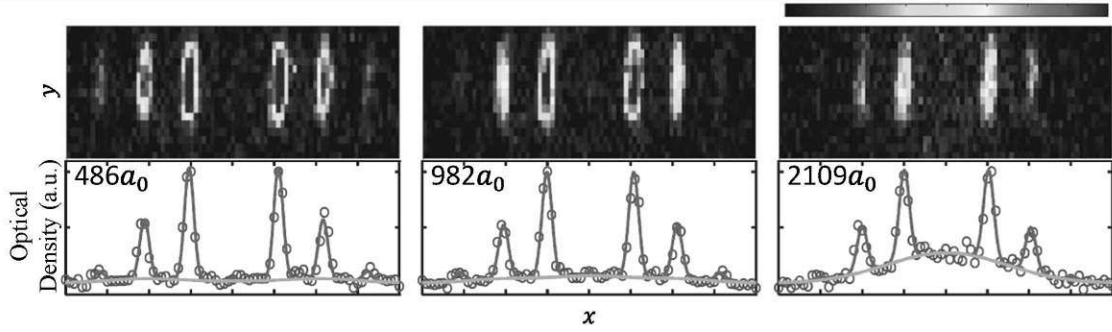


Figure 4.3.: The TOF images (up) with the integrated momentum distribution (down). We fit the lower plots to a two-part function, where the red and yellow represent the condensate peaks and incoherent background respectively.

Here A and σ denote the amplitude and width of the corresponding peak, where the superscript c denotes the molecular condensate and g the incoherent background. d_{sep} is the spatial separation corresponding to the momentum $2\hbar k_l$ which can be accurately determined. Thus we can determine the population of condensate peaks and thermal atoms separately. As shown in Figure 4.3, we integrate the momentum profiles along

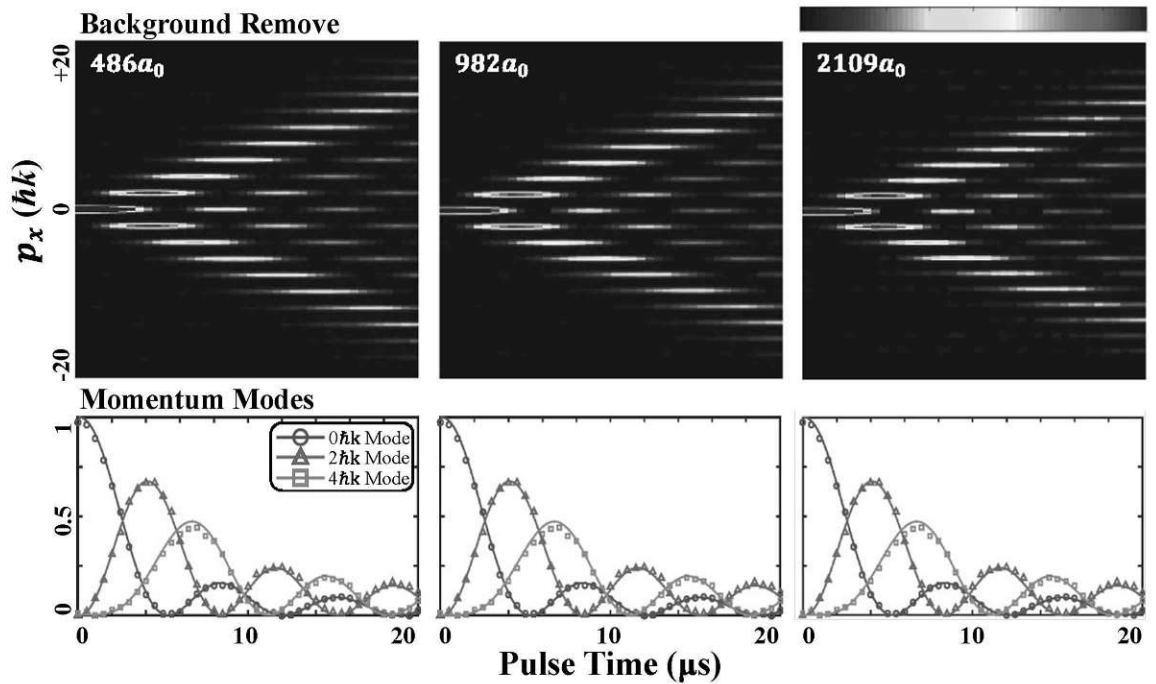


Figure 4.4.: (up) Momentum evolution of different interactions after background removal. (Down) Populations of the lowest three momentum modes plotted with Bessel function prediction.

the y direction and fit the x -momentum profile to the two-part function. The red and yellow solid lines show the fits to respective parts of the two populations obtained by fitting.

Having identified the coherent and the incoherent components, we remove the background population from the momentum distribution and normalize the atom number based on the remaining condensate number. The processed carpets are shown in Figure 4.4 with the Bessel function calculation for the lowest three momentum modes. It can be seen that the processed data shows very good agreement with the Bessel function prediction, which suggests the effect of inter-particle interaction is neglectable during the scattering process, and this agrees with the Raman-Nath approximation under short pulse time. The loss of condensate originated from the interaction effect during other processes, which we will discuss in the later section (Sec 4.1.4).

4.1.2. Beyond Raman-Nath: Channeling regime

To reveal the effect of interaction more clearly, we extend the pulse length and move beyond the Raman-Nath regime. In this case, the particles will oscillate within each lattice site while also tunneling along the lattice direction, creating a periodic pattern in momentum space. If the lattice depth satisfies the condition $U_0 \gg E_r$, the situation is referred to as the channeling regime. An analytical solution is obtained for the weak-pulse limit [72], but in general the population evolution during the scattering process needs to be calculated numerically.

We pulse the lattice with $t = 0 \sim 1000\mu\text{s}$ at trap depth $U_0 = 50E_r$. Figure 4.5 shows the raw and processed carpets of momentum evolution observed with different scattering lengths. The weaker lattice restricts the particles within the first five momentum modes to achieve a decent imaging contrast and drives the evolution at a rate such that the effect of interaction, which becomes apparent at longer times, is clearly measurable. Similar to the Raman-Nath regime, loss is found from the condensed peaks into the background, which becomes more prominent for increased interaction strength. It can be seen that for $a_{dd} > 2500a_0$, the scattering pattern becomes barely recognizable from the image. We apply the same background removal procedure to extract the momentum evolution. However, the high interaction causes excessive loss on different momentum modes, such that the signal to noise level is too low for an accurate determination of population ratios between each momentum peak.

Comparing the population evolution curves of increasing interaction strengths, it can be seen that the time point where the coherent population is restored to the $0\hbar k_i$ mode (recurrence of the mBEC) occurs at increasingly later time points, showing that the evolution becomes slower in the presence of stronger interaction.

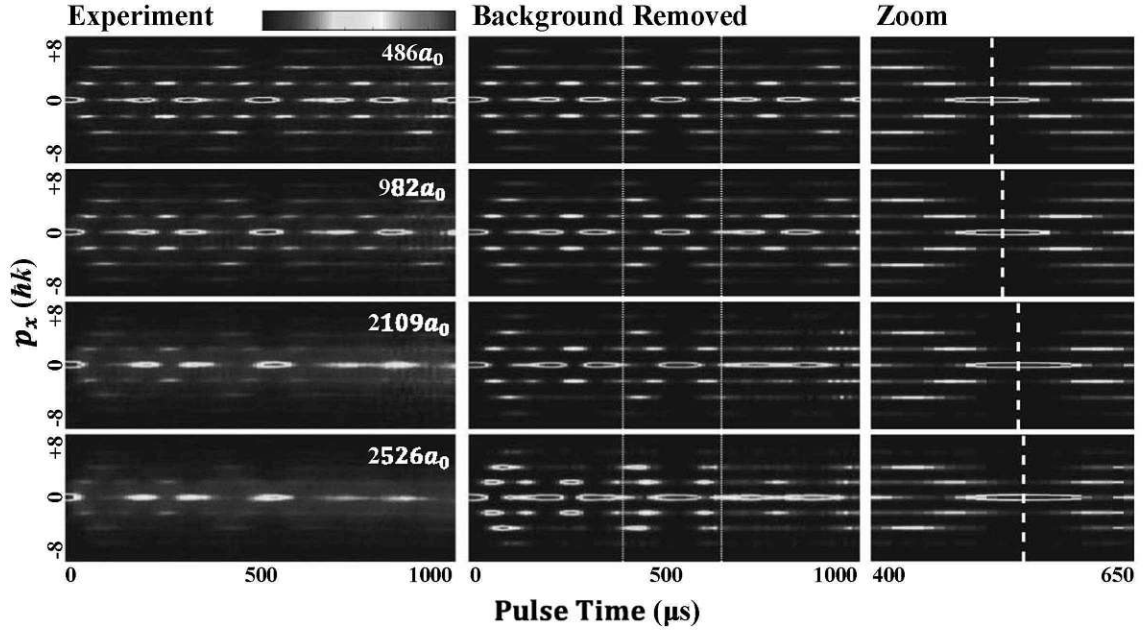


Figure 4.5.: (left) Time carpets measured with $U_0 = 50E_r$ for different interaction strengths. (middle) The momentum modes with background removed and normalized to the total condensate number at each time. The vertical dash lines mark the zoom-in range. (right) The zoom-in view of the recurrence point. The vertical dash lines mark the recurrence.

We also attempt to reproduce this scattering process with 1D GPE simulation. As shown in Figure 4.6, with a scaling factor $\eta = 4.2$ (Sec 4.1.3), the simulation result shows good agreement with experiment observation at lower scattering lengths. At higher scattering, although there is deviation caused by the collisional loss, the overall features of the observed evolution and numerical simulation still match qualitatively.

So far, we have observed two different effects originating from inter-particle interaction, which are the loss of condensate peaks and the slowing down of the scattering process. These effects are presented in further detail in Sec 4.1.3 and Sec 4.1.4.

4.1.3. Interaction Induced Slowing

To assist in understanding the effect of interaction on population evolution, we performed one-dimensional Gross-Pitaevskii equation (GPE) simulations:

$$i\hbar \frac{\partial}{\partial t} \Phi(x, t) = \left[-\frac{\hbar^2 \partial_x^2}{2m} + V(x, t) + g_{1D} |\Phi(x, t)|^2 \right] \Phi(x, t) \quad (4.3)$$

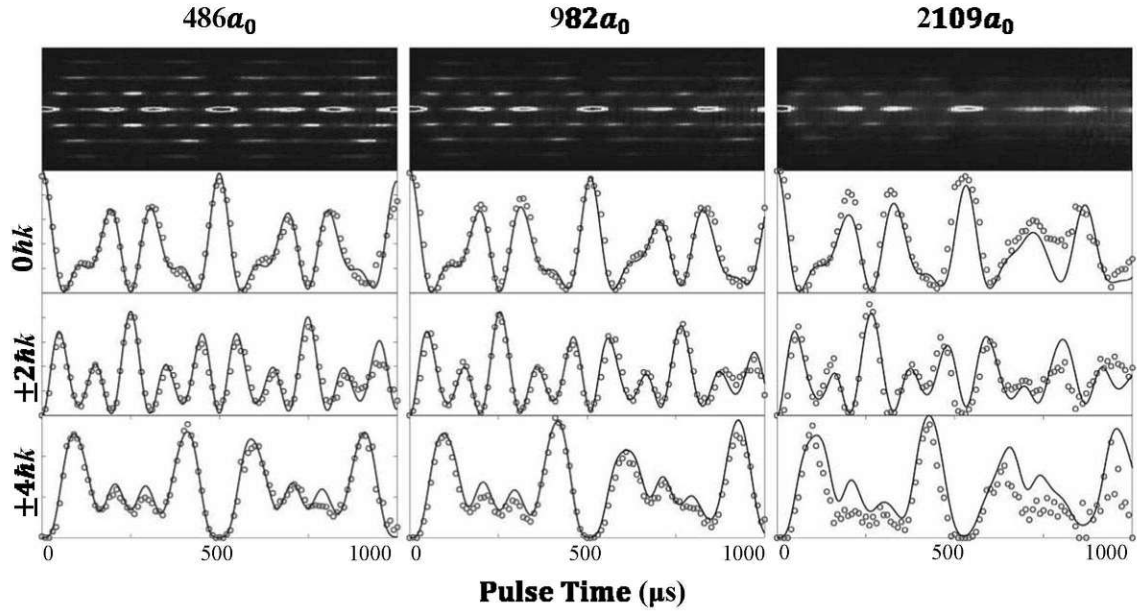


Figure 4.6.: The experimental measurement (red circle) plot with 1D GPE simulation (blue line) with correction factor $\eta = 4.2$ (Sec 4.1.3). All experimental data have been post-processed with background-removing algorithm.

with g_{1D} factor obtained by integrating over the radial direction assuming Thomas-Fermi profiles. The slowing down of the scattering process can be qualitatively understood to be associated with the formation of density grating across the condensate, which arises in the presence of the lattice potential (Figure 4.7).

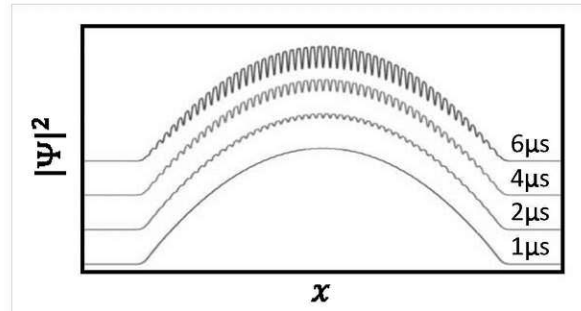


Figure 4.7.: The formation of density grating in the condensate wavefunction during the lattice pulse, calculated from GPE.

The density profiles generated by GPE simulation demonstrating this process are shown in Figure 4.7. Initially, the lattice potential generates a phase modulation in the condensate, which leads to an emerging density grating. The $0\hbar k_l$ mode decreases while

the higher momentum modes grow. For convenient visualization, the simulation here is carried out with a lattice depth of $U_0 = 500E_r$ to obtain a rapid population evolution. An obvious density grating has already formed at approximately $2\mu s$. However, the effect of repulsive interaction, contrary to the optical lattice, tends to smooth out the density grating. As a result, the interaction effectively counters the periodic potential and hence slows down the population evolution during the scattering process.

Since the formation of density grating in the condensate is associated with the emergence and evolution of populations diffracted to higher momentum modes, one can also expect the effect of interaction would reverse the population evolution when the lattice pulse is turned off, and this is demonstrable with the numerical simulation.

Figure 4.8 shows the population evolution of the $0\hbar k_l$ mode population obtained from GPE simulation, with lattice potential $U_0 = 500E_r$ and zero interaction. After $3\mu s$ (left)/ $8\mu s$ (right) of pulse, the lattice is switched off and the interaction is turned on after $2\mu s$. It can be seen that with null interaction, the mode populations maintain the values from the moment the lattice is switched off. On the other hand, when the interaction is switched on, we observe the reversal of the population evolution, consistent with what is predicted based on the physical picture. It is also evident from the comparison that stronger interaction results in a faster reversal of the evolution.

To obtain a quantitative characterization of the slowing effect, we selected the first recurrence of the $0\hbar k_l$ condensate to be our reference for studying the phenomenon. From Figure 4.6 we can see that this feature can be well identified even when there

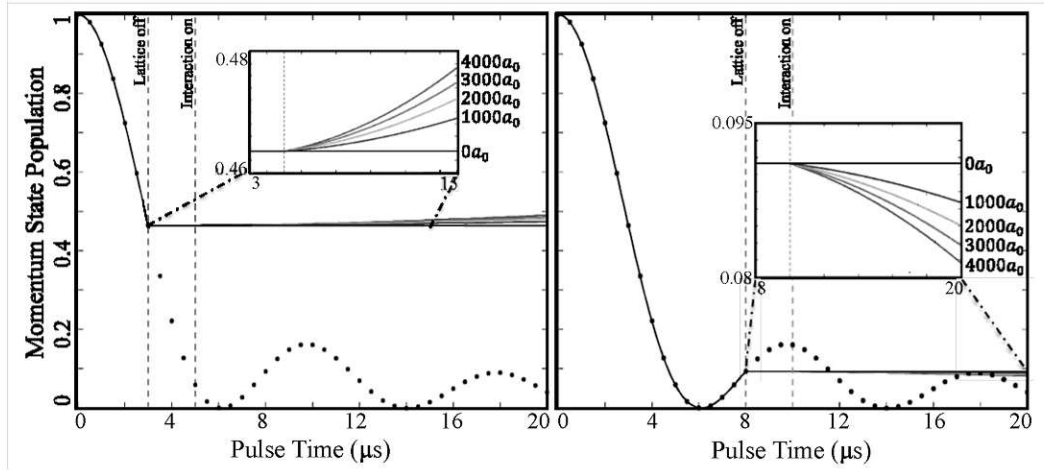


Figure 4.8.: The simulated population evolution of $0\hbar k$ momentum modes with quenching interaction and $U_0 = 500E_r$. Solid lines show the simulation results and dots plot the Bessel function prediction. The two vertical dashed line marks the time of lattice switch-off and interaction switch-on, (left) $t = 3\mu s$ and $t = 5\mu s$, (right) $t = 8\mu s$ and $t = 10\mu s$ respectively.

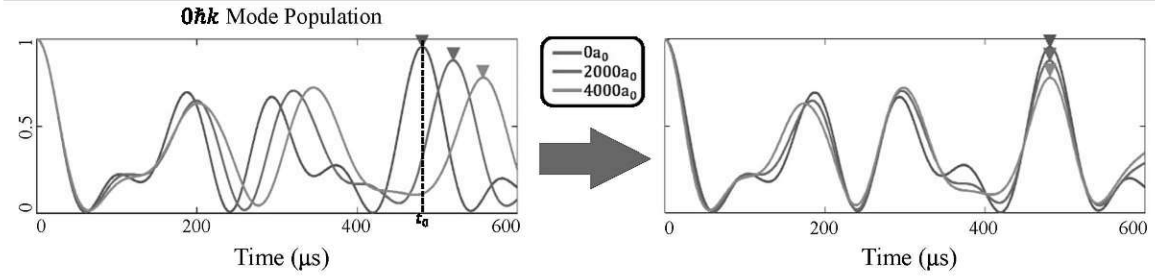


Figure 4.9.: 1D GPE calculation of the zeroth order diffraction peak with different interaction strength. The curves can be aligned by re-scaling in time to match the first condensate recurrence points to the zero interaction case by $t \rightarrow t/(1 + r)$.

is a high level of loss to the background. As shown in Figure 4.9, we generate a set of simulated evolution using 1D GPE with $U_0 = 50E_r$ and various interactions. By applying a peak-identification algorithm, we obtain the recurrence times of the 0th momentum mode for different interactions. Then we define the recurrence time of zero interaction evolution to be t_0 , such that all curves of momentum evolution could be re-scaled by $t \rightarrow t/(1 + r)$, and the slowing phenomenon could be characterized by the parameter r :

$$r(a) = \frac{t(a)}{t_0} - 1$$

where $t(a)$ is the recurrent time for a given scattering length a . This factor $r(a)$ can also be qualitatively seen as an effective reduction of the lattice depth by $1/(1 + r(a))$, such as observed for a quasi-periodic lattice, where the onset of localization is shifted by repulsive interaction to deeper lattice potentials [73].

The same peak-identification algorithm is applied to all experimental and simulated data with $U_0 = 50E_r$ lattice depth, and the result is plotted in Figure 4.10. Although the overall trend could be reproduced by GPE simulation, the actual value of the slowing effect could only be matched with an additional fudge factor to the mean-field interaction term $g = \eta g_{1D}$. We find that for a single value $\eta = 4.2$, the simulation generates results closely fitting the experimental observations not only for the slowing parameter but also for the momentum evolution (Figure 4.6).

This additional interaction energy could partly be accounted for by the dissociation of molecules into atoms during the lattice pulse. When a molecule dissociates into two free atoms, not only will it double the particle number, but the molecule to atom s -wave scattering length is given by $1.2a_{12}$ [74], which is double the value for dimer-dimer scattering. By performing a $|2\rangle \rightarrow |3\rangle$ transition with a radio frequency (RF) pulse (Sec 3.5.1), we could confirm the existence of free atoms after a $60 \mu s$ lattice pulse. Sadly, no quantitative measurement could be made till the present because of

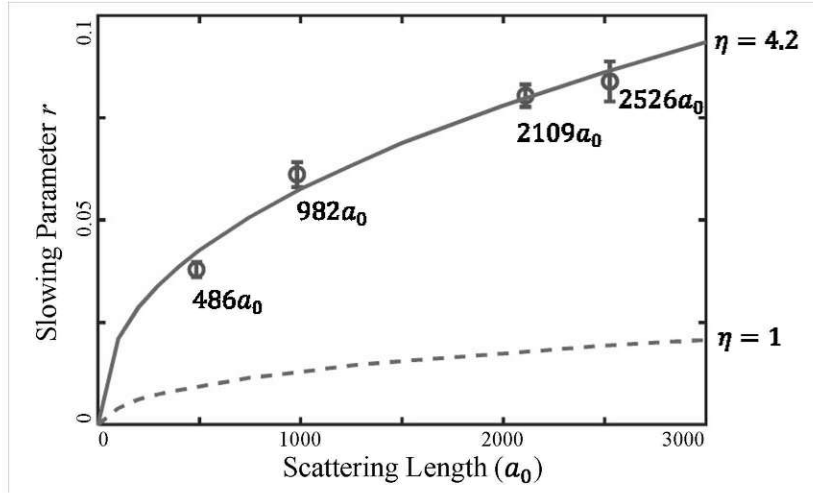


Figure 4.10.: The delay parameter r inferred from experimental measurements versus the scattering length a_{dd} . Error bars are generated with 10 repeated measurements. The solid line and dash line are produced by GPE simulation with $U_0 = 50E_r$ for $\eta = 4.2$ and $\eta = 1$.

experimental constraints (pandemic).

To investigate the origin of this mysterious factor of $\eta = 4.2$, we have built an accordion lattice setup where the lattice spacing can be tuned.

4.1.4. Incoherent Collisions

As stated in Section 4.1.1, we observe the loss from condensate to background increase for stronger interaction strength.

To clarify at which stage and by which processes the loss occurs, we make use of a technique implementing a particular lattice pulse sequence [75], which is designed with particular pulse durations and intervals for a given lattice depth U_0 , aiming at maximizing the overlap between the final wavefunction and the BEC wavefunction in the $0\hbar k$ mode.

Supposing that ψ_0 is the state of a BEC, we calculate the Bloch state after applying a pulse sequence $[t_0, t_1, t_2, t_3, t_4]$ (Figure 4.11),

$$|\psi_{final}\rangle = \prod_{j=4}^0 \hat{U}_j |\psi_0\rangle, \quad (4.4)$$

where $\hat{U}_j = e^{-i[\hat{p}_x^2/(2m) + U_j \cos^2(kx)]t_j/\hbar}$ is the evolution operator in the j th step. The duration of the initial pulse t_0 is fixed at $60 \mu s$ so that it covers the strong loss region

observed. The potential depth U_j is set to U_0 and 0 during the pulses and the time intervals, respectively. U_0 keeps constant for all three pulses.

The time sequence is determined by maximizing $|\langle\psi_0|\psi_{final}\rangle|^2$. For the parameters we choose, $[t_0, t_1, t_2, t_3, t_4] = [60, 78, 26, 36, 36] \mu\text{s}$ and $U_0 = 50E_r$, leading to $|\langle\psi_0|\psi_{final}\rangle|^2 = 0.94$.

On the other hand, after the previous pulse sequence, the populations of the higher momentum modes can be ‘returned’ to the $0\hbar k_l$ mode by applying another designed lattice pulse sequence as long as coherence is maintained.

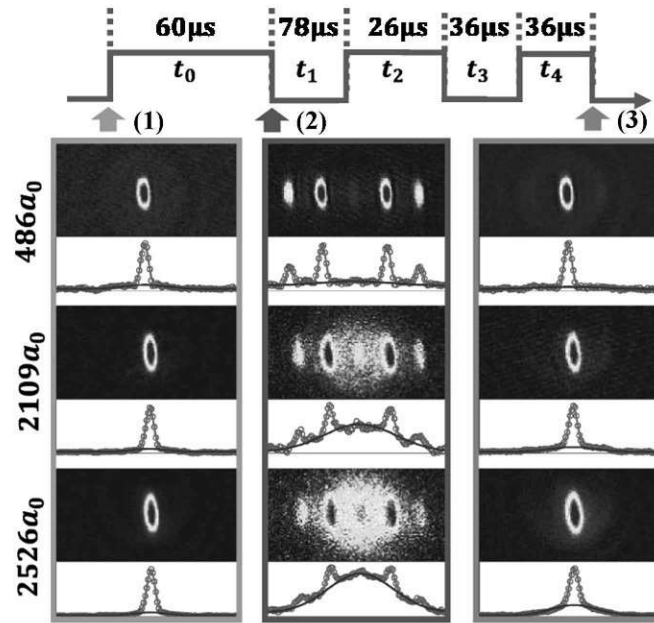
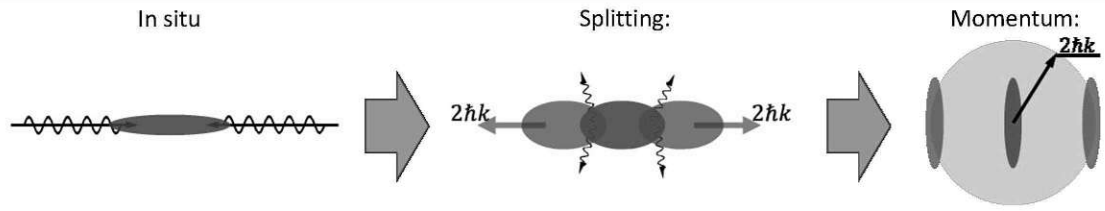


Figure 4.11.: Schematic of the pulse sequence and the corresponding absorption images at different interactions with lattice depth $U_0 = 50E_r$.

As shown in Figure 4.11, we first start with (1) a pure BEC. By applying a lattice pulse with $t_0 = 60 \mu\text{s}$ and $U_0 = 50E_r$, (2) the cloud splits into higher momentum modes $\pm 2\hbar k_l$ and $\pm 4\hbar k_l$. Then we apply the designed pulse sequence and (3) the momentum modes are returned into a BEC. All the images are taken with matter wave focusing technique (Sec 3.4.1) in the momentum space. It is rather obvious that after 3 pulses, the system does not experience a very high loss even at high interaction strength. However, a collisional halo is clearly visible at high interaction, when the cloud is split into different momentum modes. Suggesting the loss to background is mainly due to by the collision during the separation between molecules of different momentum modes.

4. Scattering from Optical Lattice



After pulsing the lattice, the cloud is split into multiple parts with different momenta. During the initial expansion, each momentum mode will move out of the other from the same position. Since the recoil momentum is significantly larger than the superfluid critical velocity [76], collisions between different momentum modes lead to decoherence and redistribution of momenta, which are enhanced under higher interaction. We could clearly observe the result of such collisions from the $2\hbar k_i$ halo in momentum space.

With the additional pulse sequence, the coherent population is returned to the zero momentum mode, and the contribution of collisional loss during mode separation is suppressed. Although the BEC can be mostly restored with the pulse sequence, an interaction-dependent loss can still be observed. We attribute this to in-trap loss which

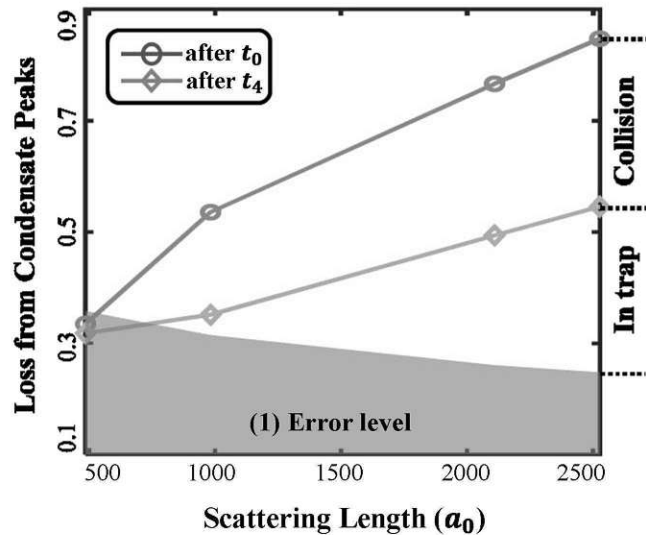


Figure 4.12.: Calculated loss plot against scattering length at different stages. The error level is calculated from the BEC images. The difference between the yellow line and the error level is the loss during the lattice pulse. The difference between the green and yellow lines is the collision loss during TOF.

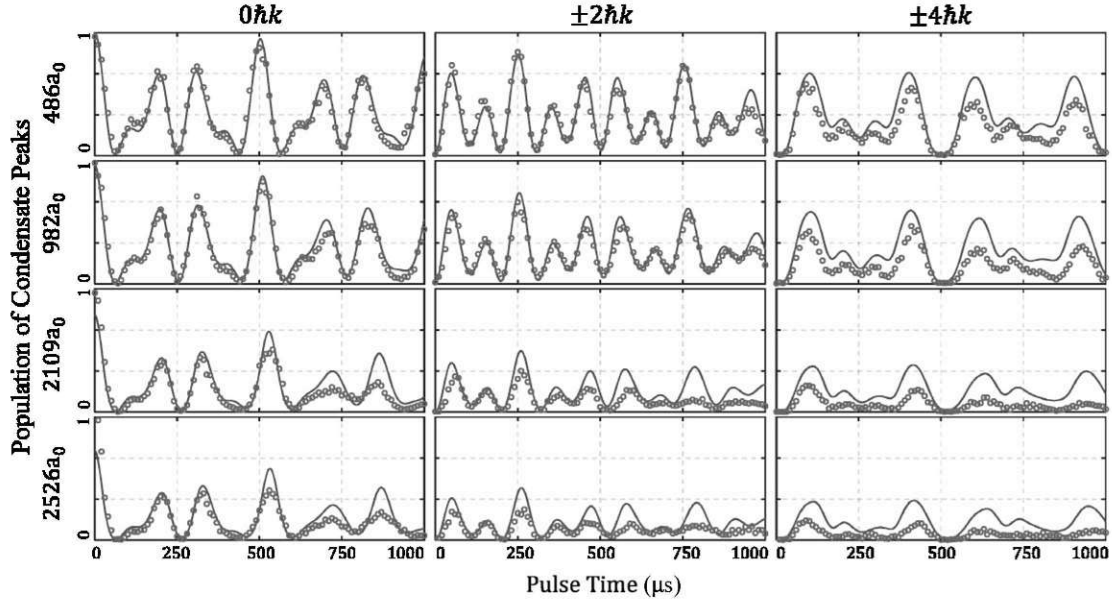


Figure 4.13.: The population evolution at different interaction strengths (red circle) with collision simulation results (blue solid line) for $U_0 = 50E_r$. The initial condition of the simulation is a product of the GPE calculation multiplied by the loss factor.

occurs during the lattice pulse. We identify the contribution of different processes to the loss by fitting the measured profile to Fomular 4.2, and the result is plotted in Figure 4.12. Because the fitting algorithm always includes the background as well as the imaging noise, the "thermal background" fraction is never zero. We correct this by setting an "Error level", calculated from the fitted background fraction for a pure BEC (before lattice pulse).

We estimate the collision loss during separation by calculating the collision events with a simple model. Each momentum mode is simplified to be a uniformly distributed cylinder of particles, with length and radius calculated from Thomas-Fermi approximation for mBEC. The expected collision events encountered by one particle over a distance of travel are given by the number of particles in the other momentum group contained in the cylinder defined by the displacement of the particle and its scattering cross-section.

Due to the symmetry of this setting, the numerical calculation can be done in 1D. In each unit time step, the groups with momentum difference $2\hbar k_l$ shift in relative position by the distance of dx . For two modes that move across each other, the estimated number of collisions is given by:

$$N_{col} = (n_1 \pi R^2 dx) n_2 A dx = n_1 n_2 \pi R^2 A dx^2,$$

where n_i are the (3D) particle density of two overlaying modes, R the Thomas-Fermi radius of the mBEC, $A = 8\pi a_s^2$ the collision cross-section between identical bosons. The line density of the collisional region is $n_i\pi R^2$, and will decrease by N/dx after the calculation step. We take dx to be sufficiently small so that the collision event encountered by each molecule in one calculation step is less than unity. The procedure obtains the expectation value of the number of collision events, and therefore the decrease in particle number from both momentum modes.

We take into account the $0\hbar k_i$, $\pm 2\hbar k_i$, and $\pm 4\hbar k_i$ momentum modes, which have significant occupations during the scattering process. The lost molecules are taken to be immediately removed from the cloud. Secondary or further collisions are supposed to be rare and not taken into account.

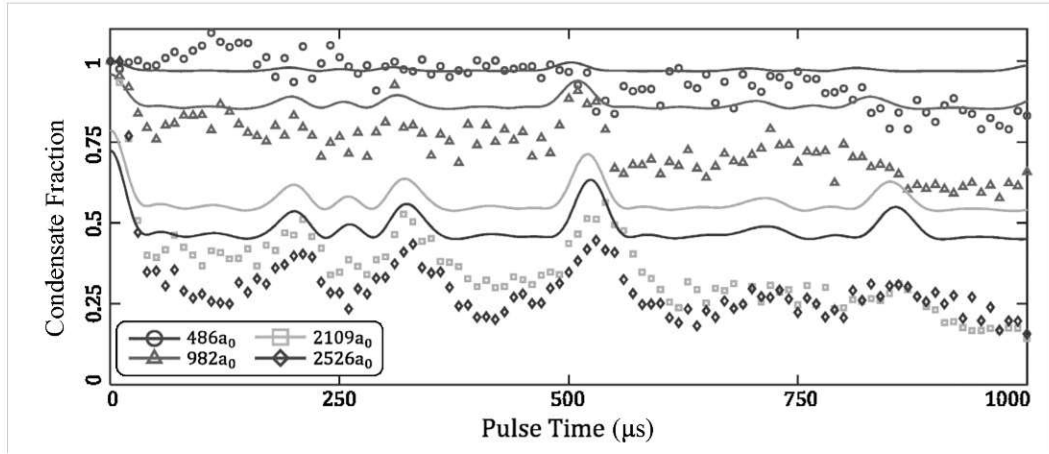


Figure 4.14.: The condensate fraction at different interaction strengths (open symbols) with collision simulation results (solid line) for $U_0 = 50E_r$. The increasing discrepancies between calculated results and experimental data indicate the continuing in-trap loss over time.

The result calculated from GPE with factor $\eta = 4.2$ was taken to be the initial condition for the collision simulation. From the simulation we obtain the estimated total remaining condensed population in the momentum modes (Figure 4.14), as well as the remaining population in the individual modes (Figure 4.13). The results show reasonable agreement with the experimentally observed $0\hbar k_i$ mode for short pulse times, and larger deviation for long pulse time, indicating the increasing contribution from in-trap loss over time. Additionally, the losses from higher modes ($\pm 2\hbar k_i, \pm 4\hbar k_i$) are increasingly underestimated, which we attribute to the approximations taken by the scattering model. In particular secondary collisions or corrections to the scattering cross-section beyond s -wave scattering are not taken into account. Quantifying secondary collisions is difficult given our experimental scenario. Due to the axial length of the condensate in our experiment, the momentum modes mutually separate over the course

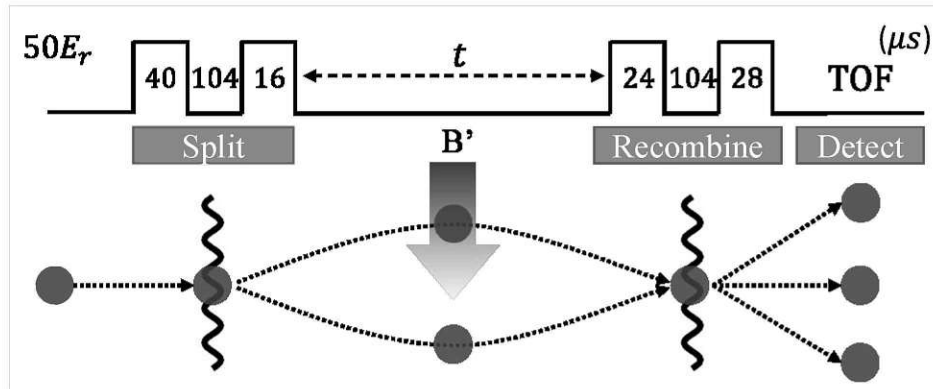
of several milliseconds. If the collisions occur in a small and well-defined range of space and time, one can expect to observe clean *s*-wave collision halos, and deviations from the expected profile would then indicate additional processes such as secondary collisions [77]. This is not the case for our experiment. Our situation is further complicated by the presence of loss caused by the lattice pulse.

4.2. Molecular Interferometer

Interferometry is a basic tool in measurement. By interfering two coherent waves traveling through different paths, the difference imprinted to the waves could be measured with great accuracy. Such technique has been used in many fundamental researches, such as gravimeters [78–80], measuring the gravitational constant [81, 82], and detecting gravitational waves [83–85]. In this section, we investigate the feasibility of ^6Li molecule used as an interferometer, and study the possible effect of interaction. These result are also published in Ref [86].

4.2.1. Michelson Type

The Michelson interferometer, named after the inventor Albert A. Michelson, is well known for its use in the Michelson-Morley experiment. This configuration features splitting a signal source into two arms. After propagating the two arms differently, both arms are combined again to measure the difference in the propagation.



The experiment uses the same setup as Fig.4.1 and starts with a BEC consisting of ~ 6000 molecules. A designed lattice pulse sequence is given to split the cloud into $\pm 2\hbar k_l$ modes. The optical dipole trap naturally acts like a waveguide with two momentum modes traveling within. After a half-period oscillation, two traveling clouds

return to the trap center and are recombined with a second pulse sequence. Detection is done after matter-wave focusing of the cloud, and momentum distribution is observed.

To demonstrate interference, a differential phase shift is introduced between the two momentum modes. When they are maximally separated at two arms of the waveguide ($\sim 130 \mu\text{m}$), we quench the Gradient-coils (Sec.3.2.4) to apply a magnetic field gradient along the waveguide (x axis), and the phase difference can be expressed as:

$$\Delta\phi = \int_t \frac{\mu_{mLi}[B_1(t) - B_2(t)]}{\hbar} dt, \quad (4.5)$$

where μ_{mLi} denote the magnetic dipole moment of Lithium molecule, B_1 and B_2 are the magnetic field experienced by the separated clouds. Because the quench time is significantly shorter than the period of the trap, both clouds are considered to be stationary during phase imprinting. We scan the differential phase by quenching different current levels through the coil, and we perform measurements with interaction varying from $333a_0$ to $982a_0$.

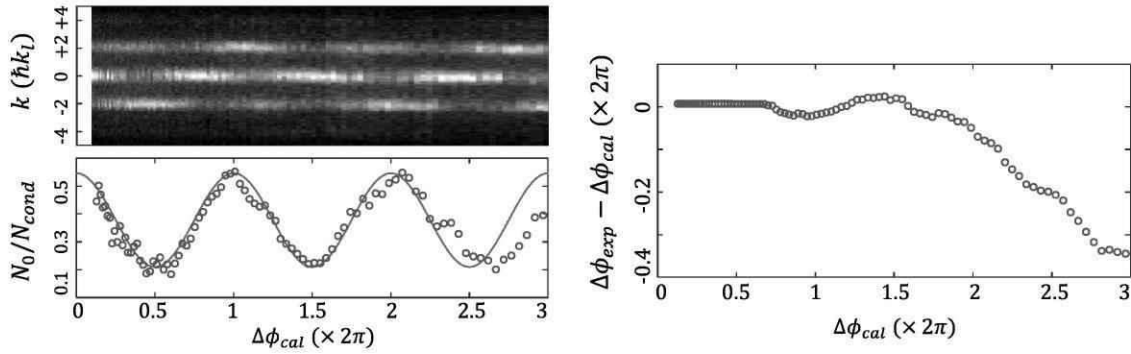


Figure 4.15.: Interference measured at $a = 487a_0$. (left) The signals from the interferometer are shown in a carpet of differential phase and the population ratio of 0^{th} momentum mode. The red solid line plotted the calculated interference with scaled amplitude and corrected the initial phase. (right) The difference of phase between the experimental measurement and calculation.

To determine the occupation in each momentum mode, we apply the same two-part function fitting introduced previously, and obtain the particle numbers N_i in the momentum mode $2i\hbar k$. The background population is removed and only the condensate peaks are included in the analysis ($N_{cond} = \sum_{i=-2}^{(2)} N_i$).

Figure 4.15 presents the result obtained at $487a_0$. It can be seen that the experimental measurement could match the calculated expectation within the error range when the given phase shift is small ($\Delta\phi_{cal} < 4\pi$). However, at a larger phase shift, a stronger field quench has to be given, which influences the trap geometric and causes the cloud

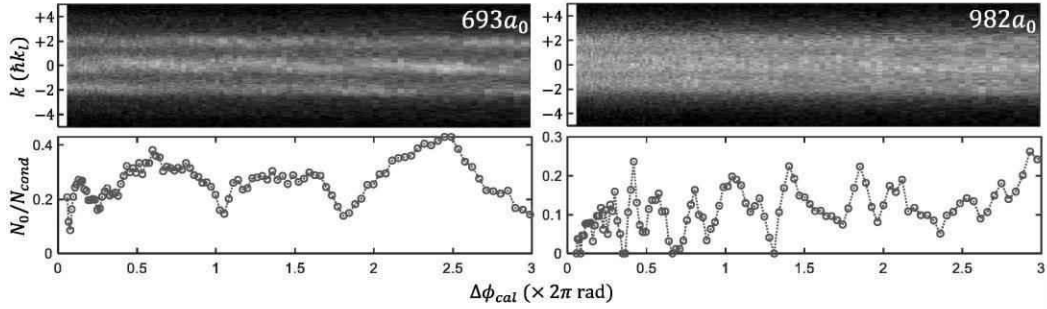


Figure 4.16.: Interference measured at $B = 675$ G, $a = 693a_0$ and $B = 700$ G, $a = 982a_0$. It can be seen that the contrast of the oscillation is already very low.

to move during the quench. As a result, the distance between the two arms of the interferometer is shortened and the applied phase shift deviated from the expected value. This distortion could also be observed from the carpet, where a tilt in the evolution can be seen.

At stronger interaction, the scattering loss becomes more extreme and the two-part fitting technique is less effective in removing the background. From the previous section (Sec 4.1.4) we have already discussed the loss mechanism caused by incoherent collision while two clouds of particles move against each other. This loss process happens three times during the interferometer operation at split, recombination and detection, and naturally makes the system vulnerable to interaction.

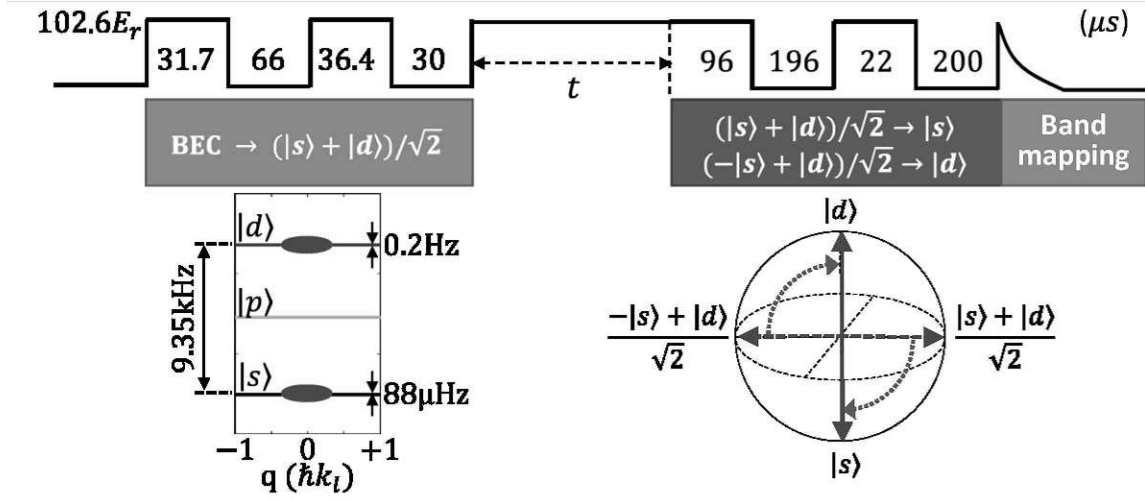
4.2.2. Ramsey Type

Developed by Norman Ramsey in the 1940s, the Ramsey interferometer was made for measuring the transition frequency of particles. By putting the atoms into a superposition of states, the energy between them could be precisely determined. It does not require the spatial separation of the two "arms", which is ideal for studying the effect of interaction.

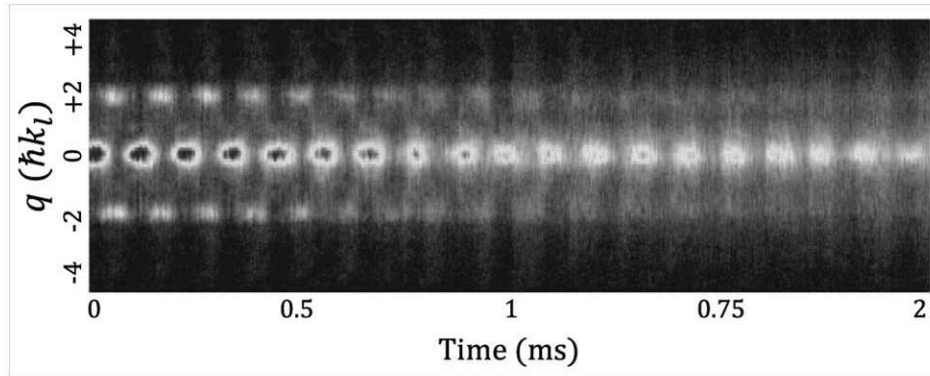
The Ramsey configuration is realized by treating two Bloch bands in the optical lattice as a spin-1/2 system, which is the ground band $|s\rangle$ and second excited band $|d\rangle$. In this experiment, the bandwidths of the two chosen bands are four orders of magnitude smaller than the energy gap between them, so the broadening of band transition arising from quasi-momentum distribution is neglected.

We first prepare a molecular BEC consisting of 3500~9500 particles. The difference in particle numbers is the result of different loss rates at various interactions. Using a short-cut loading method [75], the BEC is transferred into the superposition state

4. Scattering from Optical Lattice



$|\psi\rangle = (|s\rangle + |d\rangle)/\sqrt{2}$ of the optical lattice, which can be seen as a combination of two processes: loading into $|s\rangle$ and $\pi/2$ rotation. The fidelity of this transfer is calculated to be 98.4% under zero interaction. After the superposition state is held in the lattice for time t , a second $\pi/2$ rotation is given such that the state is transferred back to $(|s\rangle + |d\rangle)/\sqrt{2} \rightarrow |s\rangle$ and $(-|s\rangle + |d\rangle)/\sqrt{2} \rightarrow |d\rangle$ respectively. Immediately afterward, the band population is read out by the band mapping technique.



The above shows the quasi-momentum measurement with various holding times at $487a_0$ and particle number $N = 7500$. A damped oscillation between the $|s\rangle$ band and $|d\rangle$ band can be clearly seen. To quantify the effect of interaction, we analyze each evolution measurement by fitting the $|s\rangle$ band population $p_s(t) = N_s(t)/N(t)$ to the function:

$$p_s = \frac{A}{2} \cdot e^{-\lambda_c t} \cos(\omega t + \phi) + B \cdot e^{-\lambda_b t} + C \quad (4.6)$$

The fitting parameters are: interference frequency ω , diffraction phase shift ϕ , Maximal contrast A , contrast decay rate λ_c , offset B, λ_b, C . The fitting results of different interactions are plotted in Figure 4.17.

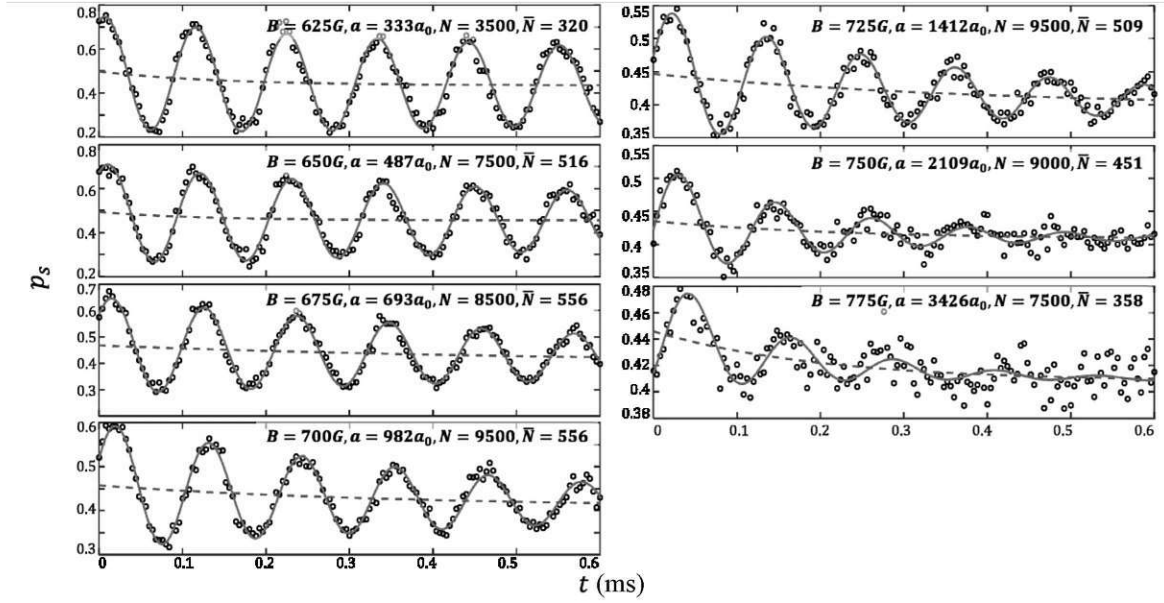


Figure 4.17.: Coherent oscillations at varying interactions. The total particle numbers N and the weighted-average particle number per lattice site \bar{N} are indicated for each dataset. The fitting results are plotted in a red solid line, and the blue dash line indicates the monotonic decreasing offset.

The results clearly demonstrate a growing decay of contrast with higher interaction. This we attribute to two different processes. First is the additional phase shift introduced by interaction during the preparation of the initial state. Since the short-cut loading calculation does not include interaction, the imbalance between $|s\rangle$ and $|d\rangle$ state (diffraction phase shift ϕ) as well as higher mode occupation (etc. $\pm 4\hbar k_l$) of the initial state increasing with interaction, which leads to decay. The second should be the same kind of incoherent collision we have with the previous experiment (Sec 4.1.4) which also takes effect during TOF.

From a closer examination of the fitting result, it is also found that the interference frequency decreases as the interaction increases. The theory prediction of energy gap between $|s\rangle$ and $|d\rangle$ at zero interaction is $\omega_0 = 2\pi \times 9.27$ kHz, and as an example, the frequency of case $487a_0$ is measured to be $\omega = 2\pi \times 9.096(33)$ kHz. This energy shift originated from the broadening of the localized wave function, which shifts the energy level of the s-band upward by a larger factor than the d-band, resulting in a decrease in the energy gap. This effect can also be interpreted as an effective reduction of the lattice depth, which has been discussed in the previous section.

Table 4.1.: Relevant quantities to the interferometers

	Ramsey (Fig 4.17)							Michelson		
a (a_0)	333	487	693	982	1412	2109	3426	487	693	982
N	3500	7500	8500	9500	9500	9000	7500	6000	6000	6000
μ/h (Hz)	214	338	409	491	568	653	737	309	356	409
$k_B T/h$ (Hz)	350	453	471	488	488	480	453	419	419	419
E_B/h (kHz)	1946	910	449	224	108	49	18	910	449	224
λ (μm)	223	97	56	33	20	12	6.3	106	64	40
\bar{N}	320	516	556	556	509	451	358	N/A		
τ_d (ms)	21	9.4	5.2	3.2	1.9	1.1	0.6	N/A		
\hbar/J ($ s\rangle$)	6600 s							N/A		

4.2.3. Interaction Induce Energy Shift

By neglecting the effect of interaction, the energy band structure of the lattice can be calculated using the Bloch theorem. At lattice depth $V_{lat} = 102E_r$, it yields an energy gap of $\omega_0 = 2\pi \times 9.27$ kHz between s- and d- band. After including interaction, each band goes through an energy shift of its own and the energy gap becomes $\omega_0 - \Delta E = \omega_0 - (\Delta E_s - \Delta E_d)$. Since each lattice site contains a different number of particles, the interaction energy shift can be written as:

$$E_{s(d),i} = \frac{N_i}{2} g_0 \int \Phi_{s(d),i}^4(r, N) dr \quad , \quad (4.7)$$

Where N_i denotes the particle number in lattice site i , $g_0 = 4\pi\hbar^2 a/m$, and the factor of $1/2$ arises from assuming an equal balance between s- and d- bands. The localized wave function $\Phi_{s(d),i}(r, N)$ could be written as a product state of the transverse and longitudinal mode under the tight-binding approximation (TBA):

$$\Phi_{s(d),i}(r, N) \simeq \omega_{s(d)}(z) \times \phi_i^{TF}(r_{perp}, N_i) \quad . \quad (4.8)$$

In the deep lattice limit, $\omega_{s(d)}$ represents the localized Wannier function in the axial direction associated with the s/d band of the optical lattice, which is independent of N_i . ϕ_i^{TF} corresponds to the radial wave function at position $z = z_i$ before applying the lattice pulse, calculated with Thomas-Fermi approximation. The total interaction

across the whole cloud is then calculated by the weighted average differential interaction energy:

$$\Delta \bar{E} = \frac{\sum_i N_i (E_{s,i} - E_{d,j})}{\sum_i N_i} . \quad (4.9)$$

In Figure 4.18 we plot the result of fitting versus the calculated differential interaction energy $\Delta \bar{E}^{int}$. Specifically, we compare the measured result of the energy gap against the theory result based on different assumptions. In the cases of weak interaction, for instead $\mu/\hbar = 214 \text{ Hz}$, the lifetime of particles in $|d\rangle$ is calculated to be 21 ms, which is much longer than the holding time. Here we observed our measurements agree with the calculated result which includes the energy shifts of both $|s\rangle$ and $|d\rangle$ states [TBA(1)]. For stronger interaction, the lifetime of $|d\rangle$ state will decrease and we calculate 0.6 ms for $\mu/\hbar = 737 \text{ Hz}$. Therefore, assuming equal population of both states is no longer accurate. Alternatively, we calculate the energy gap considering only the energy shift of $|s\rangle$ state [TBA(2)]. As shown in the figure, the measurements approaches the calculation of TBA(2) with increasing interaction. For comparison, we also perform 1D GPE simulation (also with 4.2 correction, Sec 4.1.3).

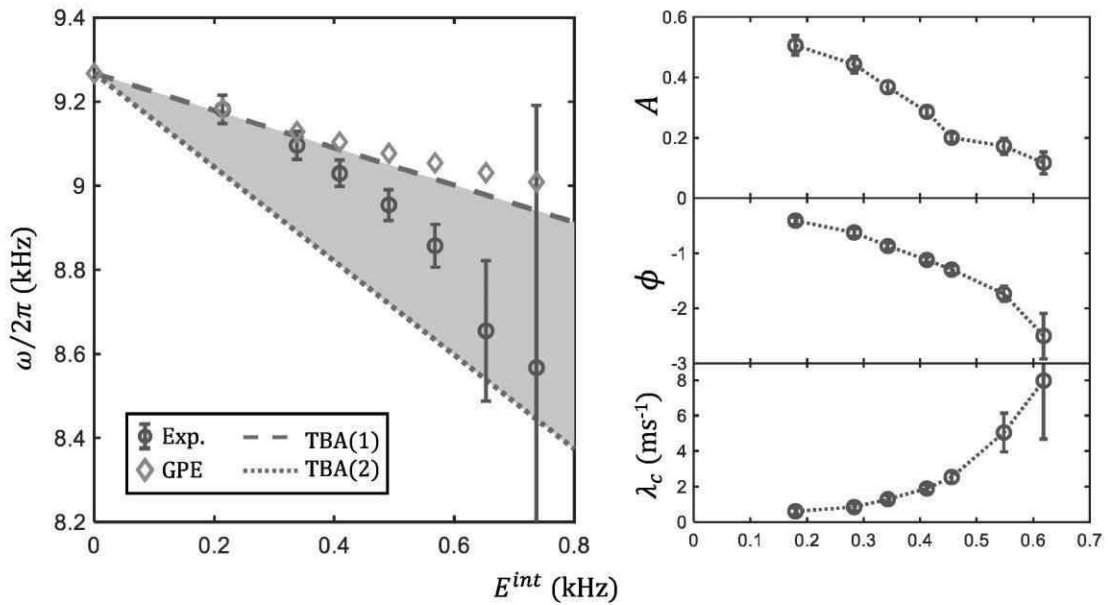


Figure 4.18.: Interaction effects in the Ramsey interferometer. Plots of oscillation frequency (ω), diffraction phase shift (ϕ), maximal contrast (A), and contrast decay rate (λ_c) as functions of calculated differential interaction energy shift between the two states ($\Delta \bar{E}^{int}$). The oscillation frequency (energy gap) is plotted with calculated result following different approximation.

5. Universal Scaling Dynamics in Strongly Interacting Bose Gas

The relaxation process of out-of-equilibrium many-body systems is an intriguing area of fundamental physics that spans a wide range of time, length, and energy scales, from the quark-gluon plasma of the early universe to the coherence of microscopic quantum systems. In recent years, rapid advancements in ultra-cold atom experiments have paved the way for new studies of relaxation dynamics. These experiments offer exceptional control over the characteristics of closed systems, enabling the exploration of fundamental processes. In the case of the relaxation process, after quenching the system into a designed initial state, its evolution can be tracked by measuring an appropriate observable, such as momentum, correlation, etc. In this chapter, the study of universal scaling phenomena in strongly interacting systems will be presented. This result is being written up in Ref.[87].

5.1. Renormalization Group and Non-Thermal Fixed Point

The idea of renormalization group (RG) emerged from theoretical studies of scale invariant systems, which have been successful in characterizing many-body systems near phase transitions[88, 89]. From the RG approach, a physical system is observed through a microscope with different magnifications of the lens. By the process of 'zooming out' from the system or 'coarse-graining', the renormalization group provides a framework for understanding self-similar evolution and critical phenomena.

Assume a self-similar dynamic described by the function $A(x)$, by observing the dynamics through a magnification s , the function could be written as a re-scaled universal function $A(x, s) = s^\zeta f(x/s)$, where ζ is the universal exponent and f is the universal function. If the re-scaled relation holds for any chosen s , for example in the thermodynamic limit, then the universal function must have taken the form of a pure power-law function $f(x) \sim x^\zeta$. The method of shifting magnification s is referred to as renormalization group flow [90] in the RG description, and such power-law behavior

signifies that the system has reached a fixed point of the flow.

By replacing the magnification factor s with the evolution time t , the RG formalism can be extended to a description of the evolution in out-of-equilibrium systems $A(x, t) = t^\alpha f(t^\beta x)$, where time evolution is equivalent to zooming in/out of the system. In this case, the system is defined as reaching a non-thermal fixed point (NTFP) [91, 92]. Furthermore, as the dynamics of the system become proportional to a power law function of time t^β , reaching NTFP also leads to the critical slowing down of the evolution.

It has been predicted that isolated systems far from equilibrium can exhibit universal scaling in time and space associated with non-thermal fixed points [93–95]. During the formation of condensate, the time evolution of momenta of the system within the scaling time window could be described by:

$$n(k, t) = t^\alpha F_s(t^\beta k) \quad . \quad (5.1)$$

Here α and β are the time-independent scaling exponents and $F_s(k)$ is the universal function. Alternatively, the universal function could be expressed as a distribution function close to the fixed point, which gives:

$$n(k, t) = \left(\frac{t}{t_0}\right)^\alpha n\left[\left(\frac{t}{t_0}\right)^\beta k, t_0\right] \quad , \quad (5.2)$$

where t_0 is any time within the scaling window.

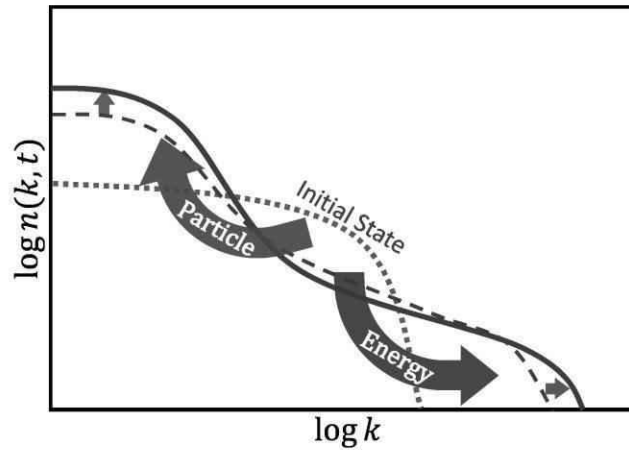


Figure 5.1.: Two-way transport of energy and particles close to a non-thermal fixed point, resulting in self-similar scaling behavior in both inferred and ultraviolet regimes of the distribution. The grey dash line indicates the non-equilibrium initial state of the system.

5. Universal Scaling Dynamics in Strongly Interacting Bose Gas

In a realistic physical system, a fixed point can only be approached approximately, since the system will be bounded by both a minimum and a maximum length scale. In this case, a pure power-law distribution will not be reached. Consider the relaxation dynamic in a closed far-out-of-equilibrium system, as shown in Figure 5.1. When we monitor the momentum evolution, the over-occupation of particles in the high-momentum modes leads to the redistribution of particles. This implies two different redistribution processes: a few particles will be transported to high-momentum modes with excessive energy, and a fraction of particles will be transported to low-momentum modes. This is referred to as two-way transport. Each redistribution process is restricted within a cutoff that is given by the maximum and minimum length scales of the system, which is referred to as inferred (IR) or ultraviolet (UV) cutoff.

The earliest experimental confirmations of universal scaling dynamics of far-out-of-equilibrium system are made with the relaxation of a spinor Bose-Einstein condensate (BEC) far from equilibrium [96] and the formation of a 1D quasi-condensate [97], where scaling behaviors in the inferred regime are observed. In a more recent experiment with a well-closed system, scaling in the ultraviolet, which is due to energy-conserving transport towards high momenta, has in addition been observed [98].

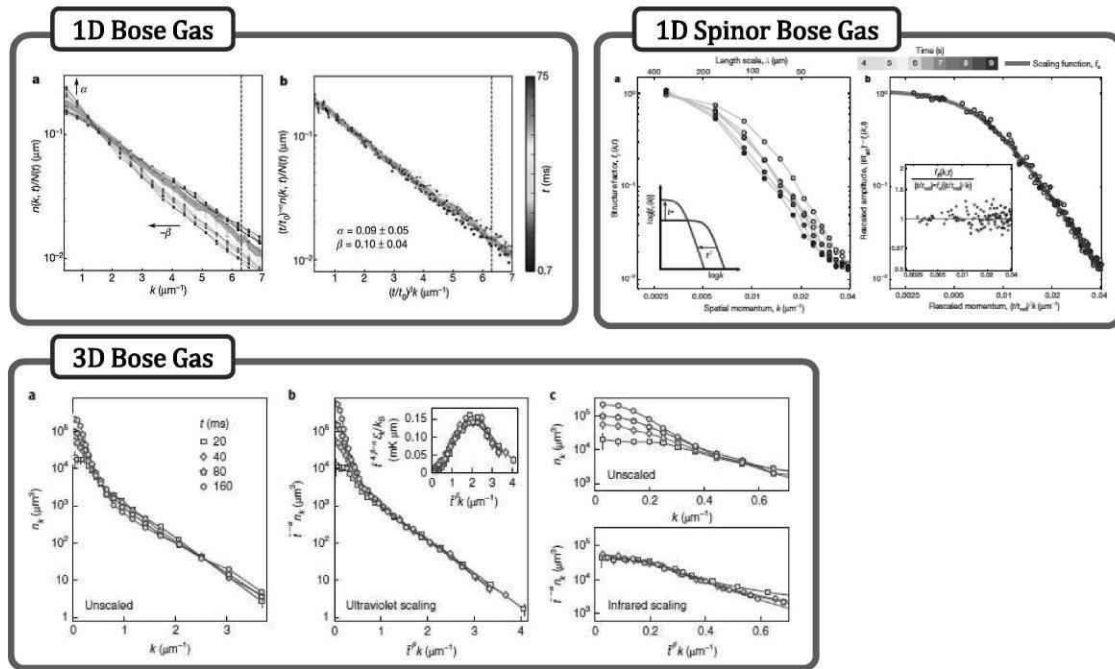


Figure 5.2.: 1D Bose Gas [97]. 1D Spinor Bose Gas [96]. 3D Bose Gas [98].

Many more experiments were performed, confirming universal dynamics in vastly

different systems [99–101]. However, it remains an open question whether universal behavior associated with non-thermal fixed points occurs for strongly interacting many-body quantum systems [102, 103].

5.2. Experiment

We performed experimental studies of universal behavior for strongly interacting boson gas, and the schematic of the setup is shown in Figure 5.3. We start with a near pure molecular BEC with $\sim 1 \times 10^4$ Feshbach molecules composed with $|1\rangle$ and $|3\rangle$ spin states. The BEC is trapped in a combined potential formed by a focused dipole beam (referred to as "carpet beam", see Sec 3.3) and magnetic field curvature, which gives trapping frequencies $(f_x, f_y, f_z) = (16, 100, 100)$ Hz. A broad spectrum of excitations is generated by a speckle laser pulse oriented perpendicular to the trapping beam. After a certain time of evolution, the capture beam is turned off and the cloud is released from the dipole trap, and matter-wave focusing is realized by the magnetic potential (Sec 3.4.1). The momentum distribution is measured with absorption imaging after 14 ms of time-of-flight.

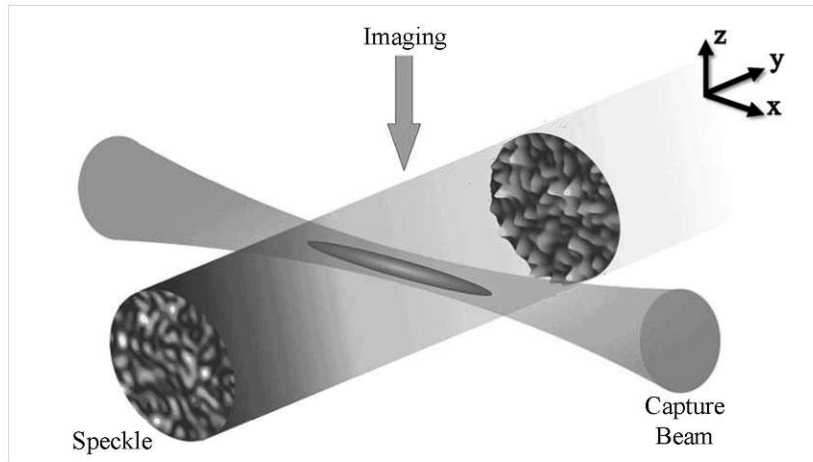
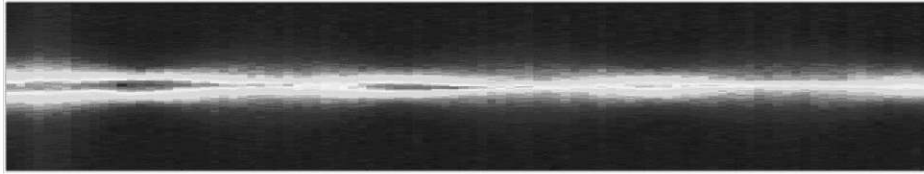


Figure 5.3.: Schematic setup of scaling experiment.

By observing the evolution under different Feshbach fields, we are able to study the thermalization of an out-of-equilibrium system with scattering lengths ranging from $500a_0$ to $4000a_0$. The speckle pulse duration is chosen such that the system will evolve through the transition, such that a partially condensed cloud would be observed when thermalized.

5.2.1. Breathing Suppression

When quenching the strongly interacting cloud in a harmonic trap, there is a common problem that breathing is excited. Reducing the breathing mode has been one of the biggest challenges of this experiment since the observation of momentum through TOF focusing would be impossible in the presence of breathing. Many different methods of quenching have been tried and failed, all resulting in an oscillating cloud.



In the end, the breathing problem was solved by an approach originating from a hand-waving naive idea: If the speckle excitation is "pushing" the particles outwards, maybe the breathing motion can be countered by pulsing the speckle when the particles are moving inward.

"Magic Squeeze"

We introduce a second dipole beam oriented perpendicular to the capture beam. By pulsing this "Squeeze" beam, we compress the BEC in the longitudinal direction and actively induce a breathing motion. Subsequently, we excite the cloud with a pulse of speckle potential while the BEC is breathing.

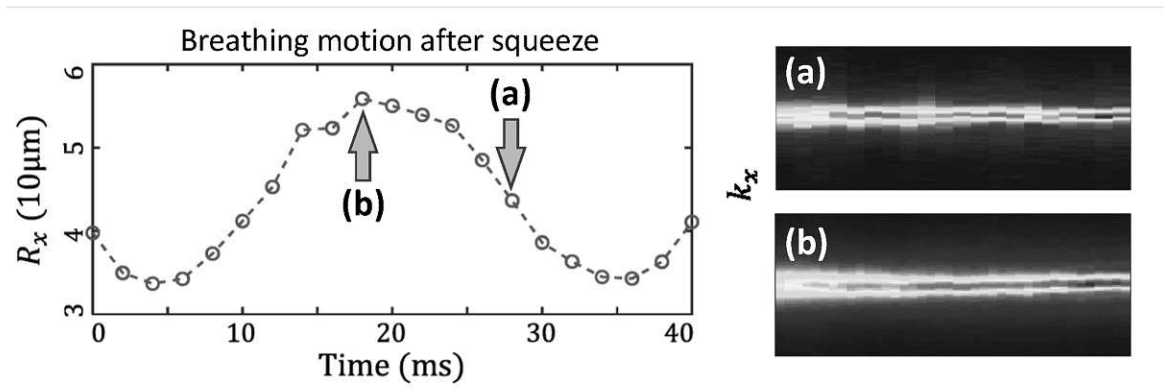


Figure 5.4.: (left) Breathing oscillation induced by the squeeze quench. (right) Momentum evolution after pulsing speckles at different times. It could be observed that the breathing mode basically vanishes when pulsing at maximum size.

As shown in Figure 5.4, breathing mode can indeed be suppressed by including this squeezing process. Further to our surprise, the breathing motion can be eliminated if the speckle pulse is applied when the cloud expands to its maximum size. This method remains effective for particle numbers larger than 4000.

To gain a better understanding of this squeezing process, we have performed 2D Gross Pitaevskii simulations to recreate the phenomenon (Details refer to the bachelor thesis of Christoph Fritzl [104]). A decay of breathing mode is observed from the simulation, and we try to find the connection between the decay rate and the time for pulsing the speckle. By fitting the breathing profiles to a decaying oscillating function $Ae^{-\gamma t}\sin(\omega t + \phi) + c$, we gain the decay factor γ and plot against the time for speckle. From Figure 5.5, a maximum γ is observed, with the time corresponding to the maximum size during BEC expansion. Limited by the nature of 2D simulation, it can not replicate the thermalization process after the speckle excitation. Nevertheless, it does reproduce the breathing suppression qualitatively.

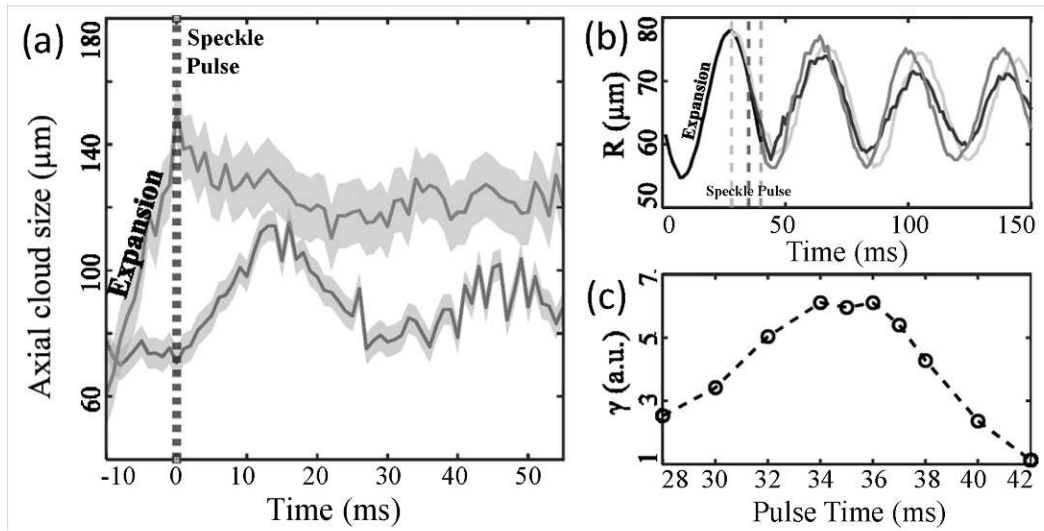


Figure 5.5.: (a) In situ longitudinal size measurements of a direction speckle pulse and the squeeze-pulse process. Size obtained from the Gaussian fit of density profile, which can not fully describe the evolution, thus the fluctuation. (b) Width of the simulated density profiles of squeeze-pulse processes for different times of pulsing. (c) The fitted decay rate of the oscillation is plotted with the time for pulsing. A clear maximum can be observed, with pulse time pointing towards the maximum size of the squeezed oscillation.

Double Speckle Pulses

Inspired by the 'magic squeeze' method, a simpler idea of breathing suppression comes to mind. In the procedure of 'magic squeeze', the speckle pulse is given at the maximum

amplitude of the breathing motion. Since a speckle pulse could excite the breathing motion, the squeeze process could be replaced by an additional speckle pulse, and the quenching process turns into a double speckle pulse sequence.

From the principle of universality, the scaling dynamics during the thermalization process should be insensitive to the initial state, as long as the initial state is far-out-of-equilibrium and the Hamiltonian of the system remains the same. However, as will be shown in the later section, we observe different behavior from two different breathing suppression methods.

5.2.2. Vertical Speckle Setup

The speckle potential excites the system in the x - z plane, by the dynamics in the z direction can not be observed since they are integrated out by our imaging system. In order to observe the momentum evolution of the z -axis, we also conducted the experiment with the speckle beam aligned vertically (Figure 5.6). With imaging and speckle in the same axis, we could image both dimensions parallel to the speckle plane.

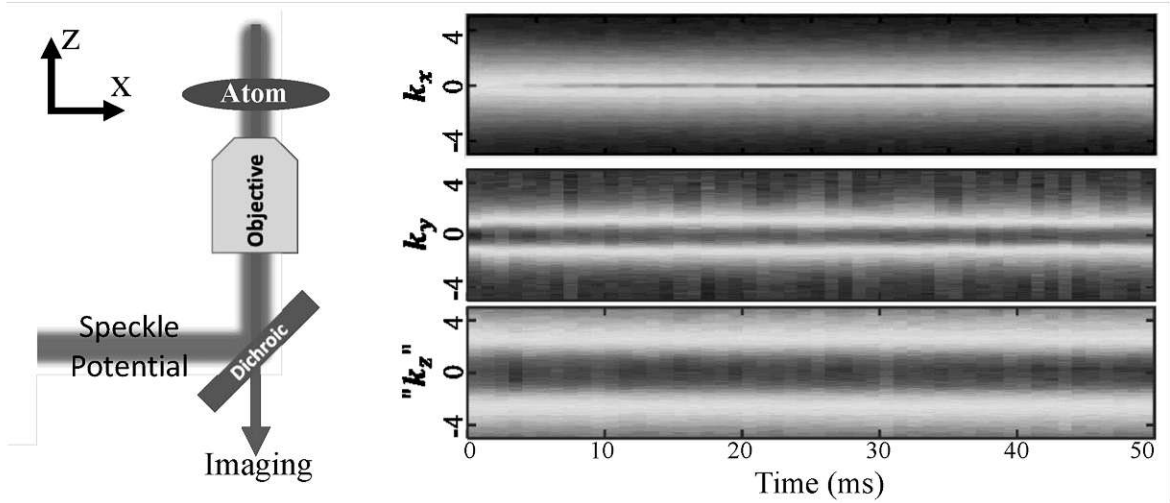


Figure 5.6.: (left) Schematic diagram of the vertical speckle setup. (right) Momentum evolution follows the speckle pulse in all directions. The momentum " k_z " is obtained from the measurement of transverse momentum in the vertical speckle setup.

The momentum evolutions along all three directions are plotted as time carpet in Figure 5.6. In the k_x axis, the evolution from an out-of-equilibrium system towards condensation can clearly be observed. Also, it is evident that the speckle potential has created a high excitation in " k_z ", as compared to along the speckle beam k_y . However, there are barely visible dynamics in the axis of k_y and " k_z ". Other than the first 3 ms

of evolution in k_y , where a broadening can be seen, the momentum distribution is almost stationary during the evolution for the transverse dimension of the cloud.

5.3. Scaling Analysis

Likelihood Calculation

The scaling exponents α and β are determined by calculating the likelihood function which calculates the mutual deviation between the momentum profiles re-scaled according to the chosen exponents:

$$L(\alpha, \beta) = \exp \left[-\frac{1}{2} \chi^2(\alpha, \beta) \right] \quad (5.3)$$

with

$$\chi^2(\alpha, \beta) = \frac{1}{N_t^2} \sum_{t, t_0}^{N_t} \int_0^{k_{cutoff}} \frac{[(t/t_0)^\alpha n((t/t_0)^\beta k, t_0) - n(k, t)]^2}{\tilde{\sigma}^2((t/t_0)^\beta k, t_0) + \tilde{\sigma}^2(k, t)} dk, \quad (5.4)$$

where N_t is the number of measured momentum profiles within the selected time window, $n(k, t)$ is the momentum distribution and $\tilde{\sigma}$ is the standard error of mean calculated from multiple measurements. For any choice of values α, β , evaluates the likelihood of the validity that the exponents satisfy a universal scaling relation.

By integrating the likelihood $L(\alpha, \beta)$ (Figure 5.7, in this thesis, $\Delta = \alpha - \beta$ is taken instead of α for convenience) along α and β , we could obtain the most likely value and error range for each exponent from the distributions.

In principle, calculating the likelihood function examines all the possible combinations of scaling exponents (within a given range) and calculates the sum of the squared difference between each scaled profile. The fitting result from the likelihood table reveals the set of exponents that produce a minimum difference, hence the scaling exponents that "scale" the best. However, an optimum solution almost always exists for any profiles given, and the validity of the solution needs to be checked by other means. In this thesis, we check the ratio of the χ^2 functions for scaled and the unscaled profiles $\chi_{0,0}^2/\chi_{\alpha,\beta}^2$, which gives a quantitative evaluation for the scaling.

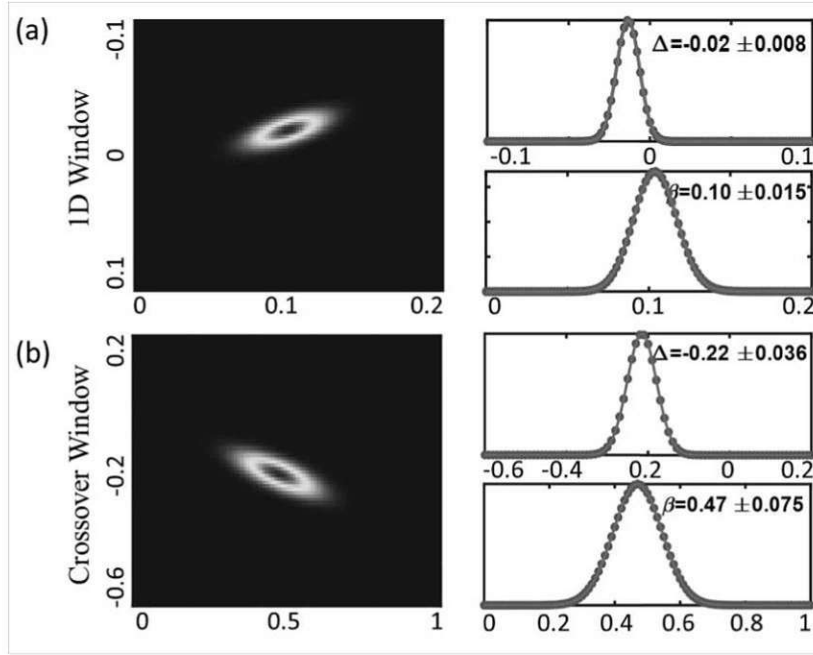


Figure 5.7.: (left) The likelihood table $L(\beta, \Delta)$. (right) Integration and Gaussian fit of the distribution. In this analysis, the likelihood function is scanned with β and $\Delta = \alpha - \beta$.

5.3.1. Identify Scaling Windows

To identify the scaling behavior, we need to determine two parameters for the likelihood analysis: the time window and momentum cutoff. In order to minimize human bias, we choose a small time window of 5 ms and momentum cutoff of $0.5 \frac{1}{\mu\text{m}}$, then perform likelihood analysis over the whole evolution by moving the time window. Theoretically speaking, an ideal scaling behavior should give the same result with a smaller range of time and momentum. So by monitoring the value of $\chi^2_{0,0}/\chi^2_{\alpha,\beta}$, the time window could be found where the scaling behavior is presented.

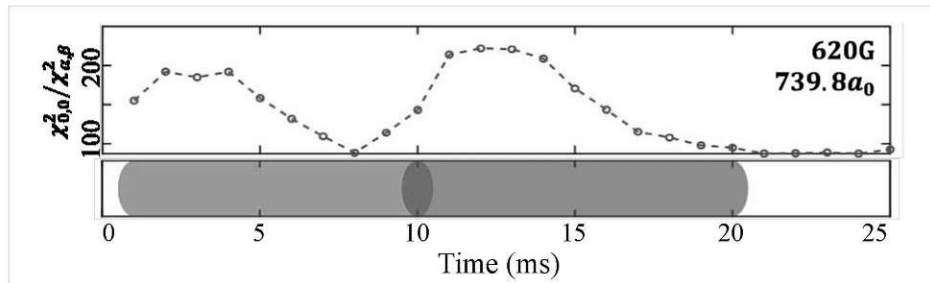


Figure 5.8.: The χ^2 calculation for particle number ~ 10000 and scattering length $740a_0$ ($B=620$ G). The lower graph marks the two scaling windows found with this method.

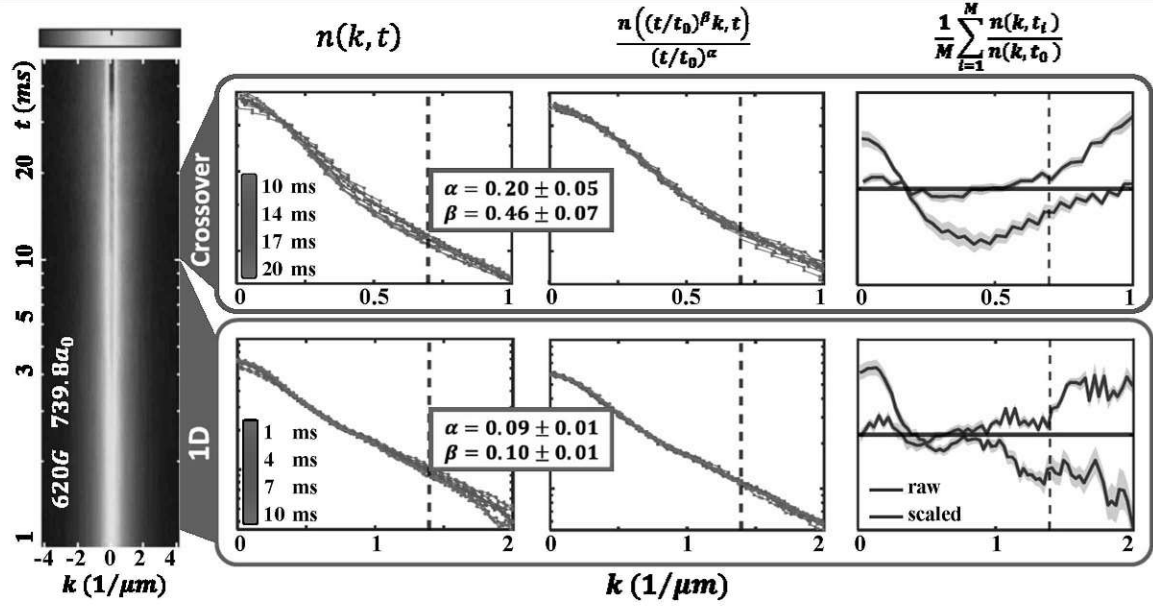


Figure 5.9.: (Carpet) Longitudinal momentum evolution measured with $B=620$ G, $a=740a_0$. The raw (left) and scaled (middle) momentum profiles within the “1D”(down) and “crossover”(up) scaling windows. (right) The mean ratio of raw and scaled profiles is divided by the reference profile. The scaling cutoff is marked by vertical dash lines.

Figure 5.8 shows the example of calculation for relatively low interaction cases $a \approx 740a_0$. It can be seen that the likelihood analysis gives two separate peaks, which suggests there are two different scaling windows within a single evolution. To specify the time window, we fix the lower boundary of the time window given by the $\chi^2_{0,0}/\chi^2_{\alpha,\beta}$ value (1 ms and 10 ms for the two peaks) and perform likelihood analysis by scanning the upper boundary. Again, we monitor the value of the chi-square ratio and an obvious decrease will show once the upper bound goes beyond a certain value.

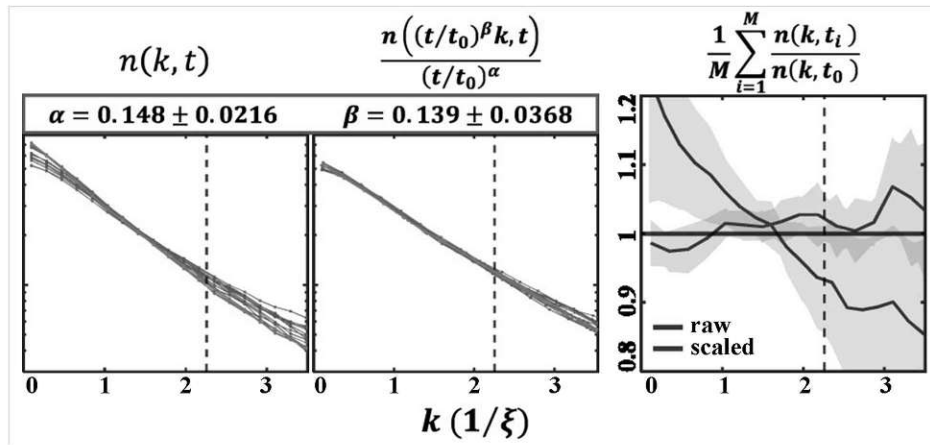


Figure 5.10.: Scaling behavior measured with scattering length $622.5a_0$ and particle number $N=4000$. The scaling window is identified to be 16 ± 1 ms.

With time windows fixed, we could scan for the momentum cutoff using the same approach. After finding both the scaling windows and momentum cutoff, we managed to verify the existence of two separate scaling windows with self-similar scaling behaviors, as shown in Figure 5.9.

To access a wider range of interaction strengths, we also perform experiments with different particle numbers and magnetic fields. Restricted by the experimental condition, we measure with particle number range from 4000 to 10000 and scattering length from $600a_0$ to $3000a_0$. An example of a low particle number is shown in Fig 5.10, where we can see an increase in the value of exponents. Since the breathing-canceling process does not work for systems with a particle number below 4000, the efficiency of this process could have already dropped while lowering the particle number. As a result, some "leftover" breathing modes would be captured by the scaling analysis due to their similarity, and thus increase the value of exponents. One other drawback of lowering particle numbers is the requirement to increase the signal-to-noise ratio by binning data points. Consequently, identifying the second scaling window is not possible because of a lack of statistics.

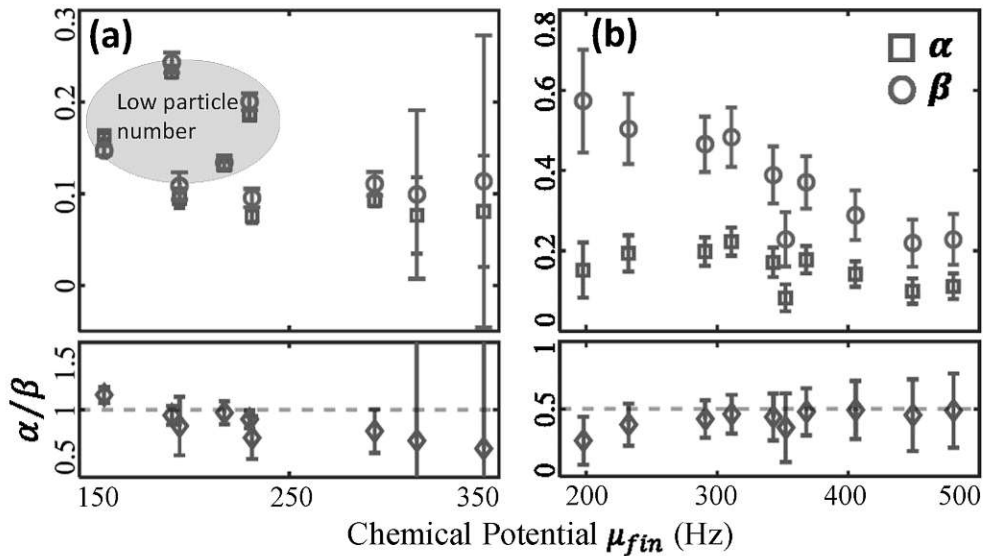


Figure 5.11.: Scaling exponents and the ratio of "1D" and "crossover" windows versus the chemical potential of the condensate component of the final state. As the "1D" window decreases with increasing interaction, scaling exponents can no longer be determined for $\mu_{fin} > 350\text{Hz}$ due to limited statistics, which could also be seen from the increase of the error bar. On the other hand, since $\mu_{fin} < 200\text{Hz}$ could only be achieved by reducing particle number in our system, the "crossover" window could not be well identified due to the limited signal-to-noise ratio.

In order to make a reasonable comparison between different measured results (Fig 5.11), we represent the interaction strength in the form of the chemical potential μ_{fin} , which is calculated from the BEC portion of the final state by adapting Thomas-Fermi approximation.

Universal Function

By the definition of universal scaling, the momentum profile within the scaling time window should be able to collapse into one universal function. We follow the convention of previous works and consider the universal function to be:

$$f_s = \frac{1}{1 + k^\zeta}.$$

By fitting every momentum profile with the universal function, we could collapse all distributions within the momentum cutoff into a single function for both scaling windows, and the result is displayed in Figure 5.12.

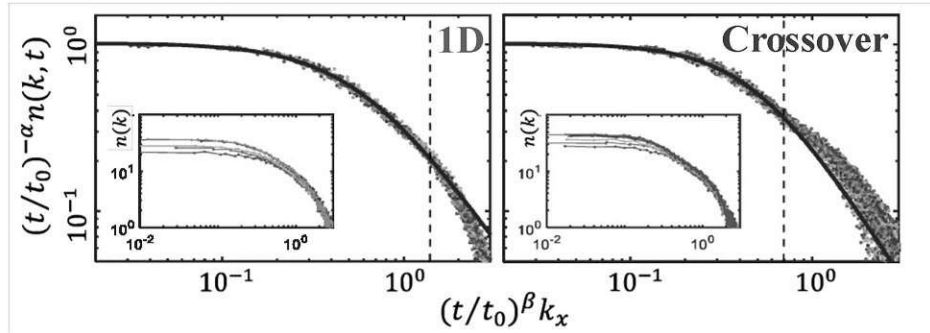


Figure 5.12.: Re-scaled momentum profiles (dots) and the fitted universal function (solid line) for all distributions in both scaling windows. The vertical dash lines mark the scaling cutoff. The inserts plotted the initial profiles of each window for all interactions.

Our fitting result gives the value of exponent $\zeta = 1.604 \pm 0.011(1.766 \pm 0.014)$ for 1D (crossover) scaling window.

Although the profiles could be collapsed into a single function, the value of the exponent does not match with the expected value of $\zeta = 2$ [97], which comes from the "Lorentzian term" of the theory distribution (Eq 5.7 in Sec 5.4.1). We found the discrepancy is related to the momentum offset of the folded distribution. When an offset term is introduced to the folded universal function $f_s \sim [1 + (k + k_0)^\zeta]^{-1}$, we found the value of ζ changing from 1.6 to 2.6 when setting k_0 to be a free fitting parameter (Fig 5.13).

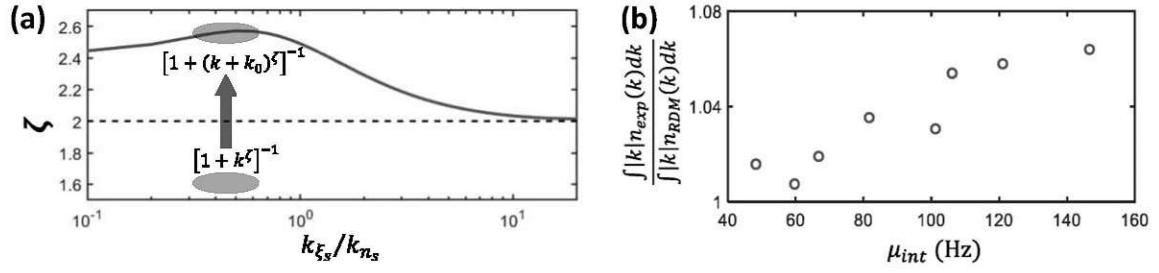


Figure 5.13.: (a) Value of the exponent ζ (solid line) by fitting to the theoretical distribution $[1 + (\frac{k_{\xi s}}{k_{n s}})^2 (\frac{k}{k_{\xi s}})^2]^{-1}$ (Sec 5.4.1), and comparison to the fitting value of the experimental data (red area). (b) The ratio of the total momentum $\int |k|n(k)dk$ between the theory model and measured distribution.

When transforming $k \rightarrow |k|$, we determine the $k = 0$ by fitting the momentum profile to a concentric double-gaussian function, so an extra k_0 momentum offset would suggest an overall increase in momentum. This could be related to the release of interaction energy during focusing (Sec 3.4.1). When the cloud is released from the dipole trap, most of the interaction energy is released into the transverse dimensions, especially the vertical direction where it is anti-trapping. However, a small fraction of the interaction energy would still be released in the longitudinal direction, such that the momentum distribution we observe may contain an offset factor k_0 . As shown in Figure 5.13, if we calculated the difference between the theoretical model (Sec 5.4.1) and the measured distribution, the ratio between the measured and theory momentum shows an increasing trend with higher interaction.

1D Scaling Window

In the first scaling window, we observe scaling exponents of $\alpha \approx \beta$ which suggests 1D scaling dynamics. So we name it the "1D" scaling window. Furthermore, the duration of "1D" time window is found to decrease with increasing interaction.

We take a naive conjecture that the scaling time window follows a power law relation with the interaction of the system $\Delta t \sim \mu_{fin}^{-k}$, such that it fits the intuition for a non-interacting system, which will take infinitely long to thermalize. To compare results in different systems, we plot our measured time windows versus chemical potential (μ_{fin}) divided by the radial trapping frequency (100 Hz for Li data and 3.3 kHz for Rb data). As shown in Figure 5.14, when we extrapolated the fitting result to less interacting systems, the scaling time window of the ^{87}Rb experiment [97] shows an agreement to the power law fit, which suggest a universal law that is governing such evolution. More detailed analysis will be shown in the later section (Sec 5.4).

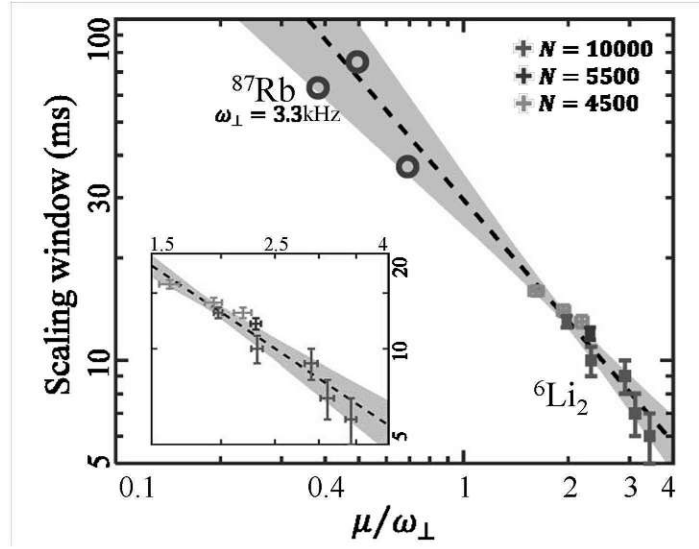


Figure 5.14.: The 1D scaling time window versus the interaction strength of the system. To compare with the previous experiment, the x -axis is plotted with chemical potential μ_{fin} calculated from the condensate portion of the final state, divided by radial trap frequency. Horizontal error calculated from the variation of particle number. Purple circles are measurements from ^{87}Rb experiments [105].

Crossover Scaling Window

In the second scaling window, we observe scaling exponents of $\alpha \approx \frac{1}{2}\beta$, with the time window relatively stable versus interaction strength. Interestingly, both the starting time and the duration of the second window are in the order of inverse transverse trap frequency ($2\pi/\omega_{\perp}$). We perform additional measurements with different trapping geometry ($f_{\parallel} = 16$ Hz, $f_{\perp} = 56$ and 200 Hz), and the results (Fig 5.15) confirm the connection of second scaling window to transverse dynamic. So we named it the "crossover" scaling window.

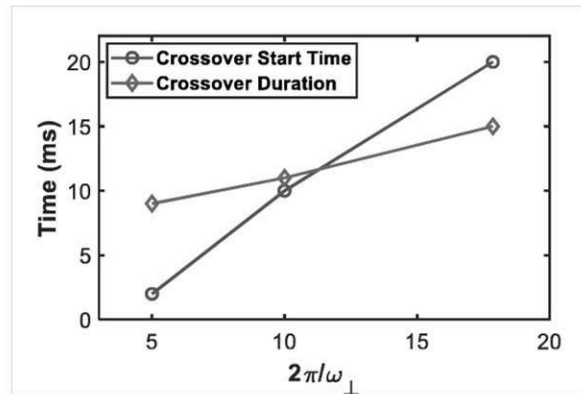


Figure 5.15.: Starting time and duration of "crossover" scaling window plot versus the inverse trap frequency.

However, from the result of Figure 5.6, we fail to observe any obvious transverse dynamics. Furthermore, the abnormal ratio between scaling exponents in the second window is also not yet understood. The preliminary thought is, that the transverse collision could be coupled to the longitudinal direction, decreasing particle transport towards inferred (low momentum) and increasing the particle transport towards UV (high momentum), thus the relation of $\alpha < \beta$. Unfortunately, our experiment does not possess the sensitivity to verify such a phenomenon.

Alternative Initial State

As mentioned previously (Sec 5.2.1), a "double-pulse" scheme could also be used to suppress breathing mode during evolution. As shown in Figure 5.16, unlike in the "squeeze-pulse" scheme, only the crossover ($\alpha < \beta$) scaling window can be found. It can be seen that the system could go through different relaxation paths by preparing an alternative initial state, which could be switched by altering the quenching process.

When we compare the initial states produced by two quenching schemes (Figure 5.17), we can easily see the distinction, which gives a possible explanation for the absence of the first scaling window. In the later section (Sec 5.4), we have associated the "1D"

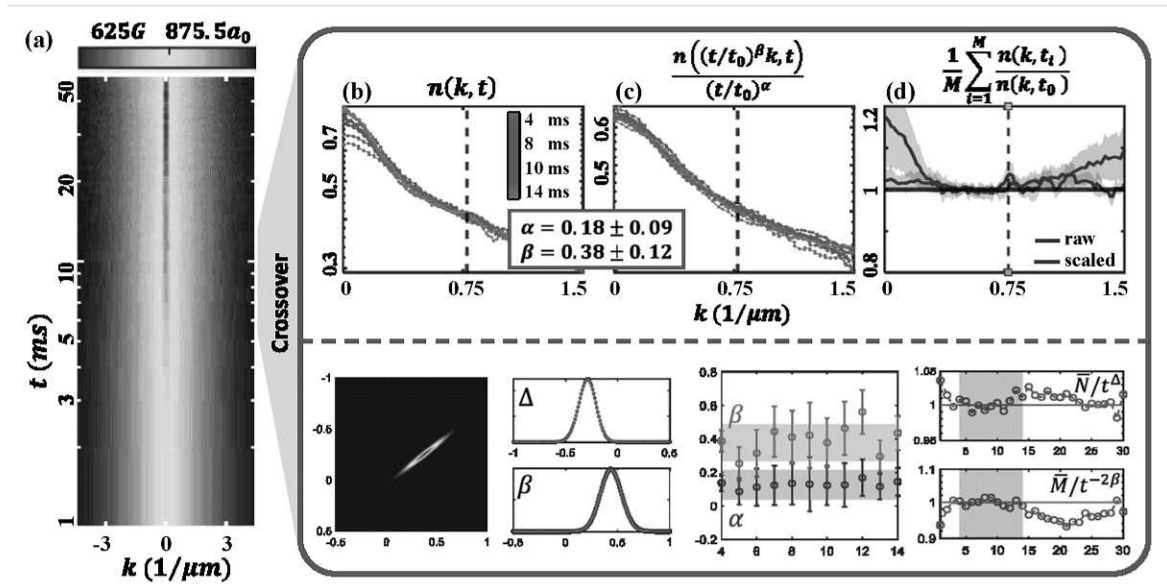


Figure 5.16.: (a) Longitudinal momentum evolution measured with $B=625\text{ G}$, $a=875.5a_0$ using the "double-pulse" scheme. The raw (b) and scaled (c) momentum profiles. (d) The mean ratio of raw and scaled profiles is divided by the reference profile. The scaling cutoff is marked by vertical dashed lines. The lower part shows the likelihood calculation and scaling check.

window to the decay of the solitonic state, which obviously would require the formation of solitons during/after the quench. However, in the 'double-pulse' scheme, the phase coherence of the cloud is already broken after the first speckle pulse, and no soliton could form with the second speckle pulse.

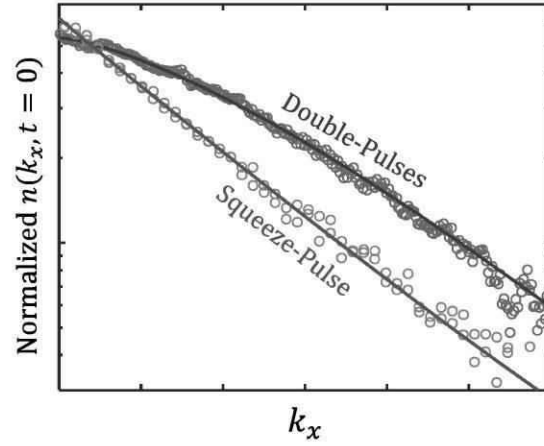


Figure 5.17.: Momentum profile of initial state ($t=0$) prepared with different cooling schemes. We plot both distributions with the fitting result to $\sim \exp(-ak^\gamma)$, where $\gamma = 1.057$ for the 'squeeze-pulse' sequence and $\gamma = 1.397$ for 'double-pulse' sequence.

5.3.2. Scaling Check

Likelihood analysis almost guarantees to produce a result with any given set of profiles. So after we have acquired the scaling exponents, they have to be checked independently against other algorithms for validation. In this section, we demonstrate two checking methods that have been used in this work.

Exponent Robustness Check

By definition, the universal distribution function $f_s(k) = n(k, t_0)$ and the reference time t_0 can be any chosen point within the scaling window. As a result, the same exponents should be found regardless of which time point is chosen to be the reference, and the results should also agree to the exponents found by the scaling analysis which calculates the deviation sum using all time points as reference. Based on this argument, we could test the robustness of the scaling analysis by checking the value of exponents using every point within the scaling window as the reference separately.

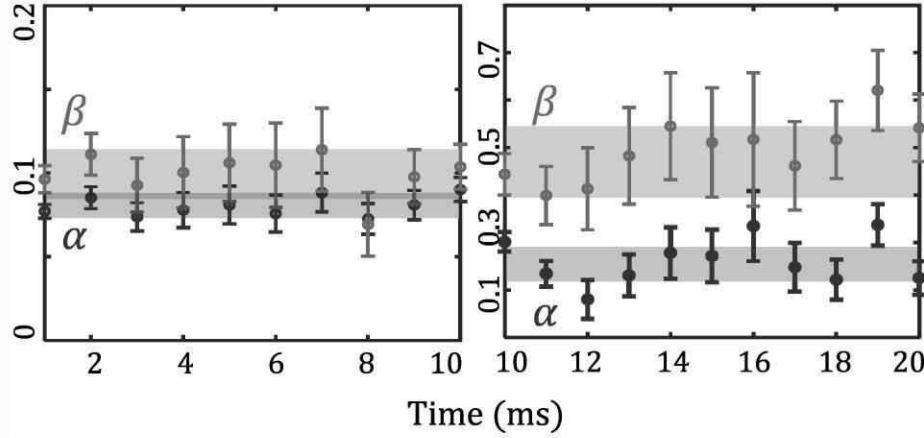


Figure 5.18.: Robustness checking calculation for (left) "1D" and (right) "Crossover" window in Fig 5.9. The solid areas indicate the error range of exponents calculated from scaling analysis. Each point represents the result of choosing the corresponding time.

As shown in Figure 5.18, it can be seen that the result of the robustness check is relatively stable and within the error range. This confirms the robustness of this analysis, suggesting the scaling behavior and exponents found are valid.

Global Variable Calculation

As required by the conservation laws, the particle number and kinetic energy within the scaling window must follow the relations [97]:

$$\overline{N}(t) = \int_{|k| \leq (t/t_0)^{-\beta k_s}} \frac{n(k, t)}{N(t)} dk \propto t^{\alpha - \beta} , \quad (5.5)$$

$$\overline{M}_{m \geq 2}(t) = \int_{|k| \leq (t/t_0)^{-\beta k_s}} \frac{|k|^m n(k, t)}{N(t) \overline{N}(t)} dk \propto t^{-m\beta} . \quad (5.6)$$

$N(t)$ is the total particle number, k_s is the scaling momentum cutoff and m is any integer bigger or equals to two. In this thesis, we choose $m = 2$.

\overline{N} and \overline{M} are referred to as global variables. They represent the particle number and average kinetic energy ($m = 2$) in the scaling regime, and the calculation is independent of the scaling analysis (likelihood calculation). As a result, global variables are useful for validation of the scaling exponents. Since we have found two sets of scaling exponents, the global variables need to be calculated based on both cases. As shown in Figure 5.19, the rescaled value of global variables $\overline{N}/(t/t_0)^{\alpha - \beta}$ and $\overline{M}/(t/t_0)^{-m\beta}$ stay constant

within the respective scaling regime, which confirms the value of the exponents.

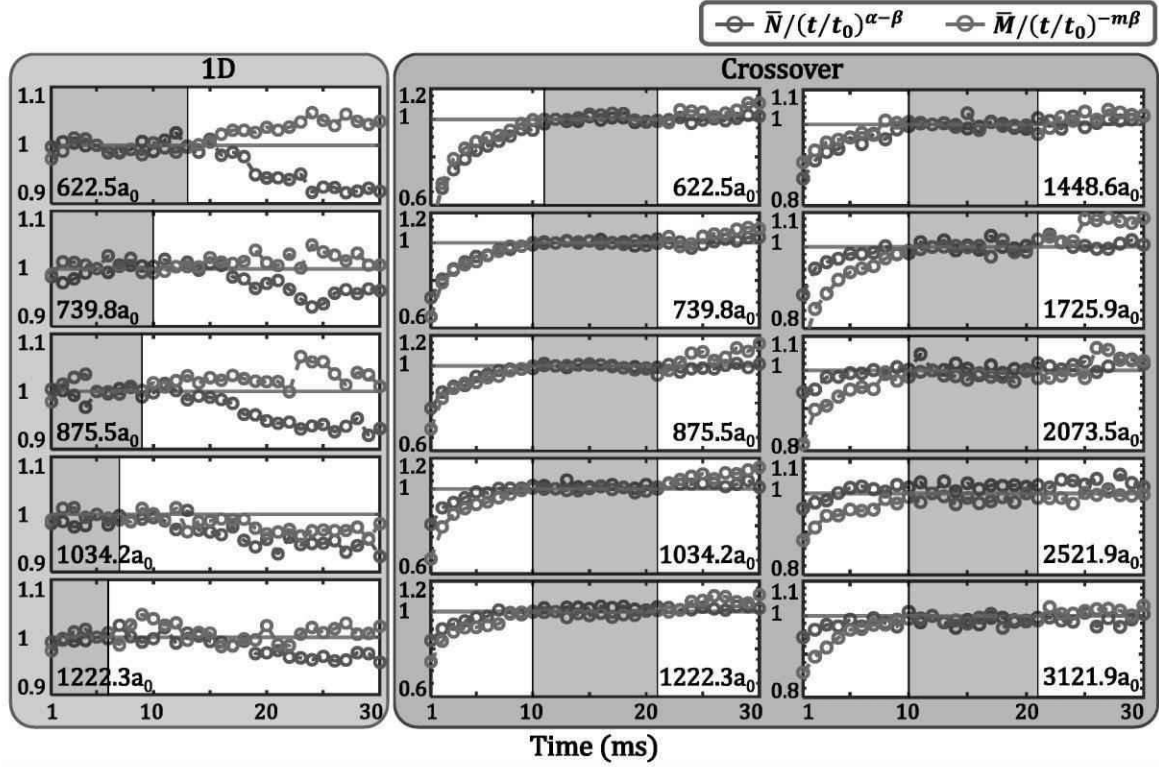


Figure 5.19.: Global variable calculation for data sets measured with 7000~10000 particle number. The values of \bar{N} and \bar{M} are rescaled by the respective exponential function, such that the value should be 1 in the scaling regime, marked by the red horizontal line. The gray area indicates the scaling windows.

5.4. Thermalization of Solitonic State

When considering the momentum spectrum of a single soliton (or vortex), the geometry of the vortex suggests a power-law distribution of velocity flow away from the core [106], which matches the description of universal distribution function occurs at NTFP (Sec 5.1). In the previous ^{87}Rb experiment [97], such distribution was observed and the result was mapped to the Random Defect Model (RDM) [107]. In our measurements, we observe similar scaling behavior with $\alpha \sim \beta \sim 0.1$ in the "1D" scaling window,

and the momentum distribution is also found to be similar to an exponential function of momentum (Fig 5.9 and 5.10), which match the description of RDM for high momentum. In this case, we will also describe the scaling dynamic in the "1D" window with RDM.

It is important to note that the "solitons" in our system are not real solitons. The more appropriate name for them should be "soliton-like defect" or "density fluctuation with phase shift" (Fig 5.20). The RDM was originally developed as a description for an ensemble of randomly distributed solitonic defects in 1D Bose gas, and we extend the model to describe the generalized solitonic defect (GSD) states. In this thesis, for convenience, we retain the name of "soliton".

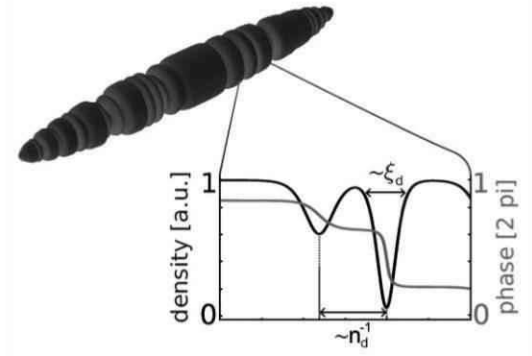
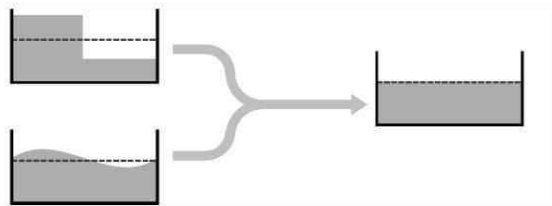


Figure 5.20.: An illustration of 3D soliton.

Chemical Potential of Initial State

Previously (Fig 5.11) we have defined the chemical potential of our system μ_{fin} from the final (thermalized) state. However, such a definition may no longer be valid while comparing different systems with different quenching schemes. The major results we would like to compare to, namely the ^{87}Rb experiment, have non-negligible atom loss after the system is thermalized, which would give an inaccurate calculation of μ_{fin} . Furthermore, even with distinct initial states, systems may still go through different paths and thermalize to the same final state.



So we would like to re-calculate the chemical potential of our system from the initial state:

$$\mu_{int} = n_0 \eta g_{1D} \quad \text{with} \quad n_0 = \max[n(x, t = 0)] \quad \text{and} \quad g_{1D} = \frac{16\hbar^2 a_0}{3mR_{TF}^2}$$

where $n(x, t)$ is the in-situ 1D density distribution along the longitudinal direction, a_0 is the scattering length, m is mass of the particles, R_{TF} is the Thomas-Fermi radius of the transverse direction and $\eta = 4.2$ is the correction term obtain in Sec 4.1.3 for high interaction. The form of g_{1D} is obtained by integrating the radial direction assuming the Thomas-Fermi profile. The healing length could also be calculated accordingly $\xi_h = \frac{\hbar}{\sqrt{2m\mu_{int}}}$. Since μ_{int} is calculated from the in-situ density distribution of the initial state, we expect it to give a better description of the interaction strength during the evolution. Unfortunately, the in-situ measurements were only done for some of the configurations (8 out of 14), but they already cover most of the scenarios we would like to discuss.

5.4.1. Random Defect Model (RDM)

From 1D GPE, the solution of single soliton $\phi = |\phi|e^{i\varphi}$ takes the form of a localized density suppression associated with a φ phase shift, and ϕ can be written as:

$$\phi_\nu = \sqrt{n} \left[\gamma^{-1} \tanh \left(\frac{x - x_s(t)}{\sqrt{2} \gamma \xi} \right) \right]$$

where n is the homogeneous background density, $x_s(t) = x_0 + \nu t$ is the position of the soliton, $\gamma^{-1} = \sqrt{1 - \nu^2}$, and $\nu = \frac{v_s}{c_s}$ is velocity of the soliton relative to the speed of sound. From the correlation between velocity and "depth" of a soliton, factor ν is also known as the "greyness" of the soliton. For mathematical simplicity, we assume

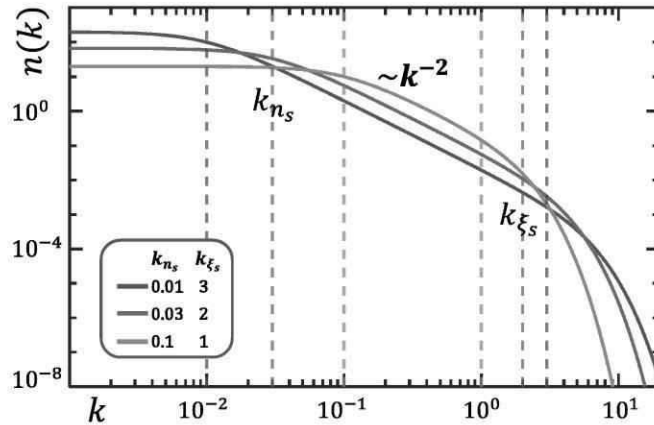


Figure 5.21.: Momentum distributions of solitonic state plotted in double Logarithm scales with different combinations of soliton width and density. An power-law relation of $\sim k^{-2}$ can be observed in the region between k_{n_s} and k_{ξ_s} .

5. Universal Scaling Dynamics in Strongly Interacting Bose Gas

the velocity of solitons is much smaller than the speed of sound $\nu \approx 0$ and the solitons are taken to "black" ($\nu = 0, \gamma = 1$). Furthermore, we neglect the correlation between different solitons, and the ensemble of solitons with positions ($x_i : i = 1, \dots, N_s$) would be:

$$\phi^{N_s}(x, t) = \sqrt{n} \prod_{i=1}^{N_s} \frac{\phi_{\nu_i}(x - x_i)}{\sqrt{n}}$$

Then the generic form of the momentum spectrum of the soliton ensemble can be obtained by taking the Fourier transform of $\langle \phi^{N_s}(x) * \phi^{N_s}(y) \rangle$ with respect to $(x - y)$:

$$n(k) = \left[\frac{2n_0 k_{n_s}}{k_{n_s}^2 + (k - k_0)^2} \right] \left[\frac{k/k_{\xi_s}}{\sinh(k/k_{\xi_s})} \right]^2, \quad (5.7)$$

where $k_{\xi_s} = \sqrt{2}/(\pi\xi_s)$ is the momentum scale related to the width ξ_s of single soliton, $k_{n_s} = 2n_s$ is the mean distance between solitons with n_s being the soliton density and k_0 is the bulk momentum of the soliton ensemble relative to the background. As shown in Figure 5.21, the spectrum can be seen as three regions separated by k_{n_s} and k_{ξ_s} .

However, fitting the full solitonic distribution function to the experimental data is challenging due to the inter-dependence of parameters k_{n_s} and k_{ξ_s} , which are both essential to characterize the distribution. So a direct fitting attempt to the full function will result in a large error for both parameters. Instead, we could first determine the width of solitons by fitting the exponential range of the distribution (high momentum range), where the distribution could be approximated by:

$$n(k) \propto \exp(-2 \frac{k}{k_{\xi_s}}) \quad (5.8)$$

Afterward, we fix the value of k_{ξ_s} and fit the full function to the momentum distribution to obtain the soliton density n_s and the results are shown in Table 5.1.

Table 5.1.: Lithium data ($^6\text{Li}_2$), $(\nu_l, \nu_L) = (16, 100)$ Hz

a_s [a_0]	N	μ_{int} [h Hz]	ξ_h [μm]	T_{final} [nK]	1D-scaling			crossover-scaling			ξ_s [μm]	n_s [μm^{-1}]
					α	β	$t[\text{ms}]$	α	β	$t[\text{ms}]$		
623	3934	n/a	n/a	35.5	0.163	0.147	16	n/a	n/a	n/a	1.38(4)	0.499(43)
740	4388	n/a	n/a	36.4	0.233	0.243	14	n/a	n/a	n/a	1.33(3)	0.524(19)
876	4312	n/a	n/a	35.8	0.131	0.134	13	n/a	n/a	n/a	1.54(4)	0.266(39)
740	5570	n/a	n/a	38.6	0.186	0.20	12	n/a	n/a	n/a	1.55(4)	0.302(16)
623	6777	48.26	2.96	43.2	0.095	0.108	13	0.152	0.574	9	1.29(2)	0.483(15)
740	7500	59.65	2.66	43.8	0.075	0.095	10	0.194	0.504	10	1.41(3)	0.403(22)
876	7853	66.77	2.51	43.6	0.093	0.111	9	0.198	0.466	10	1.48(3)	0.394(14)
1034	9267	81.68	2.27	46.1	0.076	0.099	7	0.223	0.483	10	1.61(3)	0.291(68)
1222	9184	101.22	2.04	45.7	0.081	0.114	6	0.171	0.389	10	1.65(3)	0.287(53)
1449	9300	106.13	1.99	46.4	n/a	n/a	n/a	0.083	0.228	10	1.65(3)	0.372(22)
1726	9345	121.07	1.87	46.9	n/a	n/a	n/a	0.178	0.371	10	1.70(3)	0.302(48)
2074	9323	146.64	1.70	46.9	n/a	n/a	n/a	0.142	0.289	10	1.72(3)	0.361(12)
2522	9553	n/a	n/a	47.1	n/a	n/a	n/a	0.099	0.219	10	1.72(3)	0.360(07)
3122	10063	n/a	n/a	48.4	n/a	n/a	n/a	0.111	0.228	10	1.85(4)	0.326(08)

Nonuniform Background Density

In Equation 5.7, a homogeneous background density n_0 is assumed. In our experiment, such an assumption is not valid, and we need to investigate further the impact of an inhomogeneous background.

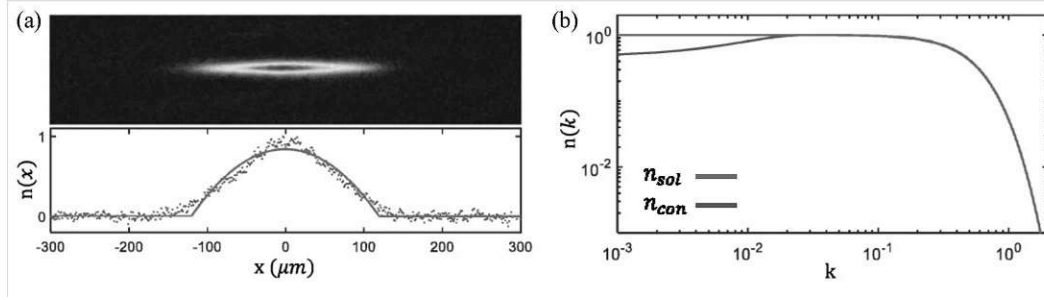


Figure 5.22.: (a) Thomas-Fermi fit of the in-situ density. (b) The full convoluted distribution n_{con} is plotted with the homogeneous background distribution n_{sol} .

From the theory, the constant density factor is replaced with the field function $\sqrt{n} \rightarrow \psi(x, t)$. Assuming a steady background, the full one-body momentum distribution can be calculated with convolution $n(k) = n_0(k) * n_{soliton}(k)$, where $n_{soliton}$ is basically Equation 5.7 without n_0 . Then we assume a Thomas-Fermi background distribution and phase coherence before the speckle quench, and the background momentum $n_0(k)$ can be calculated from Fourier transform. The Thomas-Fermi radius is obtained by fitting the 1D in-situ density distribution before the speckle, and the full one-body momenta can be calculated as shown in Figure 5.22. It can be seen that with a nonuniform background, the distribution only deviates in the low momentum range, which is already close to the spatial resolution of our experimental measurement. As a result, the nonuniform background will not have influence on our study.

5.4.2. Decay of Solitons

For a system quenched across a second-order transition, the nucleation of defects is expected from the Kibble-Zurek (KZ) mechanism. Although the heating process in our experiment is more complex than one simple quench, we believe the excitation is predominantly the result of the speckle pulse, which could be considered as a quench of the system. Thus the same dynamics should be expected.

Predicted by the theory of RDM, soliton density would decay with $n_s \sim t^{-\beta}$, and we observe exponent $\beta = 0.095$ from scaling analysis. As shown in Figure 5.23, the previous fitting is performed for distributions during the evolution, and a decay of

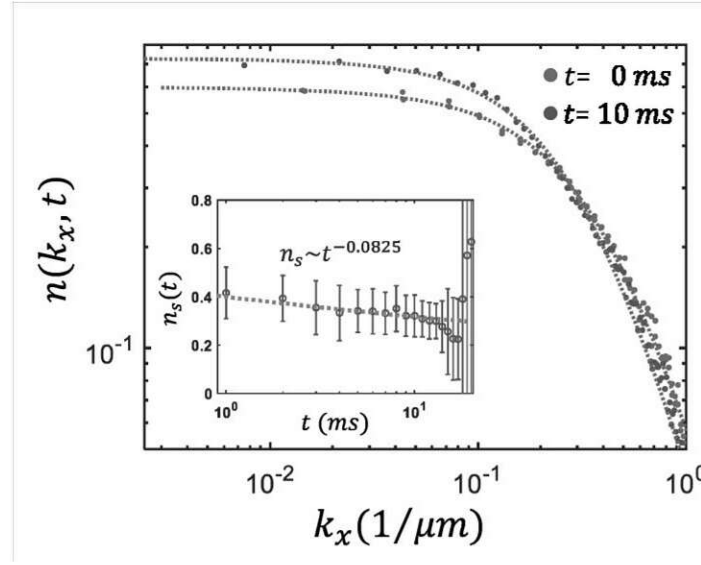


Figure 5.23.: Soliton distribution fit for $a = 740a_0$, $N \sim 7500$ at $t = 0, 10$ ms. The insert shows the soliton density during evolution.

soliton could be observed at the rate of $n_s \sim t^{-0.0825}$. Given the large uncertainty of soliton densities produced by the fitting, the value of exponent (0.0825) also comes with a large uncertainty.

Dimensionless GPE

For a better understanding of universal behavior, we could derive the dimensionless form of GPE based on our definition of dimensionless quantities. First, we start with a 3D GPE:

$$i\hbar\partial_t\psi = \left[-\frac{\hbar^2}{2m}\nabla^2 + V(r) + g_{3D}|\psi|^2 \right] \psi \quad . \quad (5.9)$$

In our system, the potential takes a cigar-sharp with weak confinement along the x-axis and strong confinement along the y and z-axis:

$$V(r) = \frac{1}{2}m\omega_{\parallel}^2x^2 + \frac{1}{2}m\omega_{\perp}^2(y^2 + z^2)$$

where ω_{\parallel} is the longitudinal trap frequency and ω_{\perp} is the transverse trap frequency. Furthermore, we define the chemical potential $\tilde{\mu}$ calculated from the peak density of initial state:

$$\tilde{\mu} = n_0 g_{3D}, \quad \text{with} \quad n_0 = \max(|\psi(t=0)|^2) \quad ,$$

and the healing length could also be calculated accordingly:

$$\xi_n = \frac{\hbar}{\sqrt{2m\tilde{\mu}}} \quad .$$

Next, we re-define the scale of the system into dimensionless quantities:

$$\begin{aligned} r &\rightarrow \bar{r} = \frac{r}{\xi_n}; & \nabla &\rightarrow \bar{\nabla} = \nabla \xi_n \\ t &\rightarrow \bar{t} = t\omega_\mu = \frac{t\tilde{\mu}}{\hbar}; & \partial_t &\rightarrow \partial_{\bar{t}} = \frac{1}{\omega_\mu} \partial_t \\ \psi &\rightarrow \bar{\psi} = \frac{\psi}{\sqrt{n_0}}. \end{aligned}$$

and the dimensionless form of Equation 5.9 can be rewritten as:

$$i\partial_{\bar{t}}\bar{\psi} = \left[-\bar{\nabla}^2 + |\bar{\psi}|^2 + \bar{V}(\bar{r}) \right] \bar{\psi}$$

with the potential term:

$$\bar{V}(\bar{r}) = \frac{\hbar^2\omega_\parallel^2}{4\tilde{\mu}^2}\bar{x}^2 + \frac{\hbar^2\omega_\perp^2}{4\tilde{\mu}^2}(\bar{y}^2 + \bar{z}^2) \quad .$$

We further simplify the equation by defining $\gamma_\parallel = \frac{\hbar\omega_\parallel}{2\tilde{\mu}}$ and $\gamma_\perp = \frac{\hbar\omega_\perp}{2\tilde{\mu}}$, and the GPE will take the form:

$$i\partial_{\bar{t}}\bar{\psi} = \left[-\bar{\nabla}^2 + |\bar{\psi}|^2 + \gamma_\parallel^2\bar{x}^2 + \gamma_\perp^2(\bar{y}^2 + \bar{z}^2) \right] \bar{\psi} \quad . \quad (5.10)$$

Noted that in Equation 5.10, the dynamic of normalized wavefunction $\bar{\psi}$ becomes universal, and only has dependence on parameters γ_\parallel and γ_\perp , namely the initial peak density n_0 and trap frequency $(\omega_\parallel, \omega_\perp)$, which is matching our observation on the experiment.

Universality

We plot in Fig 5.24 the dimensionless scaling time $\Delta t\omega_s$ versus ξ_s/ξ_h and $\mu_{int}/(\hbar\omega_\perp)$ for both systems. The dimensionless scaling time is the scaling window time (Δt) normalized by the energy calculated from the density of soliton $\omega_s = \frac{\hbar^2 k_{ns}^2}{2m}$ where m is the mass of particle, and ξ_s/ξ_h shows the size of the solitons normalized by the healing length and $\mu_{int}/(\hbar\omega_\perp)$ gives the "1D-ness" or integrability breaking of the system.

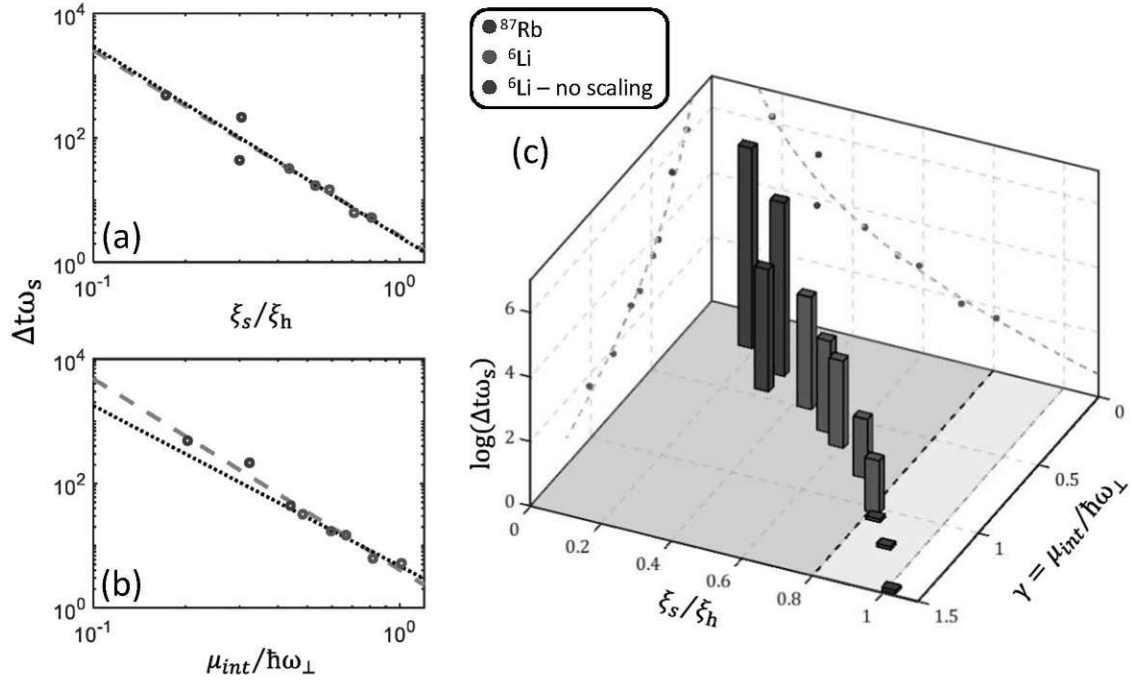


Figure 5.24.: Dimensionless scaling time ($\log_{10}(\Delta t \omega_s)$) plot via (a) the reduced size of soliton (ξ_s/ξ_h) and (b) the '1D-ness' ($\mu_{int}/(\hbar\omega_{\perp})$) of the system for both ^6Li and ^{87}Rb experiments in logarithm scale. Dotted line indicate the power law fitting result of ^6Li measurements and dash line indicate the fitting result that include both experiment. (c) The 3D diagram that combines the two plots. The three red blocks represent the data sets in ^6Li experiment that do not observe '1D' scaling behavior.

The figure shows the basin of attraction towards the universal fixed point located at $\gamma = \xi_s/\xi_h = 0$, where the value of scaling time diverges. This conceptually agrees with our understanding of dimensionality, since a pure 1D system is integrable and does not thermalize, the system will not evolve and thus take infinitely long to leave the NTFP [108].

From the RDM, we expect scaling behavior driven by the dynamic of the soliton ensemble, which would vanish for $\xi_s/\xi_h \geq 1$ as soliton becomes stable. However, in our experiment, the cutoff of scaling behavior is observed at $\xi_s/\xi_h \approx 0.8$. We believe that it is caused by the small scaling time window, where the dynamic duration becomes comparable to the time resolution. Due to the limitation of experimental resolution, the scaling analysis may no longer recognize the behavior. This will result in a large error for likelihood calculation, which could be seen in Fig 5.11.

The above result signals the existence of a universal NTFP which is governing

the thermalization of quasi-1D system. Unfortunately, limited by the experimental constraints, the initial states we created can only explore a small fraction of the phase space shown in the figure. We are also unable to study the dependence of the thermalization on the solitons or the dimensions independently since they are correlated by the quenching process. For further studies, we plan to explore the phase space by numeric simulation, which hopefully will give us a better understanding of the dependence of the thermalization process.

6. Conclusion and Outlook

In this thesis, I have presented the design and functionality of our ultra-cold atom experiment with ^6Li species. By controlling interaction strengths through Feshbach resonances and exciting systems into desired initial states, we were able to investigate fundamental processes such as thermalization and relaxation. Additionally, experiments on diffraction from periodic potentials and the thermalization of far-from-equilibrium systems under strong interactions provided insights into non-equilibrium phenomena and universal scaling behaviors. These studies showcase both the capabilities and potential of our experimental setup. As the employed techniques continue to advance, further exploration of quantum phase transitions and out-of-equilibrium dynamics will become possible.

Future Experiment

Universal scaling dynamic in 2D box trap

The universal scaling dynamics of a strongly interacting system were observed during the course of this thesis. Unfortunately, we are not able to explore the phenomena with a large variety of conditions due to the limitations of our system. To improve the experiment, we would like to increase the degrees of freedom accessible by loading the BEC into a single layer of the lattice trap. Furthermore, we have designed and tested a combination of Digital-Micromirror-Device (DMD) and axicon setup with which a circular box trap could be possible. By conducting the experiment in a 2D box trap, we could avoid the breathing problem of a harmonic trap. Additionally, omitting the breathing cancellation will greatly reduce the complexity of the quenching process, and we will be able to design the excitation with DMD, hoping to better understand the scaling dynamics.

Scattering from accordion lattice and correction for GPE at high interaction

In Chapter 4, we have presented our study on the scattering of highly interacting Bose-Einstein condensate from a periodic potential. The scattering process shows a

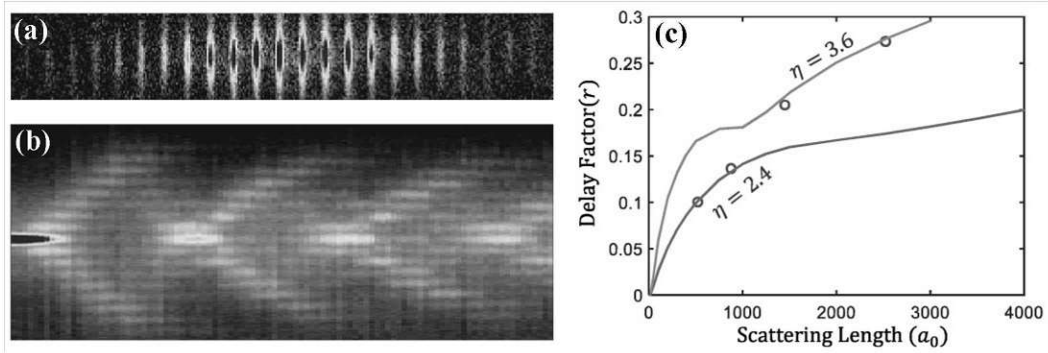


Figure 6.1.: (a) In-situ image of BEC loaded into lattice with spacing $\sim 15\mu\text{m}$. (b) Momentum evolution of BEC diffracted from the lattice potential with scattering length $520a_0$. (c) Delay factor calculation plot with GPE simulation. The delay effect can no longer be compensated by a single correction factor, suggesting a nonlinear discrepancy of GPE at high interaction.

delay effect stronger than the perdition given by the Gross-Pitaevskii simulation, and the interaction term g needs to be amplified by an extra factor $\eta = 4.2$.

To further investigate the enhancement of interaction on the scattering process, we designed and constructed an accordion lattice setup where the lattice spacing can be tuned in the range of $3\mu\text{m} \sim 20\mu\text{m}$, such that the interaction effect can be tested with different lattice configuration. When this thesis was drafted, we had already tested this setup with a lattice spacing of $\sim 15\mu\text{m}$, and a different value of η is observed (Fig 6.1).

Generalized hydrodynamics

Unlike conventional fluids, where interactions lead to chaotic dynamics and thermalization, integrable systems maintain an extensive number of conserved quantities, which profoundly influence their dynamics. In the interest of describing integrable systems, generalized hydrodynamics (GHD) has recently become a focused field of physics for the reason that it allows the study of complex non-equilibrium phenomena such as the propagation of different modes, diffusion, and shock waves.

Combining the setups mentioned above, multiple 1D/2D traps could be created with designed potential, allowing multiple 1D gases to be observed in a single-shot imaging. With the property of lithium, studies of GHD could be performed with strong interacting quasi-BEC, Fermi gas or 1D gas in unitary.

FFLO state in 1D spin-imbalanced Fermi gases

In 1960s, Peter Fulde and Richard Ferrel [109], and independently Alexei Larkin and Yuri Ovchinnikov [110], predicted an exotic state of superfluid. When Cooper pairs form within an imbalanced population of fermions, the pairs form with a non-zero momentum, which leads to a spatially modulated order parameter and the fermi gas will be separated into periodic regions in space. Named after the authors, Fulde–Ferrell–Larkin–Ovchinnikov (FFLO) state demonstrates the fundamental property of competition between order parameters. But the experimental observation of FFLO state [111] has been proven challenging. With our experiment, we propose to realize such a phenomenon with an array of 1D Fermi gases, where we can directly resolve each tube. The phase modulation of FFLO state could be measured by interfering with a balanced superfluid gas.

Appendix

A. Experiment Control

The experiment is controlled with an ADwin¹ system with multiple analog/digital cards. To perform the experiment, we program the controller from a computer via TCP/IP connection. For each experimental cycle, the control program will examine whether an upload of a new cycle is needed and calculate the output data matrix accordingly. Then, judging from the task given, the control program will send the command to start a new cycle or repeat the last cycle. Since the examination and calculation can happen while the cycle is running, the experiment can continuously measure with less than 0.2s of gap between two cycles.

ADwin System

Our ADwin system currently consist of one T12 CPU module, four analog output cards, one analog input card and three digital TiCo I/O cards.

Each digital card contains a TiCo processor, so we preload a program into the processor using "BootLoader"² with a simply looping function: receive a 32-bit number and assign all output channel accordingly. In this way, the TiCo processor can share the workload of the CUP module.

There are 3 programs (processes) running in the ADwin CPU module. Every time the control program restarts, it will flush the memory of the CPU module, upload the programs and enable them. The three programs are:

- Safety thread, high priority. This is a stalled thread that will only run when receiving a TTL falling edge on the CPU #0 input. The signal is maintained by the monitor system, and will be triggered when a failure happens for the experiment (e.g. cooling water temperature). After the trigger, this thread

¹Jäger Computergesteuerte Messtechnik (<https://www.adwin.de/index-us.html>)

²This function is within the program "TiCo Basic", only valid for version "ADwin Basic" V5 or newer.

overrides the other thread and stops the ADwin system, returning all output to zero level.

- Output thread, medium priority. This thread controls the output of the system. There are 35 data lists pre-defined, one for each analog channel, one for each digital card in use and one for "Process Delay". Each list consists of 2 million 32-bit data slots, which in total occupy 280 MB of memory. In the unlikely case that this is not sufficient, the length of lists can still be extended, as the T12 CUP module has in total 1 GB of memory.

The output thread is initiated by a software trigger from the control program (PC). While running, it writes the values from the lists to the outputs, and the value of "Process Delay" determines the duration of this output. In a real experiment, it often happens that the output is held for a much longer time than the time resolution (e.g. the MOT stage), so this approach saves a lot of process power and memory. From our experience, a normal experiment cycle of 15 s takes ~ 20 MB of memory with $25 \mu\text{s}$ resolution.

- Analog Recording thread, low priority. This thread records the input voltage on the analog input card with the configuration given by the control program. It pre-defined a data list with 12 million data slots, 1.5 million for each channel, with a maximum time resolution of $1 \mu\text{s}$. The thread checks the master clock from the output thread with a time resolution of 1 ms, and decides whether to start the recording. So it is recommended to choose a slightly larger recording time range, and also record a digital signal from the ADwin output as a reference.

Our experiment control is capable of $1 \mu\text{s}$ time resolution. However, using such high time resolution is very demanding on the calculation power of the control computer. In our experiment, we set the time resolution to be $25 \mu\text{s}$, which is sufficient for most of the tasks. In a rare occasion where higher resolution is required, we could implement a delay pulse generator or waveform generator trigger by a TTL signal.

Monitor System

Independent of the control system, we use an NI ¹ device together with a LabView program to monitor and record the lab condition, most crucially the temperature and flow of the incoming and outgoing cooling water. When all readings are within safe value, the NI device maintains a high TTL signal to the safety channel. In the case where anything triggers a warning or the monitor system itself fails, the TTL signal drops to low and triggers the safety mode of ADwin system.

¹National Instruments (<https://www.ni.com/>)

B. Control Program

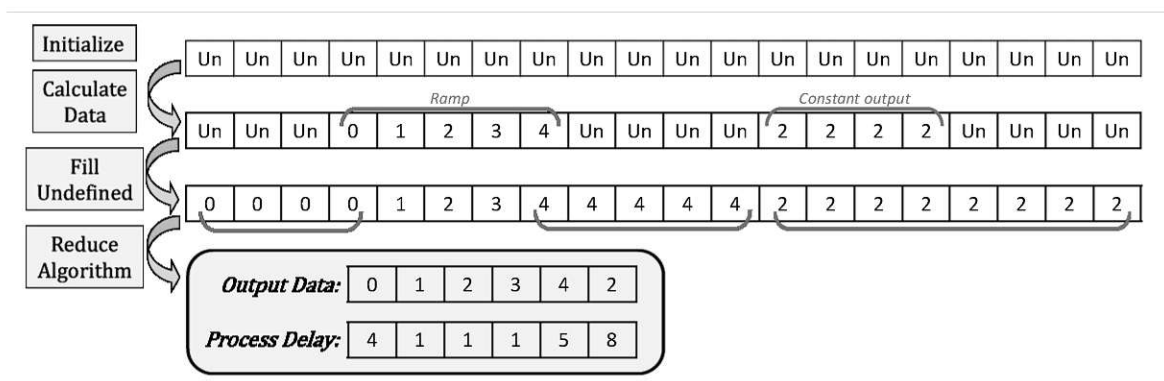
Our control program is coded in C/C++ with Qt GUI library, compiled with Qt 5.15 MinGW 8 compiler (not yet compatible with Qt 6). The source code can be found on GitHub (https://github.com/liangqibox/Lithium6_ATI). We recommend building the program with "Qt Creator" IDE and an x64 compiler is preferred.

Due to the nature of C/C++, this program could be compiled and run on any system platform. The basic functionality is to structure an experimental cycle, calculate the output matrix and update the control system accordingly, which in our case is an ADwin system. Additionally, the program contains a set of API codes that could be accessed when making other programs. With the API, it is rather easy to combine the control program of other devices and synchronize them with the experimental cycle, and the cycle setting can also be read by the devices easily. Currently, in our experiment, all cameras and function generators are run directly from the main control program.

For cycle-to-cycle data analysis, the control program saves a setting file at the beginning of every cycle, which contains the current value of all the variables. We use this file as a trigger for our analysis program (called "Acquisition"), and the next set of camera images could be recognized and analyzed by MATLAB.

Software Logic

A matrix within the output thread of ADwin CPU module is declared with size (Number of Channels+1) \times (2 · 10⁶). Before uploading a cycle, the control program will declare a matrix of size (Number of Channels) \times (cycle time/time resolution), then fill the matrix with the calculated output number. After all the defined parts of the



matrices are filled, the undefined parts of the matrix will be fixed to the closest value before it. If no defined value is presented, it will be automatically zero.

After the matrix is generated, the size is in the order of hundreds of mega-bytes. We reduce the size by combining the matrix, where all channels stay with the same output. An extra array is then made to record the time (number of matrix elements) that this output should be kept, named "Process Delay" in ADwin's terminology. With this algorithm, the output matrix could be reduced to the size $\sim 20\text{MB}$. Then the reduced matrix is uploaded to ADwin for the output of the next cycle.

Cycle Construction

Each cycle setting follows the structure of *"sequence"* \rightarrow *"section"* \rightarrow *"cycle"*. Each *sequence* represents an operation (such as a ramp) defined by the user. Multiple sequences from all channels form the structure of *section*. The output will only move on to the next *section* when all operations in the current *section* are finished. With this configuration, the beginning and end of every *section* are well aligned in time. Furthermore, each section can be individually turned on and off, so it is easy to switch between different experimental operations, such as different imaging methods.

The default units: Voltage (V), Time (ms), Frequency (kHz).

Sequence

The data type *"sequence"* is the basic building block of a cycle. Each *sequence* can be set to one pre-defined type, which contains up to four values. Each value could be replaced with a *variable*, such that their value could be easily manipulated or scanned. By right-clicking on the value entrance, one could have a table of all the available variables sorted in types.

In analog channel programming, the pre-defined output types are: *Void*¹, *Constant*, *Linear (ramp)*, *Exp (ramp)*, *Sin*, *Pulse*, *SRamp*, *Stand*. Most of the output types are self-explanatory by name. By specifying the time of the sequence T , the given values to be v_1, v_2, v_3 , and the time of the output $seqt$, the output functions of *sequence* f can be given by:

$$\text{Constant : } f = v_1$$

¹This sequence will be ignored.

$$\text{Linear : } f = \frac{v_2 - v_1}{T} \text{seqt} + v_1$$

$$\text{Exp : } f = (v_1 + 1) \exp\left[\frac{\text{seqt}}{T} \log\left(\frac{v_2 + 1}{v_1 + 1}\right)\right] - 1$$

$$\text{Sin : } f = v_1 * \sin(2\pi * v_2 * \text{seqt}) + v_3$$

$$\text{Pulse : } \text{if } \text{rem}\left(\frac{\text{seqt}}{v_2}\right) \leq v_3 \text{ then } f = v_1 \text{ else } f = 0$$

$$\text{SRamp : } f = \frac{v_1(1 + k_1) - v_2(1 + k_2)}{k_1 - k_2} + \frac{\frac{v_1(1+k_1)-v_2(k_1^2+k_1)}{1-k_1^2} - \frac{v_1(1+k_1)-v_2(1+k_2)}{k_1-k_2}}{1 + \exp(-v_3(\text{seqt}/T - 0.5))},$$

where $k_1 = e^{v_3/2}$ and $k_2 = e^{-v_3/2}$

Stand : Stay the same value as before this sequence.

In the digital channel programming, each *sequence* is fixed to 3 input numbers, which are the time of the sequence T , period v_1 and on-off-ratio v_2 (similar to analog pulse function, without the amplitude). If the period is set to zero $v_1 = 0$, then the sequence will give an on/off output based on the value of v_2 (on for $v_2 > 0$, off for $v_2 \leq 0$).

All values can be replaced by *variable* type instead of giving a number, such that we can easily scan and manipulate the output of a sequence.

Variable

The data type '*variable*' allows saving and calculating values for the cycle. In the cycle editor, when inserting a variable is required, the available variables will be given in manual form by right-clicking on the input box. There are four types of variables available:

- **Fix:** Save a number. Usually used to record constant.
- **Scan:** Number that changes value based on scanning operation. When scanning, the value will move from 'Start' to 'End' in step of 'Step'. The value 'Prior' determines the level of scan, where a multi-dimension scan is possible (up to 10) and higher priority variables are scanned first. When 'Prior' is zero, the scan function is disabled for this variable and the value is set to 'Start'.
- **Calculate:** Calculate the value based on a formula. The formula follows conventional syntax with a set of commonly used functions. Furthermore, any user-defined variable could be used as a value in the formula by inserting the name into square brackets "[name]".
- **File:** The variable will load a text file, and depending on the value of '*Fitting*'

gives a different response. If the value is '0' (linear) or '1' (spline), the variable will load the first two columns of the file as numbers (x and y), and connect them to be a function. If the value is '2' (script), the file will be treated as a JavaScript function and be loaded into the script engine. In both cases, these variable are accessible in 'Calculate' with syntax "[name]()"

Internal value: π (π), E (Euler constant).

Internal function: $random^1$, $abs()$, $sin()$, $cos()$, $tan()$, $asin()$, $acos()$, $atan()$, $ln()$, $pow()$, $log()$, $floor()$, $ceil()$.

All variables will be loaded into the script engine for calculation. The program has included an interface to the script engine directly, and the user could check the value or format of the variable, which could serve as a debugger.

Section

Every section is given a number or *variable*. The section is activated when the given number is larger than zero, and switch off if it is smaller or equal to zero. In the editor, the state of sections are indicated by the green (on) or red (off).

Channel Calibration

All ADwin signals are given in voltage. However, for an experiment, parameters are preferred to be set with better physical meaning. For example, when setting magnetic field strength, we would like to give the number in the unit of Gauss, while the power supply receives the control in voltage.

The program provides the function of calibrating a channel with a pre-defined variable. Take the example of the magnetic field again, we measure the relation of "Field \leftarrow Current \leftarrow Control Voltage", and calculate the formula of "Control = f (Field)" and save it into a calculated variable (input is given by x). Then by assigning this variable to the power supply control channel, all output given in this channel will be calibrated with this formula.

Advance Function and Application

To generate a more complex waveform other than the pre-defined function, there are internal time variables that could be called. They are "*segt/sect/cyct*", namely the

¹Generate a random number in [0,1]

time elapsed from the beginning of this '*sequence/section/cycle*'. Combined with the '*File*' variable, we can generate an arbitrary waveform with a given list.

External Add-ons

The program includes a set of internal APIs such that other codes could be combined and synchronized with the experiment, which in our case are the control of cameras and waveform/function generators. It is based on Signal-Slot construction of Qt APIs, which have a similar function as the Callback.

By connecting the signal to a slot function, an external function could be triggered based on the progress of the running cycle. Most commonly, at the beginning of each cycle, a signal '*void new_cycle(QString msg)*' is emitted, such that all cameras and signal/waveform generators would be initialized.

Communication

In the case where external communication is required, the control program has also a built-in protocol where users could send and receive commands.

The output protocol is included in the 'File Transfer' add-on. This allows self-format messages to be transferred via TCP/UDP protocol or saved into a file. Pulling numbers from variables is still possible with '[name]' syntax. This action is triggered at every cycle start, so synchronization between computers and programs could be made possible without coding. For example, our frequency generator for the RF system is connected through an Ethernet cable. At the beginning of each cycle, the control program will send the required output frequency to the IP address of the generator, and the number for frequency is read from variable '[RF_Frequency]'.

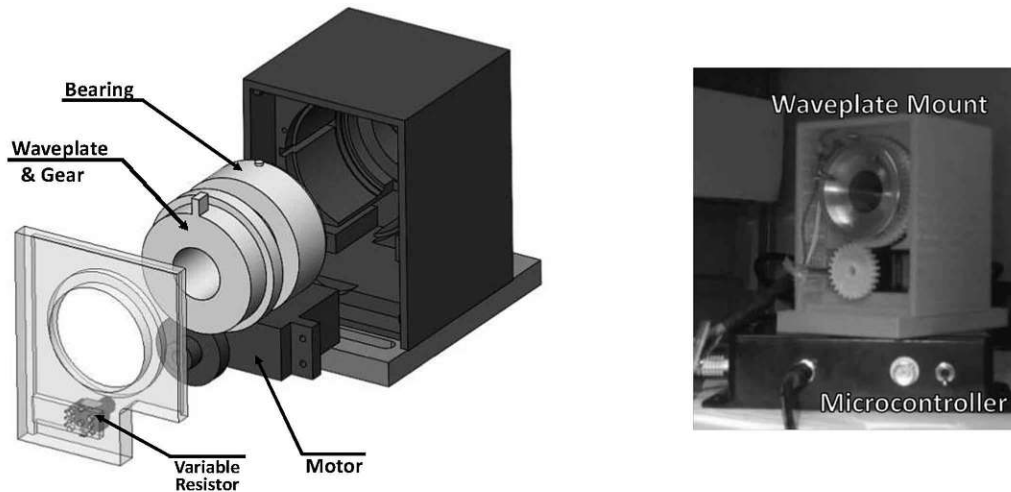
The input protocol is integrated into the program, where the user can define a port for the program to listen via TCP/IP protocol. The commands are pre-defined as 'STOP'/'START_WITHOUT_RELOAD'/'START_WITH_RELOAD' such that the program can be started/stopped remotely by other computer or software, which is useful in the case of feedback like optimal control.

C. Rotational Waveplate Mount

Sec 3.3.1 mentioned a device that rotates a $\lambda/2$ -waveplate during each experiment cycle. The laser light could thus be switched between the trapping and transport path, such that high power laser would not go through the tunable focus lens. So we required a waveplate rotation state that could stably rotate back and forth with an analog control or digital trigger, and the rotation time is better to be around half a second so that it is slow enough for adiabatic transfer.

To our surprise, we were not able to find a suitable commercial product. The closest product we found is the M102 Rotation Stage from LK-Instruments. However, it is built with a high torque stepper motor that generates a strong mechanical vibration during rotation, and we are not able to damp it. This causes a long-term drift of the experiment. So in the end we choose to build the rotational stage ourselves.

We used a scheme of servo motor (DS3218MG) controlled with a microcontroller Arduino Due, with all the mechanical elements fixed inside a 3D printed box. We machine a mounting structure for the waveplate with a gear mounted on the outside. Then the structure is inserted into a bearing for smooth rotation. The motor is mounted beside the bearing, connected to the waveplate mount with a gear ratio of 1:4. Additionally, a variable resistor is connected to the motor, such that the position of the motor could be independently feedback to the microcontroller, correcting for long-term drift.



Choosing and using the servo motor is actually trickier than we think. DS3218MG is a cheap model developed mostly for toy model cars. So the electronics inside are not

designed for long-time continuous operation, especially stall operation. Two motors were broken each after being used for ~ 30000 rounds, as the circuit was being fired. We have tried to upgrade to a higher quality and durable model, however, the higher specification surprisingly causes extra problems, like overturn, vibration, etc. In the end, we still use the cheap model but with small modifications. While connecting the motor to power, we added additional resistors in series, such that the maximum current allowed is reduced. The motor will operate slower (rotation time $300\text{ ms} \rightarrow 700\text{ ms}$, we don't care about torque) but can run reliably.

Controller Scheme and Program

We use an Arduino Due to serve the function as microcontroller, the control program can be found on GitHub (https://github.com/liangqibox/Lithium6_ATI). The Arduino uses pinout as follows:

- *Motor*: Pin 2. This pin generates the frequency signal to control the rotation of the servo motor.
- *Polar*: Pin 6. This pin connects to 3.3V or GND through a toggle switch. At start-up, the status of this pin decides the boot mode (Analog or Digital) of the system. If the system boot into Digital mode, this pin will decide the polarity of the control, which direction the motor rotates on high signal. During calibration or alignment, the toggle switch can also be used as a manual switch to change position (in Digital mode).
- *Digi*: Pin 7. External TTL control input.
- *Analog*: Pin A1. External analog control input.
- *FeedBack*: Pin A0. Determines the position of the motor by reading the voltage from the variable resistor.
- *Setting L/R*: Pin A2/A3. These two pins read the voltage given by two trimmer resistors on board. By adjusting the trimmers, we could change the target position of the rotation in Digital Mode.

The controller can be started into two different control modes: Analog and Digital. It is decided by the status of *Polar* when booting the controller.

- *Analog Mode*: If Switch reads high at startup, the program enters analog control mode. The Switch in this mode is disabled after startup, and the controller will drive the motor to a specific angular position according to the voltage reading from *Analog*.

- Digital Mode: If Switch reads low at startup, the program enters digital control mode. In this case, the controller checks the TTL level of *Polar* and *Digi*. When a change is detected, the controller will drive the motor to the opposite position given by *Setting* with maximum speed.

In our experiment, the waveplate is operated with Digital Mode. A TTL signal is given from the ADwin system each time before the transport stage and returns to the trapping position at the end of the cycle.

List of Figures

2.1.	The energy level of ${}^6\text{Li}$ atom plot with magnetic field.	4
2.2.	Optical dipole transitions of ${}^6\text{Li}$ atom.	4
2.3.	The wavelength-dependent polarizability of the $2s \leftrightarrow 2p_{3/2}$ states (Left) and $2s \leftrightarrow 3p_{3/2}$ states (right). Figure adapted from Ref.[10]	5
2.4.	Feshbach resonances between the lowest three energy states of ${}^6\text{Li}$ [21].	7
2.5.	Illustration of a three-body recombination process.	9
2.6.	Experimental measurement plot with Thomas-Fermi radius calculation.	12
3.1.	3D model of the vacuum chamber.	13
3.2.	(left)A front window heavily coated by Lithium. The coating takes the shape of the Zeeman slower beam. (right)Front window protection setup with both UV lamp and heating.	17
3.3.	(left) Photo of a MOT coil. (right) Magnetic field measurement in axial and radial direction with 10 A of current.	18
3.4.	Snubber circuit of MOT coils. Elements used: IGBT, SKM800GA176D; FRD, STTH60L06W; Shottky diode, MBR40040CT; Power supply, Keysight N8754A. Capacitor C1 should be built from polypropylene film capacitors. Capacitor C2 needs to be large in capacitance, so aluminium capacitors are preferred. IGBT driver built with chip MC33153PG. We measure the turn off time to be $\sim 150\mu\text{s}$	19
3.5.	Schematic (left) and photos (right) of the Bitter type Feshbach coils	20
3.6.	The schematic and 3D model of the coil sets at Sci-Chamber. The coil sets are referred to as Gradient (green), Stern-Gerlach (blue) and Feshbach (yellow) in this thesis.	21
3.7.	The circuit diagram and 3D model of the fast switching circuit. The whole setup is mounted on a copper board that contains cooling water channels. All connections on the board are made with copper blocks to reduce inductance.	22
3.8.	Magnetic field quench by generating a fix field from the primary coils and quenching the quench coils. Magnetic field measured with Gaussmeter.	22
3.9.	Schematic of 671 nm laser system.	24

3.10. Schematic setup of saturation spectroscopy, with the measured spectrum and error signal.	25
3.11. Schematic of offset frequency lock.	26
3.12. Schematic of the UV generation setup. There are three major parts of the system: Sum frequency generation (SFG), Second harmonic generation (SHG) and Iodine spectroscopy locking.	27
3.13. Iodine spectroscopy. Arrow marks the lock position.	28
3.14. Stability measurement by holding the atomic cloud in dipole trap, measured with 2W power. Each measurement circle is 15 s. A clear drift over time can be seen when forming the dipole trap with the tunable lens. Furthermore, the lens starts to show instability after 1 hour of long exposure operation.	30
3.15. (left) Schematic of moving focus setup. (right) Working principle of the tunable lens (Adapted from the manual provided by Optotune).	31
3.16. Schematic of a voltage-controlled current source built base on a power operational amplifier (OPA547). This circuit is capable of stability up to 0.01mA, where the constraint comes from the stability of the resistance (50Ω). We chose a power resistor and connect it to a heat sink.	31
3.17. 1064 nm is split with a non-polarized beam splitter, and focused with a 250 nm cylindrical lens. We use an AR-coated glass plate (WG11010-C from Thorlab) to reflect a small portion of light for power monitoring.	33
3.18. Lattice stability test. (left) Camera imaging and fitting result. (right) Continuous measurement of long-term phase drift.	34
3.19. Schematic of the speckle beam setup. The iris can be used to change the effective NA of the speckle potential, and thus the speckle grain size.	35
3.20. A typical measurement for speckle characterization. Figure adapt from Ref.[49]. (left) Speckle pattern on camera. (middle) Autocorrelation function fitted to Gaussian. (right) Intensity histogram of speckle pattern.	36
3.21. Top (left) and section (right) view of the imaging setup. The two fluoresce imaging beams are sent in at Brewster angle to reduce reflection.	41
3.22. Radio power reflection measured with a spectrum analyzer. Two sets of capacitor are tuned to match the $ 1\rangle \leftrightarrow 2\rangle$ and $ 2\rangle \leftrightarrow 3\rangle$ transition.	43
3.23. Rabi oscillation measurement of $ 1\rangle \leftrightarrow 2\rangle$ started with only $ 1\rangle$ population.	44
3.24. Landau-Zener sweep of $ 2\rangle \rightarrow 3\rangle$ started with $ 1\rangle$ removed.	44
3.25. RF spectroscopy of evaporative cooled state $ 1\rangle 2\rangle$ mixture, using the $ 2\rangle \rightarrow 3\rangle$ transition.	45
3.26. (left) Microwave transition ($ 3\rangle \rightarrow 4\rangle$) frequency measurement for different magnetic fields. 630 G has a low signal for unclear reasons. (right) Resonance frequencies with linear fitting. Theory predicts a slope of 2.8 MHz/G.	46

3.27. The transverse size of the atom cloud after microwave pulse under different magnetic fields. The difference in initial size is caused by the different repulsive interactions. When no pulse is given, the cloud size would reduce because of focusing (Sec. 3.4.1)	47
3.28. $ 3\rangle$ number measure of $ 2\rangle \rightarrow 3\rangle$ Landau-Zener sweep perform at 620G.	50
3.29. Evaporative cooling performed on the bosonic and fermionic sides of the Feshbach resonance.	51
4.1. Schematic of the experimental setup with images taken in situ and after focusing.	53
4.2. Time carpet of momentum evolution of Kapitza-Dirac scattering measured at different scattering lengths.	54
4.3. The TOF images (up) with the integrated momentum distribution (down). We fit the lower plots to a two-part function, where the red and yellow represent the condensate peaks and incoherent background respectively.	55
4.4. (up) Momentum evolution of different interactions after background removal. (Down) Populations of the lowest three momentum modes plotted with Bessel function prediction.	55
4.5. (left) Time carpets measured with $U_0 = 50E_r$ for different interaction strengths. (middle) The momentum modes with background removed and normalized to the total condensate number at each time. The vertical dash lines mark the zoom-in range. (right) The zoom-in view of the recurrence point. The vertical dash lines mark the recurrence.	57
4.6. The experimental measurement (red circle) plot with 1D GPE simulation (blue line) with correction factor $\eta = 4.2$ (Sec 4.1.3). All experimental data have been post-processed with background-removing algorithm.	58
4.7. The formation of density grating in the condensate wavefunction during the lattice pulse, calculated from GPE.	58
4.8. The simulated population evolution of $0\hbar k$ momentum modes with quenching interaction and $U_0 = 500E_r$. Solid lines show the simulation results and dots plot the Bessel function prediction. The two vertical dashed line marks the time of lattice switch-off and interaction switch-on, (left) $t = 3\mu s$ and $t = 5\mu s$, (right) $t = 8\mu s$ and $t = 10\mu s$ respectively.	59
4.9. 1D GPE calculation of the zeroth order diffraction peak with different interaction strength. The curves can be aligned by re-scaling in time to match the first condensate recurrence points to the zero interaction case by $t \rightarrow t/(1+r)$	60

4.10. The delay parameter r inferred from experimental measurements versus the scattering length a_{dd} . Error bars are generated with 10 repeated measurements. The solid line and dash line are produced by GPE simulation with $U_0 = 50E_r$ for $\eta = 4.2$ and $\eta = 1$	61
4.11. Schematic of the pulse sequence and the corresponding absorption images at different interactions with lattice depth $U_0 = 50E_r$	62
4.12. Calculated loss plot against scattering length at different stages. The error level is calculated from the BEC images. The difference between the yellow line and the error level is the loss during the lattice pulse. The difference between the green and yellow lines is the collision loss during TOF.	63
4.13. The population evolution at different interaction strengths (red circle) with collision simulation results (blue solid line) for $U_0 = 50E_r$. The initial condition of the simulation is a product of the GPE calculation multiplied by the loss factor.	64
4.14. The condensate fraction at different interaction strengths (open symbols) with collision simulation results (solid line) for $U_0 = 50E_r$. The increasing discrepancies between calculated results and experimental data indicate the continuing in-trap loss over time.	65
4.15. Interference measured at $a = 487a_0$. (left) The signals from the interferometer are shown in a carpet of differential phase and the population ratio of 0^{th} momentum mode. The red solid line plotted the calculated interference with scaled amplitude and corrected the initial phase. (right) The difference of phase between the experimental measurement and calculation.	67
4.16. Interference measured at $B = 675$ G, $a = 693a_0$ and $B = 700$ G, $a = 982a_0$. It can be seen that the contrast of the oscillation is already very low.	68
4.17. Coherent oscillations at varying interactions. The total particle numbers N and the weighted-average particle number per lattice site \bar{N} are indicated for each dataset. The fitting results are plotted in a red solid line, and the blue dash line indicates the monotonic decreasing offset.	70
4.18. Interaction effects in the Ramsey interferometer. Plots of oscillation frequency (ω), diffraction phase shift (ϕ), maximal contrast (A), and contrast decay rate (λ_c) as functions of calculated differential interaction energy shift between the two states ($\Delta\bar{E}^{int}$). The oscillation frequency (energy gap) is plotted with calculated result following different approximation.	72

5.1.	Two-way transport of energy and particles close to a non-thermal fixed point, resulting in self-similar scaling behavior in both inferred and ultraviolet regimes of the distribution. The grey dash line indicates the non-equilibrium initial state of the system.	74
5.2.	1D Bose Gas [97]. 1D Spinor Bose Gas [96]. 3D Bose Gas [98].	75
5.3.	Schematic setup of scaling experiment.	76
5.4.	(left) Breathing oscillation induced by the squeeze quench. (right) Momentum evolution after pulsing speckles at different times. It could be observed that the breathing mode basically vanishes when pulsing at maximum size.	77
5.5.	(a) In situ longitudinal size measurements of a direction speckle pulse and the squeeze-pulse process. Size obtained from the Gaussian fit of density profile, which can not fully describe the evolution, thus the fluctuation. (b) Width of the simulated density profiles of squeeze-pulse processes for different times of pulsing. (c) The fitted decay rate of the oscillation is plotted with the time for pulsing. A clear maximum can be observed, with pulse time pointing towards the maximum size of the squeezed oscillation.	78
5.6.	(left) Schematic diagram of the vertical speckle setup. (right) Momentum evolution follows the speckle pulse in all directions. The momentum " k_z " is obtained from the measurement of transverse momentum in the vertical speckle setup.	79
5.7.	(left) The likelihood table $L(\beta, \Delta)$. (right) Integration and Gaussian fit of the distribution. In this analysis, the likelihood function is scanned with β and $\Delta = \alpha - \beta$	81
5.8.	The χ^2 calculation for particle number ~ 10000 and scattering length $740a_0$ ($B=620$ G). The lower graph marks the two scaling windows found with this method.	81
5.9.	(Carpet) Longitudinal momentum evolution measured with $B=620$ G, $a=740a_0$. The raw (left) and scaled (middle) momentum profiles within the "1D"(down) and "crossover"(up) scaling windows. (right) The mean ratio of raw and scaled profiles is divided by the reference profile. The scaling cutoff is marked by vertical dash lines.	82
5.10.	Scaling behavior measured with scattering length $622.5a_0$ and particle number $N=4000$. The scaling window is identified to be 16 ± 1 ms. . . .	82

5.11. Scaling exponents and the ratio of "1D" and "crossover" windows versus the chemical potential of the condensate component of the final state. As the "1D" window decreases with increasing interaction, scaling exponents can no longer be determined for $\mu_{fin} > 350Hz$ due to limited statistics, which could also be seen from the increase of the error bar. On the other hand, since $\mu_{fin} < 200Hz$ could only be achieved by reducing particle number in our system, the "crossover" window could not be well identified due to the limited signal-to-noise ratio.	83
5.12. Re-scaled momentum profiles (dots) and the fitted universal function (solid line) for all distributions in both scaling windows. The vertical dash lines mark the scaling cutoff. The inserts plotted the initial profiles of each window for all interactions.	84
5.13. (a) Value of the exponent ζ (solid line) by fitting to the theoretical distribution $[1 + (\frac{k_{gs}}{k_{ns}})^2(\frac{k}{k_{gs}})^2]^{-1}$ (Sec 5.4.1), and comparison to the fitting value of the experimental data (red area). (b) The ratio of the total momentum $\int k n(k)dk$ between the theory model and measured distribution.	85
5.14. The 1D scaling time window versus the interaction strength of the system. To compare with the previous experiment, the x -axis is plotted with chemical potential μ_{fin} calculated from the condensate portion of the final state, divided by radial trap frequency. Horizontal error calculated from the variation of particle number. Purple circles are measurements from ^{87}Rb experiments [105].	86
5.15. Starting time and duration of "crossover" scaling window plot versus the inverse trap frequency.	86
5.16. (a) Longitudinal momentum evolution measured with $B=625\text{ G}$, $a=875.5a_0$ using the "double-pulse" scheme. The raw (b) and scaled (c) momentum profiles. (d) The mean ratio of raw and scaled profiles is divided by the reference profile. The scaling cutoff is marked by vertical dashed lines. The lower part shows the likelihood calculation and scaling check. . . .	87
5.17. Momentum profile of initial state ($t=0$) prepared with different cooling schemes. We plot both distributions with the fitting result to $\sim \exp(-ak^\gamma)$, where $\gamma = 1.057$ for the "squeeze-pulse" sequence and $\gamma = 1.397$ for "double-pulse" sequence.	88
5.18. Robustness checking calculation for (left)"1D" and (right)"Crossover" window in Fig 5.9. The solid areas indicate the error range of exponents calculated from scaling analysis. Each point represents the result of choosing the corresponding time.	89

5.19. Global variable calculation for data sets measured with 7000~10000 particle number. The values of \bar{N} and \bar{M} are rescaled by the respective exponential function, such that the value should be 1 in the scaling regime, marked by the red horizontal line. The gray area indicates the scaling windows.	90
5.20. An illustration of 3D soliton.	91
5.21. Momentum distributions of solitonic state plotted in double Logarithm scales with different combinations of soliton width and density. An power-law relation of $\sim k^{-2}$ can be observed in the region between k_{n_s} and k_{ξ_s}	92
5.22. (a) Thomas-Fermi fit of the in-situ density. (b) The full convoluted distribution n_{con} is plotted with the homogeneous background distribution n_{sol}	94
5.23. Soliton distribution fit for $a = 740a_0$, $N \sim 7500$ at $t = 0, 10\text{ms}$. The insert shows the soliton density during evolution.	95
5.24. Dimensionless scaling time ($\log_{10}(\Delta t\omega_s)$) plot via (a) the reduced size of soliton (ξ_s/ξ_h) and (b) the "1D-ness" ($\mu_{int}/(\hbar\omega_{\perp})$) of the system for both ^6Li and ^{87}Rb experiments in logarithm scale. Doted line indicate the power law fitting result of ^6Li measurements and dash line indicate the fitting result that include both experiment. (c) The 3D diagram that combines the two plots. The three red blocks represent the data sets in ^6Li experiment that do not observe "1D" scaling behavior.	97
6.1. (a) In-situ image of BEC loaded into lattice with spacing $\sim 15\mu\text{m}$. (b) Momentum evolution of BEC diffracted from the lattice potential with scattering length $520a_0$. (c) Delay factor calculation plot with GPE simulation. The delay effect can no longer be compensated by a single correction factor, suggesting a nonlinear discrepancy of GPE at high interaction.	100

List of Tables

2.1. Major optical transitions of ${}^6\text{Li}$ [8].	5
2.2. Feshbach resonances between the lowest 3 energy states of ${}^6\text{Li}$	7
4.1. Relevant quantities to the interferometers	71
5.1. Lithium data (${}^6\text{Li}_2$), $(\nu_I, \nu_L) = (16, 100)$ Hz	93

References

- [1] J. Berges, Sz. Borsányi, and C. Wetterich. “Prethermalization”. In: *Phys. Rev. Lett.* 93 (14 Sept. 2004), p. 142002. DOI: 10.1103/PhysRevLett.93.142002.
- [2] Michael E Gehm. “Properties of 6Li ”. In: *Jetlab*, (2003).
- [3] David R Lide. *CRC handbook of chemistry and physics*. Vol. 85. CRC press, 2004.
- [4] Ennio Arimondo, M Inguscio, and P Violino. “Experimental determinations of the hyperfine structure in the alkali atoms”. In: *Reviews of Modern Physics* 49.1 (1977), p. 31.
- [5] Andrew T. Grier, Igor Ferrier-Barbut, Benno S. Rem, et al. “ Λ -enhanced sub-Doppler cooling of lithium atoms in D_1 gray molasses”. In: *Phys. Rev. A* 87 (6 June 2013), p. 063411. DOI: 10.1103/PhysRevA.87.063411.
- [6] Gregory Breit and II Rabi. “Measurement of nuclear spin”. In: *Physical Review* 38.11 (1931), p. 2082.
- [7] P. M. Duarte, R. A. Hart, J. M. Hitchcock, et al. “All-optical production of a lithium quantum gas using narrow-line laser cooling”. In: *Phys. Rev. A* 84 (6 Dec. 2011), p. 061406. DOI: 10.1103/PhysRevA.84.061406.
- [8] Werner Scherf, Oleg Khait, Helmut Jäger, and Laurentius Windholz. “Re-measurement of the transition frequencies, fine structure splitting and isotope shift of the resonance lines of lithium, sodium and potassium”. In: *Zeitschrift für Physik D Atoms, Molecules and Clusters* 36 (1996), pp. 31–33.
- [9] Nikolai Borisovich Delone and Vladimir P Krainov. “AC Stark shift of atomic energy levels”. In: *Physics-Uspekhi* 42.7 (1999), p. 669.
- [10] M. S. Safronova, U. I. Safronova, and Charles W. Clark. “Magic wavelengths for optical cooling and trapping of lithium”. In: *Phys. Rev. A* 86 (4 Oct. 2012), p. 042505. DOI: 10.1103/PhysRevA.86.042505.
- [11] Herman Feshbach. “Unified theory of nuclear reactions”. In: *Annals of Physics* 5.4 (1958), pp. 357–390. DOI: [https://doi.org/10.1016/0003-4916\(58\)90007-1](https://doi.org/10.1016/0003-4916(58)90007-1).
- [12] Herman Feshbach. “A unified theory of nuclear reactions. II”. In: *Annals of Physics* 19.2 (1962), pp. 287–313. DOI: [https://doi.org/10.1016/0003-4916\(62\)90221-X](https://doi.org/10.1016/0003-4916(62)90221-X).
- [13] U. Fano. “Effects of Configuration Interaction on Intensities and Phase Shifts”. In: *Phys. Rev.* 124 (6 Dec. 1961), pp. 1866–1878. DOI: 10.1103/PhysRev.124.1866.
- [14] H. C. Bryant, B. D. Dieterle, J. Donahue, et al. “Observation of Resonances near 11 eV in the Photodetachment Cross Section of the H^- Ion”. In: *Phys. Rev. Lett.* 38 (5 Jan. 1977), pp. 228–230. DOI: 10.1103/PhysRevLett.38.228.

- [15] S Inouye, MR Andrews, J Stenger, et al. “Observation of Feshbach resonances in a Bose–Einstein condensate”. In: *Nature* 392.6672 (1998), pp. 151–154.
- [16] Ph. Courteille, R. S. Freeland, D. J. Heinzen, F. A. van Abeelen, and B. J. Verhaar. “Observation of a Feshbach Resonance in Cold Atom Scattering”. In: *Phys. Rev. Lett.* 81 (1 July 1998), pp. 69–72. DOI: 10.1103/PhysRevLett.81.69.
- [17] Cheng Chin, Rudolf Grimm, Paul Julienne, and Eite Tiesinga. “Feshbach resonances in ultracold gases”. In: *Rev. Mod. Phys.* 82 (2 Apr. 2010), pp. 1225–1286. DOI: 10.1103/RevModPhys.82.1225.
- [18] M. Theis, G. Thalhammer, K. Winkler, et al. “Tuning the Scattering Length with an Optically Induced Feshbach Resonance”. In: *Phys. Rev. Lett.* 93 (12 Sept. 2004), p. 123001. DOI: 10.1103/PhysRevLett.93.123001.
- [19] M. Bartenstein, A. Altmeyer, S. Riedl, et al. “Precise Determination of ^6Li Cold Collision Parameters by Radio-Frequency Spectroscopy on Weakly Bound Molecules”. In: *Phys. Rev. Lett.* 94 (10 Mar. 2005), p. 103201. DOI: 10.1103/PhysRevLett.94.103201.
- [20] Kevin E. Strecker, Guthrie B. Partridge, and Randall G. Hulet. “Conversion of an Atomic Fermi Gas to a Long-Lived Molecular Bose Gas”. In: *Phys. Rev. Lett.* 91 (8 Aug. 2003), p. 080406. DOI: 10.1103/PhysRevLett.91.080406.
- [21] G. Zürn, T. Lompe, A. N. Wenz, et al. “Precise Characterization of ^6Li Feshbach Resonances Using Trap-Sideband-Resolved RF Spectroscopy of Weakly Bound Molecules”. In: *Phys. Rev. Lett.* 110 (13 Mar. 2013), p. 135301. DOI: 10.1103/PhysRevLett.110.135301.
- [22] D. S. Petrov, C. Salomon, and G. V. Shlyapnikov. “Weakly Bound Dimers of Fermionic Atoms”. In: *Phys. Rev. Lett.* 93 (9 Aug. 2004), p. 090404. DOI: 10.1103/PhysRevLett.93.090404.
- [23] D. S. Petrov, C. Salomon, and G. V. Shlyapnikov. “Scattering properties of weakly bound dimers of fermionic atoms”. In: *Phys. Rev. A* 71 (1 Jan. 2005), p. 012708. DOI: 10.1103/PhysRevA.71.012708.
- [24] Gerhard Zürn, Thomas Lompe, Andre Niklas Wenz, et al. “Precise characterization of $\text{Li } 6$ Feshbach resonances using trap-sideband-resolved RF spectroscopy of weakly bound molecules”. In: *Physical review letters* 110.13 (2013), p. 135301.
- [25] A. J. Moerdijk, B. J. Verhaar, and A. Axelsson. “Resonances in ultracold collisions of ^6Li , ^7Li , and ^{23}Na ”. In: *Phys. Rev. A* 51 (6 June 1995), pp. 4852–4861. DOI: 10.1103/PhysRevA.51.4852.
- [26] S Jochim, M Bartenstein, A Altmeyer, et al. “Pure gas of optically trapped molecules created from fermionic atoms”. In: *Physical review letters* 91.24 (2003), p. 240402.
- [27] Eugene P Gross. “Structure of a quantized vortex in boson systems”. In: *Il Nuovo Cimento (1955-1965)* 20.3 (1961), pp. 454–477.
- [28] Lev P Pitaevskii. “Vortex lines in an imperfect Bose gas”. In: *Sov. Phys. JETP* 13.2 (1961), pp. 451–454.

- [29] D. Amit and E. P. Gross. “Vortex Rings in a Bose Fluid”. In: *Phys. Rev.* 145 (1 May 1966), pp. 130–136. DOI: 10.1103/PhysRev.145.130.
- [30] L Khaykovich, F Schreck, G Ferrari, et al. “Formation of a matter-wave bright soliton”. In: *Science* 296.5571 (2002), pp. 1290–1293.
- [31] Kevin E Strecker, Guthrie B Partridge, Andrew G Truscott, and Randall G Hulet. “Formation and propagation of matter-wave soliton trains”. In: *Nature* 417.6885 (2002), pp. 150–153.
- [32] L. Salasnich, A. Parola, and L. Reatto. “Effective wave equations for the dynamics of cigar-shaped and disk-shaped Bose condensates”. In: *Phys. Rev. A* 65 (4 Apr. 2002), p. 043614. DOI: 10.1103/PhysRevA.65.043614.
- [33] Lev Pitaevskii and Sandro Stringari. *Bose-Einstein condensation and superfluidity*. Vol. 164. Oxford University Press, 2016.
- [34] W. Ketterle, D. S. Durfee, and D. M. Stamper-Kurn. *Making, probing and understanding Bose-Einstein condensates*. 1999.
- [35] In: *La Rivista del Nuovo Cimento* 31.506 (July 2008), pp. 247–422. DOI: 10.1393/ncr/i2008-10033-1.
- [36] I. Abramova, Eugene Aleksandrov Alexandrov, A. Bonch-Bruevich, and V. Khromov. “Photostimulated desorption of metal atoms from surfaces of transparent insulators”. In: *Jetp Letters - JETP LETT-ENGL TR* 39 (Jan. 1984).
- [37] Lukas Heller. “Design and Construction of a Zeeman slower for a ^6Li Atom Experiment”. Technische Universität Wien, 2015.
- [38] Dylan O. Sabulsky, Colin V. Parker, Nathan D. Gemelke, and Cheng Chin. “Efficient continuous-duty Bitter-type electromagnets for cold atom experiments”. In: *Review of Scientific Instruments* 84.10 (Oct. 1, 2013), p. 104706. DOI: 10.1063/1.4826498.
- [39] Sophie Höller. “A Laser Offset Locking Circuit for Imaging under High Magnetic Field”. Technische Universität Wien, 2019.
- [40] A C Wilson, Ospelkaus C, A P VanDevender, et al. “A 750-mW, continuous-wave, solid-state laser source at 313 nm for cooling and manipulating trapped 9Be^+ ions”. In: *Applied Physics B* 105 (4 Dec. 2011), pp. 741–748. DOI: 10.1007/s00340-011-4771-1.
- [41] A Omran. “A microscope for Fermi gases”. PhD thesis. 2016.
- [42] Julian Léonard, Moonjoo Lee, Andrea Morales, et al. “Optical transport and manipulation of an ultracold atomic cloud using focus-tunable lenses”. In: *New Journal of Physics* 16.9 (Sept. 2014), p. 093028. DOI: 10.1088/1367-2630/16/9/093028.
- [43] A. Couvert, T. Kawalec, G. Reinaudi, and D. Guéry-Odelin. “Optimal transport of ultracold atoms in the non-adiabatic regime”. In: *Europhysics Letters* 83.1 (June 2008), p. 13001. DOI: 10.1209/0295-5075/83/13001.

- [44] C. Orzel, A. K. Tuchman, M. L. Fenselau, M. Yasuda, and M. A. Kasevich. “Squeezed States in a Bose-Einstein Condensate”. In: *Science* 291.5512 (2001), pp. 2386–2389.
- [45] Markus Greiner, Olaf Mandel, Tilman Esslinger, Theodor W. Hänsch, and Immanuel Bloch. “Quantum phase transition from a superfluid to a Mott insulator in a gas of ultracold atoms”. In: *Nature* 415.6867 (Jan. 2002), pp. 39–44. DOI: 10.1038/415039a.
- [46] J. E. Lye, L. Fallani, M. Modugno, et al. “Bose-Einstein Condensate in a Random Potential”. In: *Phys. Rev. Lett.* 95 (7 Aug. 2005), p. 070401. DOI: 10.1103/PhysRevLett.95.070401.
- [47] Benjamin Nagler, Sian Barbosa, Jennifer Koch, Giuliano Orso, and Artur Widera. “Observing the loss and revival of long-range phase coherence through disorder quenches”. In: *Proceedings of the National Academy of Sciences* 119.1 (2022), e2111078118. DOI: 10.1073/pnas.2111078118.
- [48] Joseph W Goodman. *Speckle phenomena in optics: theory and applications*. Roberts and Company Publishers, 2007.
- [49] Lorenz Fischer. “Atomic Beam Oven Test and Laser Speckle Analysis for a 6Li Ultracold Atom Experiment”. Technische Universität Wien, 2021.
- [50] C. F. Ockeloen, A. F. Tauschinsky, R. J. C. Spreeuw, and S. Whitlock. “Detection of small atom numbers through image processing”. In: *Phys. Rev. A* 82 (6 Dec. 2010), p. 061606. DOI: 10.1103/PhysRevA.82.061606.
- [51] Linxiao Niu, Xinxin Guo, Yuan Zhan, et al. “Optimized fringe removal algorithm for absorption images”. In: *Applied Physics Letters* 113.14 (Oct. 2018), p. 144103. DOI: 10.1063/1.5040669.
- [52] P. A. Murthy, D. Kedar, T. Lompe, et al. “Matter-wave Fourier optics with a strongly interacting two-dimensional Fermi gas”. In: *Phys. Rev. A* 90 (4 Oct. 2014), p. 043611. DOI: 10.1103/PhysRevA.90.043611.
- [53] Martin Feiler. “Radio frequency setup to address hyperfine state transitions in a cold lithium gas”. Technische Universität Wien, 2019.
- [54] F. Scazza, G. Del Pace, L. Pieri, et al. *An efficient high-current circuit for fast radio-frequency spectroscopy in cold atomic gases*. 2021.
- [55] Bernhard Zeh. “Radio frequency antennas to influence hyperfine state transitions in ultra-cold 6Li atoms”. Technische Universität Wien, 2022.
- [56] M.-O. Mewes, M. R. Andrews, D. M. Kurn, et al. “Output Coupler for Bose-Einstein Condensed Atoms”. In: *Phys. Rev. Lett.* 78 (4 Jan. 1997), pp. 582–585. DOI: 10.1103/PhysRevLett.78.582.
- [57] M. Bartenstein, A. Altmeyer, S. Riedl, et al. “Precise Determination of ^6Li Cold Collision Parameters by Radio-Frequency Spectroscopy on Weakly Bound Molecules”. In: *Phys. Rev. Lett.* 94 (10 Mar. 2005), p. 103201. DOI: 10.1103/PhysRevLett.94.103201.

- [58] P. L. Kapitza and P. A. M. Dirac. “The reflection of electrons from standing light waves”. In: *Mathematical Proceedings of the Cambridge Philosophical Society* 29.2 (1933), pp. 297–300. DOI: 10.1017/S0305004100011105.
- [59] Alexander D. Cronin, Jörg Schmiedmayer, and David E. Pritchard. “Optics and interferometry with atoms and molecules”. In: *Rev. Mod. Phys.* 81 (3 July 2009), pp. 1051–1129. DOI: 10.1103/RevModPhys.81.1051.
- [60] Phillip L. Gould, George A. Ruff, and David E. Pritchard. “Diffraction of atoms by light: The near-resonant Kapitza-Dirac effect”. In: *Phys. Rev. Lett.* 56 (8 Feb. 1986), pp. 827–830. DOI: 10.1103/PhysRevLett.56.827.
- [61] Daniel L. Freimund, Kayvan Aflatoon, and Herman Batelaan. “Observation of the Kapitza-Dirac effect”. In: *Nature* 413.6852 (2001), pp. 142–143. DOI: 10.1038/35093065.
- [62] Daniel L. Freimund and Herman Batelaan. “Bragg Scattering of Free Electrons Using the Kapitza-Dirac Effect”. In: *Phys. Rev. Lett.* 89 (28 Dec. 2002), p. 283602. DOI: 10.1103/PhysRevLett.89.283602.
- [63] M. Kozuma, L. Deng, E. W. Hagley, et al. “Coherent Splitting of Bose-Einstein Condensed Atoms with Optically Induced Bragg Diffraction”. In: *Phys. Rev. Lett.* 82 (5 Feb. 1999), pp. 871–875. DOI: 10.1103/PhysRevLett.82.871.
- [64] S. B. Cahn, A. Kumarakrishnan, U. Shim, et al. “Time-Domain de Broglie Wave Interferometry”. In: *Phys. Rev. Lett.* 79 (5 Aug. 1997), pp. 784–787. DOI: 10.1103/PhysRevLett.79.784.
- [65] Yu. B. Ovchinnikov, J. H. Müller, M. R. Doery, et al. “Diffraction of a Released Bose-Einstein Condensate by a Pulsed Standing Light Wave”. In: *Phys. Rev. Lett.* 83 (2 July 1999), pp. 284–287. DOI: 10.1103/PhysRevLett.83.284.
- [66] R. E. Sapiro, R. Zhang, and G. Raithel. “Atom interferometry using Kapitza-Dirac scattering in a magnetic trap”. In: *Phys. Rev. A* 79 (4 Apr. 2009), p. 043630. DOI: 10.1103/PhysRevA.79.043630.
- [67] Qi Liang, Chen Li, Sebastian Erne, et al. “Diffraction of strongly interacting molecular Bose-Einstein condensate from standing wave light pulses”. In: *SciPost Phys.* 12 (2022), p. 154. DOI: 10.21468/SciPostPhys.12.5.154.
- [68] Julian Grond, Ulrich Hohenester, Igor Mazets, and Jörg Schmiedmayer. “Atom interferometry with trapped Bose-Einstein condensates: impact of atom-atom interactions”. In: *New Journal of Physics* 12.6 (June 2010), p. 065036. DOI: 10.1088/1367-2630/12/6/065036.
- [69] S. Hofferberth, I. Lesanovsky, T. Schumm, et al. “Probing quantum and thermal noise in an interacting many-body system”. In: *Nature Physics* 4.6 (June 2008), pp. 489–495. DOI: 10.1038/nphys941.
- [70] Juha Javanainen and Martin Wilkens. “Phase and Phase Diffusion of a Split Bose-Einstein Condensate”. In: *Phys. Rev. Lett.* 78 (25 June 1997), pp. 4675–4678. DOI: 10.1103/PhysRevLett.78.4675.

- [71] C. V. Raman and N. S. Nagendra Nathe. “The diffraction of light by high frequency sound waves: Part I.” In: *Proceedings of the Indian Academy of Sciences - Section A* 2.4 (1935), pp. 406–412. DOI: 10.1007/BF03035840.
- [72] Bryce Gadway, Daniel Pertot, René Reimann, Martin G. Cohen, and Dominik Schneble. “Analysis of Kapitza-Dirac diffraction patterns beyond the Raman-Nath regime”. In: *Opt. Express* 17.21 (Oct. 2009), pp. 19173–19180. DOI: 10.1364/OE.17.019173.
- [73] Matteo Sbroscia, Konrad Viebahn, Edward Carter, et al. “Observing Localization in a 2D Quasicrystalline Optical Lattice”. In: *Phys. Rev. Lett.* 125 (20 Nov. 2020), p. 200604. DOI: 10.1103/PhysRevLett.125.200604.
- [74] G V Skorniakov and K A Ter-Martirosian. “Three body problem for short range forces. I Scattering of low energy neutrons by deuterons”. In: *Soviet Phys. JETP* 4 (June 1957).
- [75] Chen Li, Tianwei Zhou, Igor Mazets, et al. “Relaxation of bosons in one dimension and the onset of dimensional crossover”. In: *SciPost Physics* 9.4 (Oct. 2020), p. 058. DOI: 10.21468/SciPostPhys.9.4.058.
- [76] DE Miller, JK Chin, CA Stan, et al. “Critical velocity for superfluid flow across the BEC-BCS crossover”. In: *Physical review letters* 99.7 (2007), p. 070402.
- [77] R. Thomas, K. O. Roberts, E. Tiesinga, et al. “Multiple scattering dynamics of fermions at an isolated p-wave resonance”. In: *Nature Communications* (1 2016), p. 12069. DOI: 10.1038/ncomms12069.
- [78] S. Chu A. Peters K. Y. Chung. “Measurement of gravitational acceleration by dropping atoms”. In: *Nature* 400 (1999), pp. 849–852. DOI: 10.1038/23655.
- [79] J. E. Debs, P. A. Altin, T. H. Barter, et al. “Cold-atom gravimetry with a Bose-Einstein condensate”. In: *Phys. Rev. A* 84 (3 Sept. 2011), p. 033610. DOI: 10.1103/PhysRevA.84.033610.
- [80] P A Altin, M T Johnsson, V Negnevitsky, et al. “Precision atomic gravimeter based on Bragg diffraction”. In: *New Journal of Physics* 15.2 (Feb. 2013), p. 023009. DOI: 10.1088/1367-2630/15/2/023009.
- [81] J. B. Fixler, G. T. Foster, J. M. McGuirk, and M. A. Kasevich. “Atom Interferometer Measurement of the Newtonian Constant of Gravity”. In: *Science* 315.5808 (2007), pp. 74–77. DOI: 10.1126/science.1135459.
- [82] G. Rosi, F. Sorrentino, L. Cacciapuoti, M. Prevedelli, and G. M. Tino. “Precision measurement of the Newtonian gravitational constant using cold atoms”. In: *Nature* 510 (2014), pp. 518–521. DOI: 10.1038/nature13433.
- [83] Peter W. Graham, Jason M. Hogan, Mark A. Kasevich, and Surjeet Rajendran. “New Method for Gravitational Wave Detection with Atomic Sensors”. In: *Phys. Rev. Lett.* 110 (17 Apr. 2013), p. 171102. DOI: 10.1103/PhysRevLett.110.171102.
- [84] Jason M. Hogan and Mark A. Kasevich. “Atom-interferometric gravitational-wave detection using heterodyne laser links”. In: *Phys. Rev. A* 94 (3 Sept. 2016), p. 033632. DOI: 10.1103/PhysRevA.94.033632.

- [85] B. P. Abbott, R. Abbott, T. D. Abbott, et al. “GW151226: Observation of Gravitational Waves from a 22-Solar-Mass Binary Black Hole Coalescence”. In: *Phys. Rev. Lett.* 116 (24 June 2016), p. 241103. DOI: 10.1103/PhysRevLett.116.241103.
- [86] Chen Li, Qi Liang, Pradyumna Paranjape, RuGway Wu, and Jörg Schmiedmayer. “Matter-wave interferometers with trapped strongly interacting Feshbach molecules”. In: *Phys. Rev. Res.* 6 (2 May 2024), p. 023217. DOI: 10.1103/PhysRevResearch.6.023217.
- [87] Qi Liang, RuGway Wu, Jörg Schmiedmayer, and Sebastian Erne. “Universal dynamics in strongly interacting Bose gases far from equilibrium”. In preparation.
- [88] P. C. Hohenberg and B. I. Halperin. “Theory of dynamic critical phenomena”. In: *Rev. Mod. Phys.* 49 (3 July 1977), pp. 435–479. DOI: 10.1103/RevModPhys.49.435.
- [89] Nigel Goldenfeld. *Lectures on phase transitions and the renormalization group*. CRC Press, 2018.
- [90] Kenneth G. Wilson. “The renormalization group and critical phenomena”. In: *Rev. Mod. Phys.* 55 (3 July 1983), pp. 583–600. DOI: 10.1103/RevModPhys.55.583.
- [91] Jürgen Berges and Gabriele Hoffmeister. “Nonthermal fixed points and the functional renormalization group”. In: *Nuclear Physics B* 813.3 (2009), pp. 383–407. DOI: <https://doi.org/10.1016/j.nuclphysb.2008.12.017>.
- [92] Thomas Gasenzer and Jan M. Pawłowski. “Towards far-from-equilibrium quantum field dynamics: A functional renormalisation-group approach”. In: *Physics Letters B* 670.2 (2008), pp. 135–140. DOI: <https://doi.org/10.1016/j.physletb.2008.10.049>.
- [93] Jürgen Berges, Alexander Rothkopf, and Jonas Schmidt. “Nonthermal Fixed Points: Effective Weak Coupling for Strongly Correlated Systems Far from Equilibrium”. In: *Phys. Rev. Lett.* 101 (4 July 2008), p. 041603. DOI: 10.1103/PhysRevLett.101.041603.
- [94] Asier Piñeiro Orioli, Kirill Boguslavski, and Jürgen Berges. “Universal self-similar dynamics of relativistic and nonrelativistic field theories near nonthermal fixed points”. In: *Phys. Rev. D* 92 (2 July 2015), p. 025041. DOI: 10.1103/PhysRevD.92.025041.
- [95] J. Berges, K. Boguslavski, S. Schlichting, and R. Venugopalan. “Universality Far from Equilibrium: From Superfluid Bose Gases to Heavy-Ion Collisions”. In: *Phys. Rev. Lett.* 114 (6 Feb. 2015), p. 061601. DOI: 10.1103/PhysRevLett.114.061601.
- [96] Maximilian Prüfer, Philipp Kunkel, Helmut Strobelt, et al. “Observation of universal dynamics in a spinor Bose gas far from equilibrium”. In: *Nature* 563 (7730 2018), pp. 217–220. DOI: 10.1038/s41586-018-0659-0.

- [97] Sebastian Erne, Robert Bückler, Thomas Gasenzer, Jürgen Berges, and Jörg Schmiedmayer. “Universal dynamics in an isolated one-dimensional Bose gas far from equilibrium”. In: *Nature* 563 (7730 2018), pp. 225–229. DOI: 10.1038/s41586-018-0667-0.
- [98] Jake A. P. Glidden, Christoph Eigen, Lena H. Dogra, et al. “Bidirectional dynamic scaling in an isolated Bose gas far from equilibrium”. In: *Nature Phys.* 17 (4 2021), pp. 457–461. DOI: 10.1038/s41567-020-01114-x.
- [99] Maciej Gałka, Panagiotis Christodoulou, Martin Gazo, et al. “Emergence of Isotropy and Dynamic Scaling in 2D Wave Turbulence in a Homogeneous Bose Gas”. In: *Phys. Rev. Lett.* 129 (19 Nov. 2022), p. 190402. DOI: 10.1103/PhysRevLett.129.190402.
- [100] SeungJung Huh, Koushik Mukherjee, Kiryang Kwon, et al. *Classifying the universal coarsening dynamics of a quenched ferromagnetic condensate*. 2023.
- [101] Xiang-Pei Liu, Xing-Can Yao, Youjin Deng, et al. “Dynamic formation of quasicondensate and spontaneous vortices in a strongly interacting Fermi gas”. In: *Phys. Rev. Res.* 3 (4 Nov. 2021), p. 043115. DOI: 10.1103/PhysRevResearch.3.043115.
- [102] Isara Chantesana, Asier Piñeiro Orioli, and Thomas Gasenzer. “Kinetic theory of nonthermal fixed points in a Bose gas”. In: *Phys. Rev. A* 99 (4 Apr. 2019), p. 043620. DOI: 10.1103/PhysRevA.99.043620.
- [103] R. Walz, K. Boguslavski, and J. Berges. “Large- N kinetic theory for highly occupied systems”. In: *Phys. Rev. D* 97 (11 June 2018), p. 116011. DOI: 10.1103/PhysRevD.97.116011.
- [104] Christoph Fritzl. “Suppression of breathing excitations through speckle potentials in the mean-field Gross-Pitaevskii equation”. Technische Universität Wien, 2024.
- [105] Erne Sebastian. “Far-From-Equilibrium Quantum Many-Body Systems From Universal Dynamics to Statistical Mechanics”. PhD thesis. 2018.
- [106] Boris Nowak, Jan Schole, Dénes Sexty, and Thomas Gasenzer. “Nonthermal fixed points, vortex statistics, and superfluid turbulence in an ultracold Bose gas”. In: *Phys. Rev. A* 85 (4 Apr. 2012), p. 043627. DOI: 10.1103/PhysRevA.85.043627.
- [107] Maximilian Schmidt, Sebastian Erne, Boris Nowak, Dénes Sexty, and Thomas Gasenzer. “Non-thermal fixed points and solitons in a one-dimensional Bose gas”. In: *New Journal of Physics* 14.7 (July 2012), p. 075005. DOI: 10.1088/1367-2630/14/7/075005.
- [108] Lasse Gresista, Torsten V Zache, and Jürgen Berges. “Dimensional crossover for universal scaling far from equilibrium”. In: *Physical Review A* 105.1 (2022), p. 013320.
- [109] Peter Fulde and Richard A. Ferrell. “Superconductivity in a Strong Spin-Exchange Field”. In: *Phys. Rev.* 135 (3A Aug. 1964), A550–A563. DOI: 10.1103/PhysRev.135.A550.

References

- [110] A I Larkin and Yu N Ovchinnikov. "NONUNIFORM STATE OF SUPERCONDUCTORS". In: *Zh. Eksperim. i Teor. Fiz.* 47 (Sept. 1964).
- [111] Mason Swanson, Yen Lee Loh, and Nandini Trivedi. "Proposal for interferometric detection of the topological character of modulated superfluidity in ultracold Fermi gases". In: *New Journal of Physics* 14.3 (Mar. 2012), p. 033036. DOI: 10.1088/1367-2630/14/3/033036.